

There is Nothing Anomalous about “Anomalous” Underscreening in Concentrated Electrolytes

Sophie Baker^{†,1}, Gareth R. Elliott^{†,1}, Erica J. Wanless¹, Grant B. Webber², Vincent S. J. Craig³,
Alister J. Page^{*1}

¹*Discipline of Chemistry, The University of Newcastle, Callaghan, New South Wales 2308, Australia*

²*Discipline of Chemical Engineering, The University of Newcastle, Callaghan, New South Wales 2308, Australia*

³*Department of Material Physics, Research School of Physics, Australian National University, Canberra, ACT 0200
Australia*

[†]These authors contributed equally

***Corresponding author.** Email: alister.page@newcastle.edu.au

Abstract

Over the last decade, experimental measurements of electrostatic screening lengths in concentrated electrolytes have exceeded theoretical predictions by orders of magnitude. This disagreement has led to a paradigm in which such screening lengths are referred to as “anomalous underscreening”, while others – predominantly those predicted by theory and molecular simulation – are referred to as “normal underscreening”. Herein we use discrete Fourier analysis of the radial charge density obtained from molecular dynamics simulations to reveal the origin of anomalous underscreening in concentrated electrolytes. Normal underscreening above the Kirkwood point arises from low-frequency decay modes of the electrostatic potential, while anomalous underscreening arises from high-frequency decay modes that are observed only at high concentrations. The screening length associated with a particular decay mode is in turn determined by the degree of short-range interference between ion-ion correlation functions. The long-range decay associated with anomalous underscreening is thus ultimately determined by short range structure in the bulk electrolyte. These results reconcile the disagreement between experimental measurements and theoretical predictions of screening lengths in concentrated electrolytes.

The addition of ions to a liquid causes a remarkable deviation in its behaviour and properties. Arguably the most fundamental of these is an electrolyte's electrostatic screening length – the length scale over which the electrostatic field around individual ions are ‘screened’ by the local electrolyte structure. The decay of the electrostatic potential $\psi(r)$ due to a local charge density $\rho(r)$ at temperature T is predicted via the Poisson-Boltzmann equation,

$$\varepsilon_0 \varepsilon_r \nabla^2 \psi(r) = q n e^{-q\psi(r)/k_B T} \quad (1)$$

where ε_r is the dielectric permittivity of the (continuum) solvent, and $\rho(r)$ arises from an ensemble of n point charges q . By assuming an infinitely dilute, symmetric electrolyte, the seminal Debye-Hückel theory shows that for $r \rightarrow \infty$, $\psi(r)$ exhibits Yukawa decay,

$$\psi(r) \sim C \frac{e^{-\kappa r}}{r} \quad (2)$$

such that $C \rightarrow q/4\pi \varepsilon_0 \varepsilon_r$ and,

$$\kappa = \sqrt{\frac{q^2 \sum_j n_j Z_j^2}{\varepsilon_0 \varepsilon_r k_B T}} \quad (3)$$

where the Debye length, $\lambda_D \equiv \kappa^{-1}$, is the distance r over which $\psi(r)$ decays by $1/e$.¹ Here $\sum_j n_j Z_j^2$ is the ionic strength of the electrolyte comprising n_j ions of type j with formal charge Z_j . The Debye-Hückel assumptions are invalid at concentrations above ~ 0.1 - 0.5 M², as solutions to equation (1) can no longer be linearised. Theoretical treatments of electrostatic potential decay³⁻⁸ in concentrated electrolytes instead have their origins in the statistical mechanical treatments of Kirkwood.⁹⁻¹¹ Kjellander has shown that³,

$$\psi(r) = \frac{q^{\text{eff}}}{4\pi \varepsilon_r^{\text{eff}} \varepsilon_0} \frac{e^{-\kappa r}}{r} + \frac{q'^{\text{eff}}}{4\pi \varepsilon_r'^{\text{eff}} \varepsilon_0} \frac{e^{-\kappa' r}}{r} + \dots \quad (4a)$$

and

$$\rho(r) = \frac{\kappa^2 q^{\text{eff}} \varepsilon_r}{4\pi \varepsilon_r^{\text{eff}}} \frac{e^{-\kappa r}}{r} + \frac{\kappa'^2 q'^{\text{eff}} \varepsilon_r}{4\pi \varepsilon_r'^{\text{eff}}} \frac{e^{-\kappa' r}}{r} + \dots \quad (4b)$$

In effect, the electrostatic decay within the electrolyte is multi-modal and determined by the complex effective charges and permittivity q^{eff} and $\varepsilon_r^{\text{eff}}$. Sufficiently high concentrations also lead to the decay parameters κ and κ' themselves becoming complex conjugates, i.e. $\kappa = \kappa_{\Re} + i\kappa_{\Im}$ and $\kappa' = \kappa^* = \kappa_{\Re} - i\kappa_{\Im}$, and both $\psi(r)$ and $\rho(r)$ becoming oscillatory in nature,

$$\rho(r) = \frac{|\kappa^2||q^{\text{eff}}|\epsilon_r}{2\pi|\epsilon_r^{\text{eff}}|} \frac{e^{-\kappa_{\mathfrak{R}}r}}{r} \cos(\kappa_{\mathfrak{I}}r + \alpha) + \dots \quad (5)$$

The concentration at which the decay of the electrostatic potential transitions from exponential Yukawa decay to complex oscillatory decay is known as the Kirkwood point. At concentrations above this point, the screening length κ^{-1} is predicted to increase, contrary to Debye-Hückel theory.

The typical application of Kirkwood's theoretical treatment for predicting κ assumes *a priori* that $\psi(r)$ and $\rho(r)$ (equation (5)) is dominated by a single oscillatory term.¹²⁻¹⁷ An example that illustrates this typical approach is provided in Figure 1, for a molecular dynamics (MD) simulation of ~ 7 M LiCl_(aq). The form of $\rho(r)$ can be inferred directly from the total charge correlation function¹⁸ obtained from an MD trajectory, $g_{zz}(r)$,

$$\rho(r) \sim g_{zz}(r) = g_{++}(r) + g_{--}(r) - 2g_{+-}(r) \quad (6)$$

where g_{++} , g_{--} and g_{+-} are the cation-cation, anion-anion and cation-anion radial distribution functions respectively (Figure 1a, inset). Equations (6) and (5) are then equated,

$$\ln(|g_{zz}(r)| \cdot r) = -\kappa_{\mathfrak{R}}r + \ln\left(\frac{|\kappa^2||q^{\text{eff}}|\epsilon_r}{2\pi|\epsilon_r^{\text{eff}}|} \cdot |\cos(\kappa_{\mathfrak{I}}r + \alpha)|\right) \quad (7)$$

where $A = \frac{|\kappa^2||q^{\text{eff}}|\epsilon_r}{2\pi|\epsilon_r^{\text{eff}}|}$. The screening length $\lambda_s \equiv \kappa_{\mathfrak{R}}^{-1}$ can then be obtained simply as the inverse slope of the curve in Figure 1a. Screening lengths derived in this manner are compared with experimental values¹⁹⁻²⁵ for aqueous alkali metal chloride electrolytes ($\sim 0.1 - 9$ M) and pure ionic liquid (IL) 1-ethyl-3-methylimidazolium tetrafluoroborate ([C₂C₁im][BF₄]) in Figure 1b. This figure shows the predicted screening lengths are orders of magnitude smaller than those observed experimentally. For instance, λ_s predicted for 7 M LiCl is 3.4 Å, whereas fluorescence measurements of the same system indicate that it is 75.3 Å.²⁴ This disparity between theory and experiment has been noted extensively over the last decade and has led to screening lengths being classed as either 'normal' or 'anomalous'.²⁶

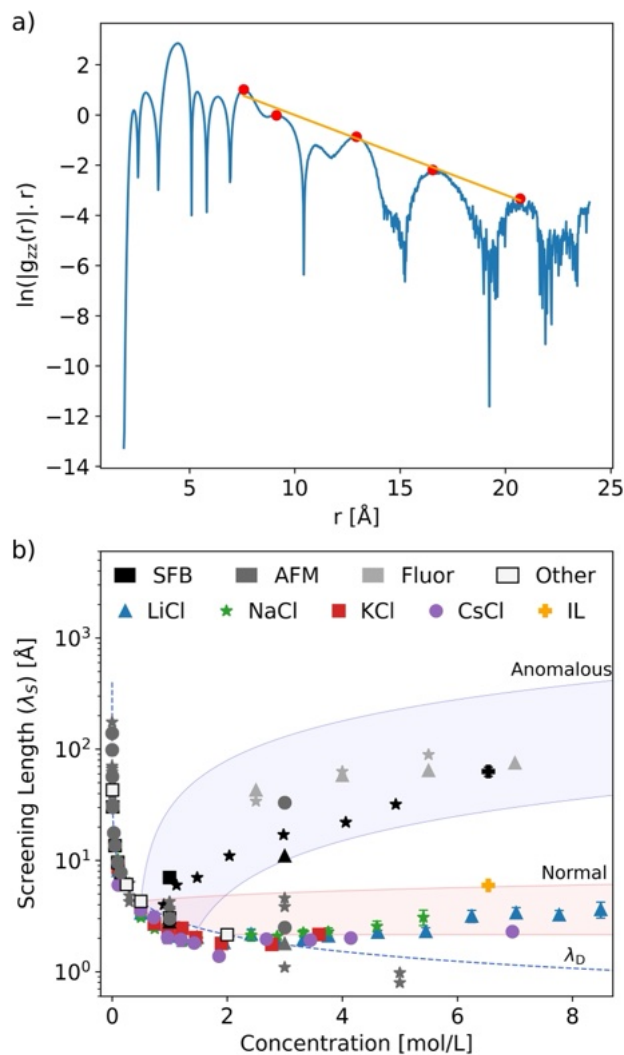


Figure 1. Calculation of λ_s from molecular dynamics (MD) simulations. (a) Conventionally the electrostatic screening length can be obtained from the radial charge density by plotting $\ln(|g_{zz}(r)| \cdot r)$ as a function of radial distance r (illustrated here for 7M $\text{LiCl}_{(\text{aq})}$). The red points and straight line indicate the region used to obtain λ_s via linear regression. (b) Comparison of screening lengths obtained using the method in (a) with experimental values for alkali metal chlorides and the pure IL $[\text{C}_2\text{C}_1\text{im}][\text{BF}_4]$.^{19–25} MD-derived screening lengths fail to reproduce the anomalous values observed experimentally. Full details of all conventionally-derived λ_s values are provided in Supporting Information.

There are notable curiosities regarding experimentally measured anomalous screening lengths. For instance, Figure 1b shows that nearly all experimental evidence for anomalous underscreening comes from surface force balance (SFB) force/distance curves. On the other hand, force/distance

curves measured via atomic force microscopy (AFM) experiments do not detect anomalous underscreening^{19,20}, with one exception at elevated temperatures²⁷. Fluorescence measurements,²⁴ and inferences made from re-entrant colloidal and soft matter behaviour,^{23,26,28–30} however indicate that anomalous underscreening is not simply an artefact of the SFB technique. The effect of surface chemistry and the geometric nature of the confinement on the screening length is still an open area of enquiry²⁶, with recent works suggesting in a salt-in-IL system that the confinement produced polymer-like structures that were the origin of the force (at least in that system)³¹, rather than purely electrostatic.

Similarly, there are curiosities regarding screening lengths derived from theoretical treatments and molecular simulations. Without exception, such approaches fail to reproduce anomalous screening lengths measured experimentally and predict so-called ‘normal’ underscreening. Even the most sophisticated and extensive molecular dynamics (MD) simulations^{12–14} available in the literature were unable to demonstrate the origin of this effect. Some theoretical works have suggested that confinement causes significant increase in the degree of ion pairing^{32,33} in ILs and simple electrolytes, or there is an effect due to particle exchange^{34,35}, or that a cavity is not necessarily needed, attributing it simply to ion pairing^{36,37}, resulting in an effectively dilute electrolyte. Yet MD simulations³⁸ have shown that ion pairing in aqueous electrolytes is transient, and strongly ion specific. Other works have suggested that a plasma-like collective behaviour exists^{39,40}. The electronic effects of the solvent are also important⁴¹, and screening lengths vary with the solvent^{42,43} and also applied electrostatic fields⁴⁴. While Kjellander has shown that many decay modes exist in a concentrated electrolyte,^{45,46} it was suggested recently that the mode responsible for anomalous underscreening has a small amplitude and occurs over a large dynamic range.⁴⁷

However, nearly all simulated and predicted screening lengths have two essential assumptions in common. Firstly, they all are based *a priori* on the assumption that the decay of the oscillatory potential (equation (5b)) at high concentrations is dominated by a single decay mode. Secondly, the application of equation (7) typically employs a range of ~5-20 Å to determine the value of λ_s (approximately the range indicated in Figure 1a). While Zeman et al.^{13,14} used 2 and 3 independent modes to derive λ_s for 1-butyl-3-methylimidazolium hexafluorophosphate ([C₄C₁im][PF₆]) and NaCl solutions, a similar range was still used and anomalous underscreening was not observed.

Here we present an alternative analysis of the radial charge density $\rho(r)$ that reveals the origins of anomalously large screening lengths in concentrated electrolytes. We again take the assumption that $\rho(r) \sim g_{zz}(r)$, consistent with equation (6). Instead of restricting the expansion of $\rho(r)$ in equation (5) to a single mode however, we apply a discrete Fourier transform \mathfrak{F} to the complete expansion across all length scales,

$$\mathfrak{F}[[g_{zz}(r)| \cdot r](k) = \mathfrak{F}[Ae^{-\kappa_{\mathfrak{R}}r} \cos(\kappa_{\mathfrak{S}}r + \alpha)](k) + \mathfrak{F}[A'e^{-\kappa'_{\mathfrak{R}}r} \cos(\kappa'_{\mathfrak{S}}r + \alpha')](k) + \dots \quad (8)$$

As \mathfrak{F} is linear, and as each term in equation (5) is independent, an arbitrary number of screening lengths $1/\kappa_{\mathfrak{R}}$, $1/\kappa'_{\mathfrak{R}}$, $1/\kappa''_{\mathfrak{R}}$, ... can be extracted directly from the discrete Fourier transform of the exponential decay component in each term,

$$\mathfrak{F}[e^{-\kappa_{\mathfrak{R}}r}](k) = \frac{1}{\sqrt{2\pi}} \frac{-\kappa_{\mathfrak{R}}}{k^2 + \kappa_{\mathfrak{R}}^2} \quad (9)$$

Figure 2 illustrates the application of this approach to the same simulation as that presented in Figure 1a. Figure 2a shows the $g_{zz}(r) \cdot r$ function for ~ 7 M LiCl_(aq), and the corresponding Fourier transform is depicted in Figure 2b. In this case, five peaks in the discrete Fourier transform are resolved unambiguously, corresponding to five independent decay modes and their associated screening lengths. We note that the resolution of additional decay modes in Figure 2b is limited only by the sampling density of the radial distribution function employed. Of the decay modes resolved, two exhibit low spatial frequencies ($k < 1 \text{ \AA}^{-1}$), whereas three exhibit high spatial frequencies ($k > 1 \text{ \AA}^{-1}$). These modes manifest, respectively, as long and short oscillations in the total charge distribution function (Figure 2a). The screening lengths associated with the decay of the low spatial frequency modes, 4.15 ± 0.26 and $5.42 \pm 0.31 \text{ \AA}$ respectively, are consistent with ‘normal’ underscreening obtained using the conventional approach (Figure 1). However, the high spatial frequency modes give rise to screening lengths of 141 ± 53 , 167 ± 66 and $229 \pm 74 \text{ \AA}$ respectively. These screening lengths are consistent with the ‘anomalous’ underscreening observed experimentally (see Figure 1b).

The oscillatory length scales in the radial charge density associated with anomalous underscreening (i.e. 0.45 , 0.56 and 0.74 \AA) are shorter than all chemical bonds in this system (and any chemical bond more generally), all intermolecular interaction distances, and the bare/hydrated ion sizes of both Li⁺ and Cl⁻. Anomalous underscreening therefore cannot be due to any individual

chemical moiety present in $\text{LiCl}_{(\text{aq})}$. Figure 2c shows instead that the oscillatory length scale of all decay modes is the result of short-range interference between $g_{++}(\mathbf{r})$, $g_{--}(\mathbf{r})$ and $g_{+-}(\mathbf{r})$ correlation functions; in effect, how similar the ion-ion correlation functions are for ions of like and opposite charge. The high spatial frequency decay modes (i.e. anomalous underscreening modes) arise when these correlations are nearly, but not exactly, commensurate. For instance, the g_{++} and g_{+-} correlation functions in 7M $\text{LiCl}_{(\text{aq})}$ share a peak at $\sim 5 \text{ \AA}$, however there is a difference of precisely 0.41 \AA . This difference is consistent with the oscillatory length scale of the 2.24 \AA^{-1} frequency mode obtained via the discrete Fourier transform of $g_{zz}(r) \cdot r$, 0.45 \AA . The $g_{--}(\mathbf{r})$ function for 7M $\text{LiCl}_{(\text{aq})}$ also exhibits a peak at $\sim 5 \text{ \AA}$ that is precisely 0.58 \AA larger than the length scale of the peak observed in the $g_{+-}(\mathbf{r})$ correlation function. This difference is consistent with the oscillatory length scale associated with the 1.79 \AA^{-1} decay mode, 0.56 \AA . This is true also at longer radial distances; for instance, the $g_{++}(\mathbf{r})$ and $g_{+-}(\mathbf{r})$ both exhibit peaks at $\sim 10 \text{ \AA}$ that differ by precisely 0.74 \AA , in exact agreement with the oscillatory length scale for the 1.35 \AA^{-1} decay mode (see Table S1 in Supporting Information).

Conversely, normal underscreening (i.e. the low spatial frequency decay modes) results when the interference between $g_{++}(\mathbf{r})$, $g_{--}(\mathbf{r})$ and $g_{+-}(\mathbf{r})$ correlation functions occurs at larger distances. The fact that these modes are significantly more prominent in Figure 2b, reflects the fact that there are far more instances at which $g_{++}(\mathbf{r})$, $g_{--}(\mathbf{r})$ and $g_{+-}(\mathbf{r})$ interfere at the corresponding length scales. For instance, there are 13 instances where $g_{++}(\mathbf{r})$, $g_{--}(\mathbf{r})$ and $g_{+-}(\mathbf{r})$ interfere at a length scale of 2.18 \AA , which is consistent with the length scale of the 0.46 \AA^{-1} frequency mode observed in the discrete Fourier transform of $g_{zz}(r) \cdot r$. Similarly, the most prominent peak in Figure 2b, the 0.13 \AA^{-1} frequency decay mode, arises from 15 distinct interferences between $g_{++}(\mathbf{r})$, $g_{--}(\mathbf{r})$ and $g_{+-}(\mathbf{r})$ (see Table S2 in Supporting Information).

Figure 2c demonstrates that both normal and anomalous underscreening in 7 M $\text{LiCl}_{(\text{aq})}$ are the direct result of imperfect, or ‘frustrated’, short-range ($< 1 \text{ nm}$) ion-ion correlations in the bulk electrolyte. It is only when the ion concentration is sufficiently high, that ions of like charge associate at short range in nearly the same manner as ions with opposite charge. We note that, contrary to expectation, the long-range electrostatic decay lengths are not associated with the long-range structure of the radial charge distribution itself (see Figure S1).

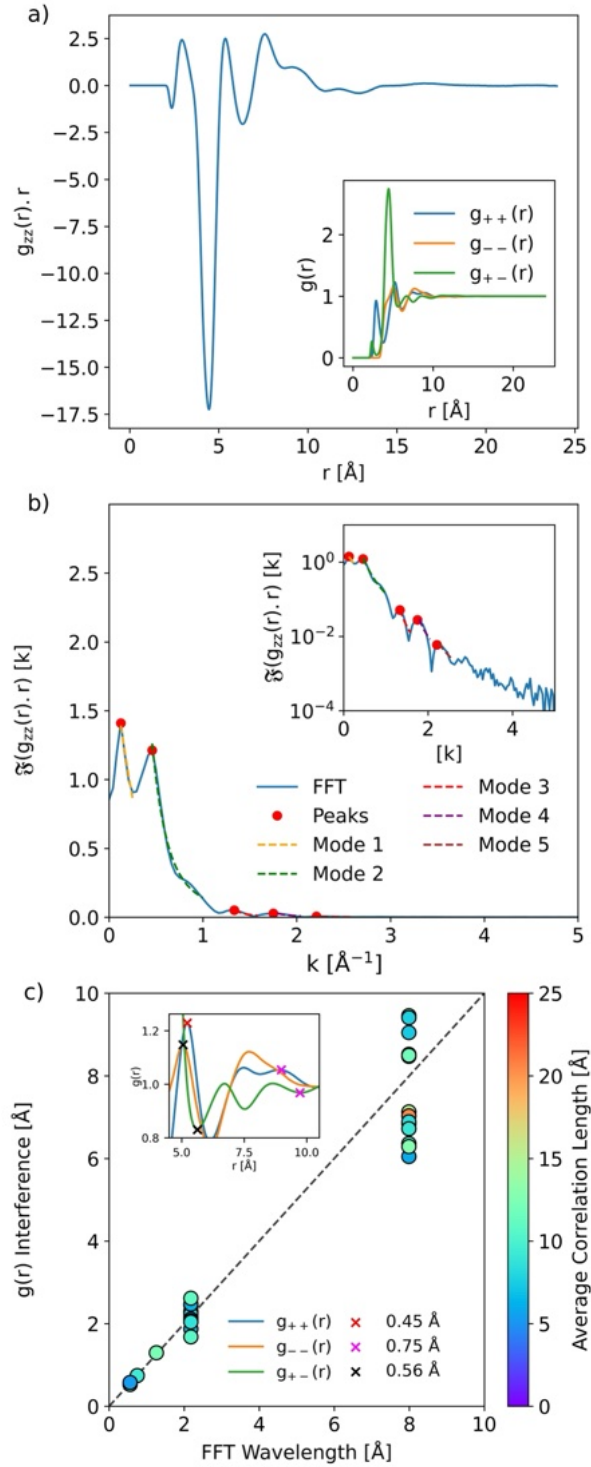


Figure 2. Origins of anomalous screening lengths. (a) $g_{zz}(r) \cdot r$ as a function of radial distance r for 7 M LiCl_(aq). The inset shows the ion-ion correlation functions $g_{++}(r)$, $g_{--}(r)$ and $g_{+-}(r)$ that define $g_{zz}(r)$. (b) Discrete Fourier transform $\mathfrak{F}[g_{zz}(r) \cdot r]$. Individual peaks correspond to distinct electrostatic decay modes and can be fitted using equation 9 to extract screening lengths $1/\kappa_{\mathfrak{R}}$, $1/\kappa'_{\mathfrak{R}}$, $1/\kappa''_{\mathfrak{R}}$, Inset shows the Fourier transform on a log scale. (c) Oscillatory length scales in

the radial charge density are determined by short-range interferences between $g_{++}(r)$, $g_{--}(r)$ and $g_{+-}(r)$ correlation functions (shown inset); the colour scale indicates the average length scale at which the interference occurs. The peaks highlighted in the inset are those discussed in the text.

Results presented in Figure 2 lead us to hypothesise that the relationship between the decay length and spatial frequency of independent decay modes is a general one, observed in all bulk electrolytes. We examine this hypothesis in Figure 3, which presents screening lengths obtained via discrete Fourier analysis of $g_{zz}(r) \cdot r$ for a series of aqueous alkali metal chloride electrolytes, across a range of concentrations ($\sim 0.1 - 9$ M), and ionic liquids. Figure 3 also summarises the experimental values for these electrolytes. Full details of individual $g_{zz}(r) \cdot r$ functions and their discrete Fourier transforms are presented in Supporting Information for all electrolytes.

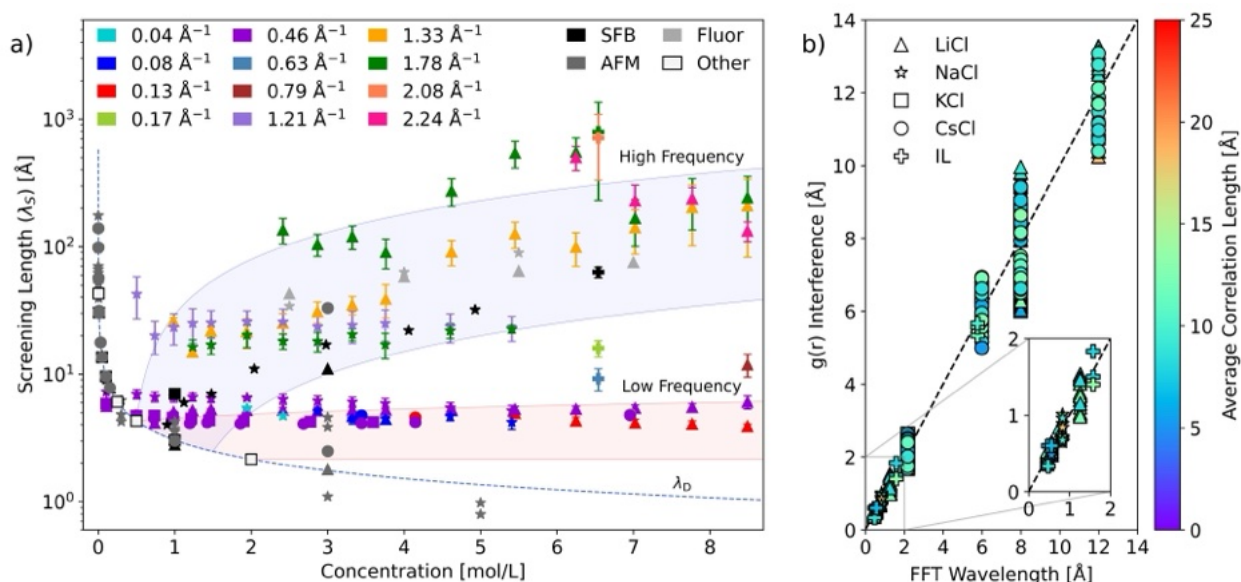


Figure 3. (a) Comparison of experimentally observed screening lengths in concentrated electrolytes and those obtained from the discrete Fourier transform of the radial charge density obtained from molecular dynamics simulations. In all cases, anomalous screening arises from high spatial frequency decay modes in the radial charge density, whereas normal underscreening arises from low spatial frequency decay modes. Predicted screening lengths are coloured according to the spatial frequency of the decay mode, and experimental data is given in greyscale. (b) Oscillatory length scales in the radial charge density are determined by short-range interferences between $g_{++}(r)$, $g_{--}(r)$ and $g_{+-}(r)$ for all electrolytes considered. The colour scale indicates the average length scale at which the interference occurs, as in Figure 2. Symbols in (a) and (b) indicate the electrolyte: \blacktriangle LiCl_(aq), \star NaCl_(aq), \blacksquare KCl_(aq), \bullet CsCl_(aq) and \oplus C₂C₁imBF₄. Experimental data is adapted from references^{19–25} and presented as in Figure 1.

Inspection of Figure 3 immediately confirms our hypothesis – anomalous underscreening is the result of decay modes in the electrostatic potential with high spatial frequencies (short oscillations). For the aqueous alkali metal chloride electrolytes considered, concentrations below the Kirkwood point (~ 0.5 - 1 M) Fourier analysis of $g_{zz}(r) \cdot r$ reveals only a single, low spatial frequency mode, 0.46 \AA^{-1} , common to all electrolytes that yields a screening length in the ‘normal’ range, e.g. $\sim 4.13 \text{ \AA}$ for $0.75 \text{ M LiCl}_{(\text{aq})}$. This mode persists at concentrations above the Kirkwood point. At these concentrations additional higher spatial frequency modes appear and give rise to anomalously large screening lengths. Figure 3b shows that the origin of these low- and high- spatial frequency modes, *viz* the interference between the respective $g_{++}(r)$, $g_{--}(r)$ and $g_{+-}(r)$ correlation functions, is consistent with those discussed above for $7 \text{ M LiCl}_{(\text{aq})}$ in Figure 2c for all electrolytes considered here.

In summary, we have presented an alternative approach to the analysis of the radial charge density in bulk electrolytes that reveals the origins of so-called anomalous underscreening. Discrete Fourier analysis of the radial charge density definitively determines an arbitrary number of decay modes present in the electrostatic potential, and each associated screening length. Below the Kirkwood point, only low spatial frequency decay modes are present. At concentrations above the Kirkwood point however, decay modes comprising high spatial frequency oscillations in the potential are observed. The decay lengths of the latter are consistent with the anomalous screening lengths observed in recent experiments. Analysis of the interference between ion-ion correlation function reveals that decay modes associated with both low and high spatial frequency oscillations in the potential (i.e. ‘normal’ and ‘anomalous’ screening lengths) arise from short-range interference between ion-ion correlation functions, and not long-range correlations in the bulk electrolyte. These results show that the delineation of screening lengths into ‘normal’ and ‘anomalous’ classes is arbitrary, and that, ultimately, there is in fact nothing anomalous about anomalous underscreening.

Acknowledgements

The authors acknowledge Australian Research Council funding (ARC DP190100788, DP230102030). Sophie Baker acknowledges an Australian Government Research Training

Program Scholarship. The authors thank Mr Lachlann Howard for useful discussions. This research was undertaken with the assistance of resources provided at the NCI National Facility systems at the Australian National University, through the National Computational Merit Allocation Scheme supported by the Australian Government.

END MATTER

Computational Methods

Polarisable molecular dynamics (MD) simulations were performed on 50 Å cubic boxes prepared using Packmol⁴⁸. Aqueous systems employed AMOEBA^{49–52} force field, as implemented in the OpenMM⁵³ code. Simulations of [C₂C₁im][BF₄] were performed using the CL&Pol force field^{54,55} as implemented in LAMMPS^{56,57} with the USER-DRUDE⁵⁸ package. Hydrogen atoms were allowed to move freely under AMOEBA, whilst CL&Pol requires H atoms to be constrained using the SHAKE⁵⁹ algorithm. All MD simulations were first equilibrated under the isobaric-isothermal (NPT)^{60–62} ensemble, prior to another under the canonical (NVT)^{60–63} ensemble, before sampling. Full simulation details are in the Supporting Information. Analysis of radial distribution functions was performed using the MDAnalysis^{64,65} package, while visualization was done using Matplotlib.⁶⁶ Calculation of the Fourier transform was completed using the fast Fourier transform module in SciPy.^{67,68}

References

1. Livadiotis, G. in *Kappa Distributions* (ed. Livadiotis, G.) 249–312 (Elsevier, 2017).
2. Kontogeorgis, G. M., Maribo-Mogensen, B. & Thomsen, K. The Debye-Hückel theory and its importance in modeling electrolyte solutions. *Fluid Phase Equilib* **462**, 130–152 (2018).
3. Kjellander, R. A multiple decay-length extension of the Debye-Hückel theory: To achieve high accuracy also for concentrated solutions and explain under-screening in dilute symmetric electrolytes. *Phys Chem Chem Phys* **22**, 23952–23985 (2020).
4. Kjellander, R. The intimate relationship between the dielectric response and the decay of intermolecular correlations and surface forces in electrolytes. *Soft Matter* **15**, 5866–5895 (2019).

5. Kjellander, R. Decay behavior of screened electrostatic surface forces in ionic liquids: The vital role of non-local electrostatics. *Phys Chem Chem Phys* **18**, 18985–19000 (2016).
6. Kjellander, R. Nonlocal electrostatics in ionic liquids: The key to an understanding of the screening decay length and screened interactions. *J Chem Phys* **145**, 124503 (2016).
7. Ramirez, R. & Kjellander, R. Dressed molecule theory for liquids and solutions: An exact charge renormalization formalism for molecules with arbitrary charge distributions. *J Chem Phys* **119**, 11380–11395 (2003).
8. Ulander, J. & Kjellander, R. Screening and asymptotic decay of pair distributions in asymmetric electrolytes. *J Chem Phys* **109**, 9508–9522 (1998).
9. Kirkwood, J. G. Statistical mechanics of liquid solutions. *Chem Rev* **19**, 275–307 (1936).
10. Kirkwood, J. G. Statistical Mechanics of Fluid Mixtures. *J Chem Phys* **3**, 300–313 (1935).
11. Kirkwood, J. G. & Poirier, J. C. The statistical mechanical basis of the Debye-Hückel theory of strong electrolytes. *J Phys Chem* **58**, 591–596 (1954).
12. Coles, S. W. *et al.* Correlation Length in Concentrated Electrolytes: Insights from All-Atom Molecular Dynamics Simulations. *J Phys Chem B* **124**, 1778–1786 (2020).
13. Zeman, J., Kondrat, S. & Holm, C. Bulk ionic screening lengths from extremely large-scale molecular dynamics simulations. *Chem Commun* **56**, 15635–15638 (2020).
14. Zeman, J., Kondrat, S. & Holm, C. Ionic screening in bulk and under confinement. *J Chem Phys* **155**, (2021).
15. Zeidler, A. *et al.* Structure of molten NaCl and the decay of the pair-correlations. *J Chem Phys* **157**, (2022).
16. Cats, P., Evans, R., Härtel, A. & Van Roij, R. Primitive model electrolytes in the near and far field: Decay lengths from DFT and simulations. *J Chem Phys* **154**, (2021).
17. Krucker-Velasquez, E. & Swan, J. W. Underscreening and hidden ion structures in large scale simulations of concentrated electrolytes. *J Chem Phys* **155**, (2021).
18. Leote De Carvalho, R. J. F. & Evans, R. The decay of correlations in ionic fluids. *Mol Phys* **83**, 619–654 (1994).
19. Baimpos, T., Shrestha, B. R., Raman, S. & Valtiner, M. Effect of interfacial ion structuring on range and magnitude of electric double layer, hydration, and adhesive interactions between mica surfaces in 0.05-3 M Li⁺ and Cs⁺ electrolyte solutions. *Langmuir* **30**, 4322–4332 (2014).

20. Kumar, S. *et al.* Absence of anomalous underscreening in highly concentrated aqueous electrolytes confined between smooth silica surfaces. *J Colloid Interface Sci* **622**, 819–827 (2022).
21. Smith, A. M., Maroni, P., Trefalt, G. & Borkovec, M. Unexpectedly large decay lengths of double-layer forces in solutions of symmetric, multivalent electrolytes. *J Phys Chem B* **123**, 1733–1740 (2019).
22. Smith, A. M., Lee, A. A. & Perkin, S. The Electrostatic Screening Length in Concentrated Electrolytes Increases with Concentration. *J Phys Chem Lett* **7**, 2157–2163 (2016).
23. Robertson, H. *et al.* Underscreening in concentrated electrolytes: re-entrant swelling in polyelectrolyte brushes. *Phys Chem Chem Phys*, **25**, 24770-24782 (2023).
24. Gaddam, P. & Ducker, W. Electrostatic Screening Length in Concentrated Salt Solutions. *Langmuir* **35**, 5719–5727 (2019).
25. Pashley, R. M. & Israelachvili, J. N. Molecular layering of water in thin films between mica surfaces and its relation to hydration forces. *J Colloid Interface Sci* **101**, 511–523 (1984).
26. Elliott, G. R. *et al.* The known-unknowns of anomalous underscreening in concentrated electrolytes. *Chem Phys Lett*, **843**, 141190 (2024)
27. Hjalmarsson, N., Atkin, R. & Rutland, M. W. Switchable long-range double layer force observed in a protic ionic liquid. *Chem Commun* **53**, 647–650 (2017).
28. Liu, G., Parsons, D. & Craig, V. S. J. Re-entrant swelling and redissolution of polyelectrolytes arises from an increased electrostatic decay length at high salt concentrations. *J Colloid Interface Sci* **579**, 369–378 (2020).
29. Yuan, H., Deng, W., Zhu, X., Liu, G. & Craig, V. S. J. Colloidal Systems in Concentrated Electrolyte Solutions Exhibit Re-entrant Long-Range Electrostatic Interactions due to Underscreening. *Langmuir* **38**, 6164–6173 (2022).
30. Kumar, S., Yadav, I., Abbas, S., Aswal, V. K. & Kohlbrecher, J. Interactions in reentrant phase behavior of a charged nanoparticle solution by multivalent ions. *Phys Rev E* **96**, 2–6 (2017).
31. Zhang, X. *et al.* Long-Range Interactions in Salt-in-Ionic Liquids. *ChemRxiv* (2024). DOI: 10.26434/chemrxiv-2024-hs7sf
32. Huang, J. Confinement Induced Dilution: Electrostatic Screening Length Anomaly in Concentrated Electrolytes in Confined Space. *J Phys Chem C* **122**, 3428–3433 (2018).
33. Berlinger, S. A. *et al.* Cation valency in water-in-salt electrolytes alters the short- and long-range structure of the electrical double layer. *Proc Natl Acad Sci* **121**, 2017 (2024).

34. Kim, J. & Rotenberg, B. Donnan equilibrium in charged slit-pores from a hybrid nonequilibrium molecular dynamics/Monte Carlo method with ions and solvent exchange. *J Chem Phys* **161**, (2024).
35. Jäger, H. *et al.* A screening of results on the decay length in concentrated electrolytes. *Faraday Discuss* **246**, 520-539 (2023).
36. Safran, S. A. & Pincus, P. Scaling Perspectives of Underscreening in Concentrated Electrolyte Solutions. *Soft Matter* **1**, 1–285 (2023).
37. Härtel, A., Bültmann, M. & Coupette, F. Anomalous Underscreening in the Restricted Primitive Model. *Phys Rev Lett* **130**, 108202 (2022).
38. Elliott, G. R. *et al.* Dynamic Ion Correlations and Ion-Pair Lifetimes in Aqueous Alkali Metal Chloride Electrolytes. *J Phys Chem B* **128**, 7438–7444 (2024).
39. Apostol, M. Screening length in concentrated electrolytes. *Chem Phys* **558**, 111514 (2022).
40. Zarubin, G. & Bier, M. Static dielectric properties of dense ionic fluids. *J Chem Phys* **142**, 184502 (2015).
41. Gregory, K. P., Wanless, E. J., Webber, G. B. & Craig, V. S. J., Page, A. J., A First-Principles Alternative to Empirical Solvent Parameters. *Phys Chem Chem Phys* **26**, 20750-20759 (2024).
42. Lee, A. A., Perez-Martinez, C. S., Smith, A. M. & Perkin, S. Scaling Analysis of the Screening Length in Concentrated Electrolytes. *Phys Rev Lett* **119**, 1–5 (2017).
43. Lee, A. A., Perez-Martinez, C. S., Smith, A. M. & Perkin, S. Underscreening in concentrated electrolytes. *Faraday Discuss* **199**, 239–259 (2017).
44. Fung, C. Static and dynamic behaviour of ionic liquid films studied with the surface force apparatus. (University of South Australia, 2022). <https://hdl.handle.net/11541.2/27912>.
45. Kjellander, R. *Statistical Mechanics of Liquids and Solutions. Statistical Mechanics of Liquids and Solutions* (CRC Press, 2019).
46. Kjellander, R. Oscillatory and long-range monotonic exponential decays of electrostatic interactions in ionic liquids and other electrolytes: The significance of dielectric permittivity and renormalized charges. *J Chem Phys* **148**, (2018).
47. Groves, T. & Perkin, S. Wave mechanics in an ionic liquid mixture. *Faraday Discuss* (2024) DOI:10.1039/D4FD00040D.

48. Martínez, L., Andrade, R., Birgin, E. G. & Martínez, J. M. PACKMOL: A package for building initial configurations for molecular dynamics simulations. *J Comput Chem* **30**, 2157–2164 (2009).
49. Laury, M. L., Wang, L. P., Pande, V. S., Head-Gordon, T. & Ponder, J. W. Revised Parameters for the AMOEBA Polarizable Atomic Multipole Water Model. *J Phys Chem B* **119**, 9423–9437 (2015).
50. Ren, P. & Ponder, J. W. Polarizable Atomic Multipole Water Model for Molecular Mechanics Simulation. *J Phys Chem B* **107**, 5933–5947 (2003).
51. Wang, Z. Polarizable Force Field Development, and Applications to Conformational Sampling and Free Energy Calculations. (Washington University, 2018). DOI: 10.7936/axj9-k915
52. Ponder, J. W. *et al.* Current status of the AMOEBA polarizable force field. *J Phys Chem B* **114**, 2549–2564 (2010).
53. Eastman, P. *et al.* OpenMM 8: Molecular Dynamics Simulation with Machine Learning Potentials. *J Phys Chem B* **128**, 109–116 (2024).
54. Goloviznina, K., Gong, Z. & Padua, A. A. H. The CL&Pol polarizable force field for the simulation of ionic liquids and eutectic solvents. *WIREs Comput Mol Sci* **12**, (2022).
55. Goloviznina, K., Canongia Lopes, J. N., Costa Gomes, M. & Pádua, A. A. H. Transferable, Polarizable Force Field for Ionic Liquids. *J Chem Theory Comput* **15**, 5858–5871 (2019).
56. Plimpton Steve. Fast Parallel Algorithms for Short-Range Molecular Dynamics. *Journal of Computation Physics* **117**, 1–19 (1995).
57. Thompson, A. P. *et al.* LAMMPS - a flexible simulation tool for particle-based materials modeling at the atomic, meso, and continuum scales. *Comput Phys Commun* **271**, 108171 (2022).
58. Dequidt, A., Devémy, J. & Pádua, A. A. H. Thermalized Drude Oscillators with the LAMMPS Molecular Dynamics Simulator. *J Chem Inf Model* **56**, 260–268 (2016).
59. Ryckaert, J. P., Ciccotti, G. & Berendsen, H. J. C. Numerical integration of the cartesian equations of motion of a system with constraints: molecular dynamics of n-alkanes. *J Comput Phys* **23**, 327–341 (1977).
60. Martyna, G. J., Klein, M. L. & Tuckerman, M. Nosé-Hoover chains: The canonical ensemble via continuous dynamics. *J Chem Phys* **97**, 2635–2643 (1992).
61. Nosé, S. A unified formulation of the constant temperature molecular dynamics methods. *J Chem Phys* **81**, 511–519 (1984).

62. Hoover, W. G. Canonical dynamics: Equilibrium phase-space distributions. *Phys Rev A* **31**, 1695–1697 (1985).
63. Åqvist, J., Wennerström, P., Nervall, M., Bjelic, S. & Brandsdal, B. O. Molecular dynamics simulations of water and biomolecules with a Monte Carlo constant pressure algorithm. *Chem Phys Lett* **384**, 288–294 (2004).
64. Gowers, R. *et al.* MDAnalysis: A Python Package for the Rapid Analysis of Molecular Dynamics Simulations. *Proceedings of the 15th Python in Science Conference* 98–105 (2016) DOI:10.25080/majora-629e541a-00e.
65. Michaud-Agrawal, N., Denning, E. J., Woolf, T. B. & Beckstein, O. MDAnalysis: A toolkit for the analysis of molecular dynamics simulations. *J Comput Chem* **32**, 2319–2327 (2011).
66. Hunter, J. D. Matplotlib: A 2D Graphics Environment. *Comput Sci Eng* **9**, 90–95 (2007).
67. Virtanen, P. *et al.* SciPy 1.0: fundamental algorithms for scientific computing in Python. *Nat Methods* **17**, 261–272 (2020).
68. Cooley, J. W. & Tukey, J. W. An algorithm for the machine calculation of complex Fourier series. *Math Comput* **19**, 297–301 (1965).

There is Nothing Anomalous about “Anomalous” Underscreening in Concentrated Electrolytes

Sophie Baker^{†,1}, Gareth R. Elliott^{†,1}, Erica J. Wanless¹, Grant B. Webber², Vincent S. J. Craig³,
Alister J. Page^{*1}

¹*Discipline of Chemistry, The University of Newcastle, Callaghan, New South Wales 2308, Australia*

²*Discipline of Chemical Engineering, The University of Newcastle, Callaghan, New South Wales 2308, Australia*

³*Department of Material Physics, Research School of Physics, Australian National University, Canberra, ACT 0200
Australia*

Supporting Information

Table of Contents

<i>Ion Correlation Interference Analysis</i>	2
<i>Long Range Ion Correlation Analysis</i>	4
<i>Molecular Dynamics Simulation Details</i>	5
Aqueous Alkali Metal Chlorides.....	5
Ionic Liquid: [C ₂ C ₁ im][BF ₄]	5
References	5
<i>Conventional Derivation of λ_s</i>	7
Lithium Chloride.....	7
Sodium Chloride	17
Potassium Chloride	25
Cesium Chloride	31
Ionic Liquid: [C ₂ C ₁ im][BF ₄]	38
<i>Derivation of λ_s via Discrete Fourier Analysis of $g_{zz}(r).r$</i>	39
Lithium Chloride.....	39
Sodium Chloride	46
Potassium Chloride.....	52
Cesium Chloride	56
Ionic Liquid: [C ₂ C ₁ im][BF ₄]	61

Ion Correlation Interference Analysis

Table S1. Short-range interference ($< 1 \text{ \AA}$) between $g_{++}(r)$, $g_{--}(r)$ and $g_{+-}(r)$ correlation functions produce the oscillatory wavelengths associated with high-frequency (anomalous) decay modes in the electrostatic potential. Mode 3, 4 and 5 refer to Figure 2b in the main text.

Mode 3 ($\lambda_s = 141 \pm 53 \text{ \AA}$)			Mode 4 ($\lambda_s = 167 \pm 66 \text{ \AA}$)			Mode 5 ($\lambda_s = 229 \pm 74 \text{ \AA}$)		
Interference (\AA)	Interfering Correlations	Average Correlation Length (\AA)	Interference (\AA)	Interfering Correlations	Average Correlation Length (\AA)	Interference (\AA)	Interfering Correlations	Average Correlation Length (\AA)
0.74	$g(r)_{+-} / g(r)_{++}$	9.36	0.53	$g(r)_{+-} / g(r)_{++}$	11.68	0.41	$g(r)_{+-} / g(r)_{++}$	5.42
			0.58	$g(r)_{+-} / g(r)_{--}$	5.34	0.53	$g(r)_{+-} / g(r)_{++}$	11.68
						0.41	$g(r)_{+-} / g(r)_{--}$	12.14

Table S2. Longer-range interference between $g_{++}(r)$, $g_{--}(r)$ and $g_{+-}(r)$ correlation functions produce the oscillatory wavelengths associated with the low-frequency (normal) decay modes. Mode 1 and 2 refer to Figure 2b in the main text.

Mode 1 ($\lambda_s = 4.15 \pm 0.26 \text{ \AA}$)			Mode 2 ($\lambda_s = 5.42 \pm 0.31 \text{ \AA}$)		
Interference (\AA)	Interfering Correlations	Average Correlation Length (\AA)	Interference (\AA)	Interfering Correlations	Average Correlation Length (\AA)
9.46	$g(r)-- / g(r)++$	13.79	2.16	$g(r)-- / g(r)++$	6.50
7.13	$g(r)-- / g(r)++$	14.96	2.47	$g(r)-- / g(r)++$	10.30
8.52	$g(r)-- / g(r)++$	19.77	2.45	$g(r)-- / g(r)++$	8.80
7.03	$g(r)-- / g(r)++$	20.51	2.28	$g(r)+- / g(r)++$	4.08
6.36	$g(r)-- / g(r)++$	9.55	2.30	$g(r)+- / g(r)++$	6.37
6.84	$g(r)+- / g(r)++$	6.31	1.87	$g(r)+- / g(r)++$	6.56
9.05	$g(r)+- / g(r)++$	7.42	2.23	$g(r)+- / g(r)++$	8.62
6.72	$g(r)+- / g(r)++$	8.58	1.68	$g(r)+- / g(r)++$	10.57
6.05	$g(r)+- / g(r)++$	5.96	2.11	$g(r)+- / g(r)--$	4.00
8.47	$g(r)+- / g(r)++$	7.18	2.47	$g(r)+- / g(r)--$	6.29
6.89	$g(r)+- / g(r)--$	8.50	2.06	$g(r)+- / g(r)--$	6.66
9.41	$g(r)+- / g(r)--$	7.64	2.04	$g(r)+- / g(r)--$	8.71
6.72	$g(r)+- / g(r)--$	8.99	2.62	$g(r)+- / g(r)--$	11.04
8.50	$g(r)+- / g(r)--$	11.77			
6.29	$g(r)+- / g(r)--$	12.88			

Long Range Ion Correlation Analysis

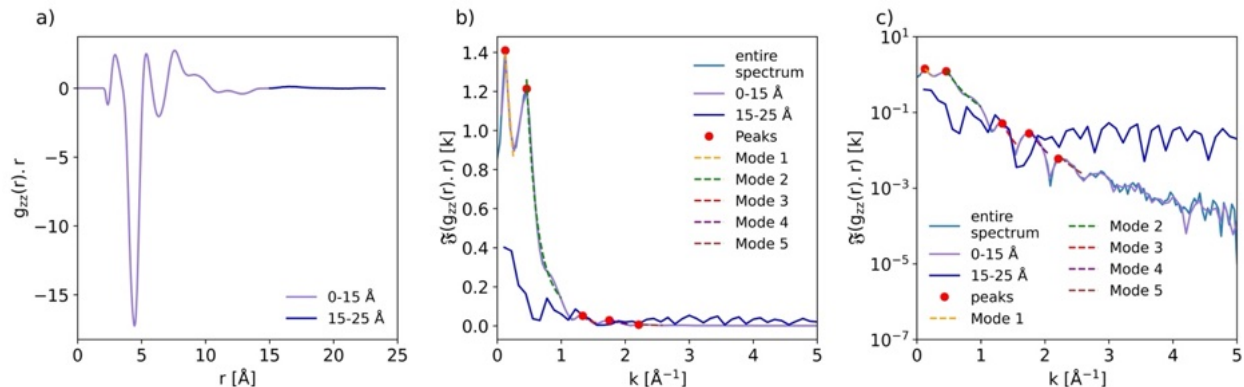


Figure S1. Long-range decay lengths are not associated with the long-range structure of the radial charge distribution. This is shown here by performing the discrete Fourier transform of $g_{zz}(r) \cdot r$ within specific length scales (0-15 Å (blue) and 15-25 Å (yellow)) for 7 M LiCl. The features of $\mathcal{F}[|g_{zz}(r)| \cdot r](k)$ that give rise to ‘anomalous’ long-range screening lengths are resolved using only the first 15 Å. (a) $g_{zz}(r) \cdot r$ (b) $\mathcal{F}[|g_{zz}(r)| \cdot r](k)$ and (c) $\mathcal{F}[|g_{zz}(r)| \cdot r](k)$ on a log scale.

Molecular Dynamics Simulation Details

Aqueous Alkali Metal Chlorides

Polarisable molecular dynamics calculations of aqueous systems have been detailed previously¹. Briefly, periodic simulation boxes were prepared with a volume of approximately 50x50x50 Å with 4167 water molecules, and the required number of ion pairs to create a given concentration (listed below). Four independent simulations at each concentration were prepared with randomly initialised coordinates by the packmol² tool. After an energy minimisation, simulations were then run using the Atomic Multipole Optimized Energetics for Biomolecular Applications (AMOEBA) force field³ as implemented in OpenMM⁴. Each of the independent simulations used the isobaric-isothermal (NpT) ensemble to relax and equilibrate the density. After equilibration, the average volume was then determined from the last 500 ps, and the box fixed at this size. The coordinates were then equilibrated under the canonical (NVT) ensemble prior to sampling, which was done for 2 ns for each replica (totally 8 ns of sampling). All stages of the simulations used a timestep of 1 fs to propagate the equations of motion. All simulations employed the water parameters of Ren et al.⁵, while the ion parameters were obtained from the thesis of Wang⁶.

Ionic Liquid: [C₂C₁im][BF₄]

MD simulations of [C₂C₁im][BF₄] were initialised using a 50 Å periodic cubic box containing 150 ion pairs with starting configurations and input files generated using Packmol². We employ the CL&Pol polarisable force-field of Padua et al.^{7,8}, via LAMMPS^{9,10} with the USER-DRUDE¹¹ package. Polarisability was included explicitly following Padua et al.^{7,8}, with Drude induced dipoles consisting of positively charged Drude core and a negatively charged Drude particle of mass 0.40 a.u and spring constant $k_D = 4184$ kJ/mol. Only heavy atoms were made polarisable; polarisability of hydrogen atoms was merged onto neighbouring atoms. The point charges of the dipoles were evaluated from atomic polarisabilities as $\alpha = \frac{q_D^2}{k_D}$. Short-range dipole-dipole interactions were damped using the Thole function with $a = 2.6$. The non-bonded attractive energies were used unchanged from the original parameter set, and employed a cut off of 12 Å for pair potentials with tail corrections applied. Bonds terminating in hydrogen atoms were constrained using the SHAKE algorithm¹². A 0 K energy minimization was first performed, followed by a 2 ns NPT equilibration at 300 K and 1 bar. Then a 50 ns NVT production run was performed at 300 K. The temperature and pressure were maintained using a Nosé-Hoover thermostat and barostat^{13–15}, with a 1 fs timestep and dumping the trajectory every 1000 frames.

References

1. Elliott, G. R. *et al.* Dynamic Ion Correlations and Ion-Pair Lifetimes in Aqueous Alkali Metal Chloride Electrolytes. *J Phys Chem B* (2024) doi:10.1021/acs.jpcc.4c01992.
2. Martínez, L., Andrade, R., Birgin, E. G. & Martínez, J. M. PACKMOL: A package for building initial configurations for molecular dynamics simulations. *J Comput Chem* **30**, 2157–2164 (2009).

3. Ponder, J. W. *et al.* Current status of the AMOEBA polarizable force field. *Journal of Physical Chemistry B* **114**, 2549–2564 (2010).
4. Eastman, P. *et al.* OpenMM 8: Molecular Dynamics Simulation with Machine Learning Potentials. *Journal of Physical Chemistry B* **128**, 109–116 (2024).
5. Ren, P. & Ponder, J. W. Polarizable Atomic Multipole Water Model for Molecular Mechanics Simulation. *J Phys Chem B* **107**, 5933–5947 (2003).
6. Wang, Z. Polarizable Force Field Development, and Applications to Conformational Sampling and Free Energy Calculations. (Washington University, 2018).
7. Goloviznina, K., Gong, Z. & Padua, A. A. H. The CL&Pol polarizable force field for the simulation of ionic liquids and eutectic solvents. *WIREs Comput Mol Sci* **12**, (2022).
8. Goloviznina, K., Canongia Lopes, J. N., Costa Gomes, M. & Pádua, A. A. H. Transferable, Polarizable Force Field for Ionic Liquids. *J Chem Theory Comput* **15**, 5858–5871 (2019).
9. Thompson, A. P. *et al.* LAMMPS - a flexible simulation tool for particle-based materials modeling at the atomic, meso, and continuum scales. *Comput Phys Commun* **271**, 108171 (2022).
10. Plimpton, S. & Plimpton Steve. Fast parallel algorithms for short-range molecular dynamics. *J Comput Phys* **117**, 1–19 (1995).
11. Dequidt, A., Devémy, J. & Pádua, A. A. H. Thermalized Drude Oscillators with the LAMMPS Molecular Dynamics Simulator. *J Chem Inf Model* **56**, 260–268 (2016).
12. Ryckaert, J. P., Ciccotti, G. & Berendsen, H. J. C. Numerical integration of the cartesian equations of motion of a system with constraints: molecular dynamics of n-alkanes. *J Comput Phys* **23**, 327–341 (1977).
13. Martyna, G. J., Tobias, D. J. & Klein, M. L. Constant pressure molecular dynamics algorithms. *J Chem Phys* **101**, 4177–4189 (1994).
14. Nosé, S. A unified formulation of the constant temperature molecular dynamics methods. *J Chem Phys* **81**, 511–519 (1984).
15. Hoover, W. G. Canonical dynamics: Equilibrium phase-space distributions. *Phys Rev A (Coll Park)* **31**, 1695–1697 (1985).

Conventional Derivation of λ_5

Lithium Chloride

Table S3. Concentrations and conventionally-derived λ_5 values for aqueous LiCl simulations (see Figures S2-S18).

Conc (m)	Conc (M)	Decay Length (Å)
0.1	0.11	8.13 ± 0.17
0.5	0.50	3.38 ± 0.39
0.75	0.74	2.68 ± 0.10
1.0	0.99	2.09 ± 0.04
1.25	1.23	2.00 ± 0.08
1.5	1.47	2.04 ± 0.11
2.0	1.94	1.82 ± 0.10
2.5	2.42	2.18 ± 0.24
3.0	2.87	1.87 ± 0.07
3.5	3.32	1.95 ± 0.16
4.0	3.76	2.10 ± 0.14
5.0	4.62	2.27 ± 0.09
6.0	5.45	2.30 ± 0.18
7.0	6.25	3.16 ± 0.39
8.0	7.02	3.38 ± 0.39
9.0	7.77	3.25 ± 0.30
10.0	8.49	3.62 ± 0.59

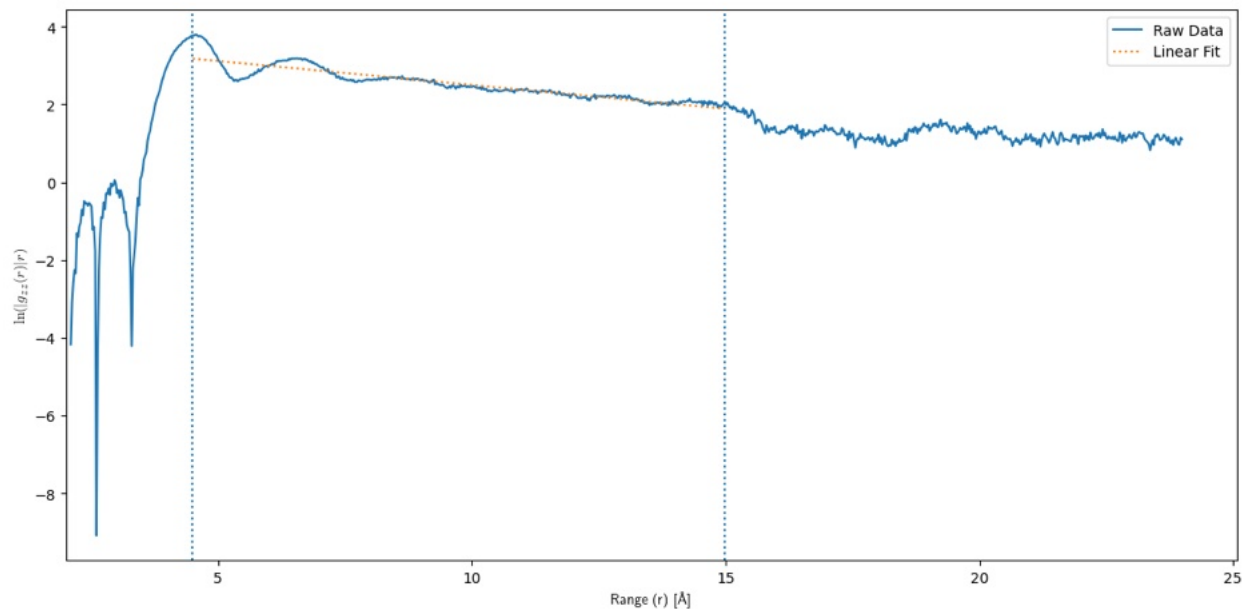


Figure S2. Fitting of aqueous LiCl at a concentration of 0.11 M. In this instance, because of the presence of a plateau in the data, a single straight line was used to fit to the points, rather than fitting the peaks. The vertical lines indicate the extrema that fitting was carried out over.

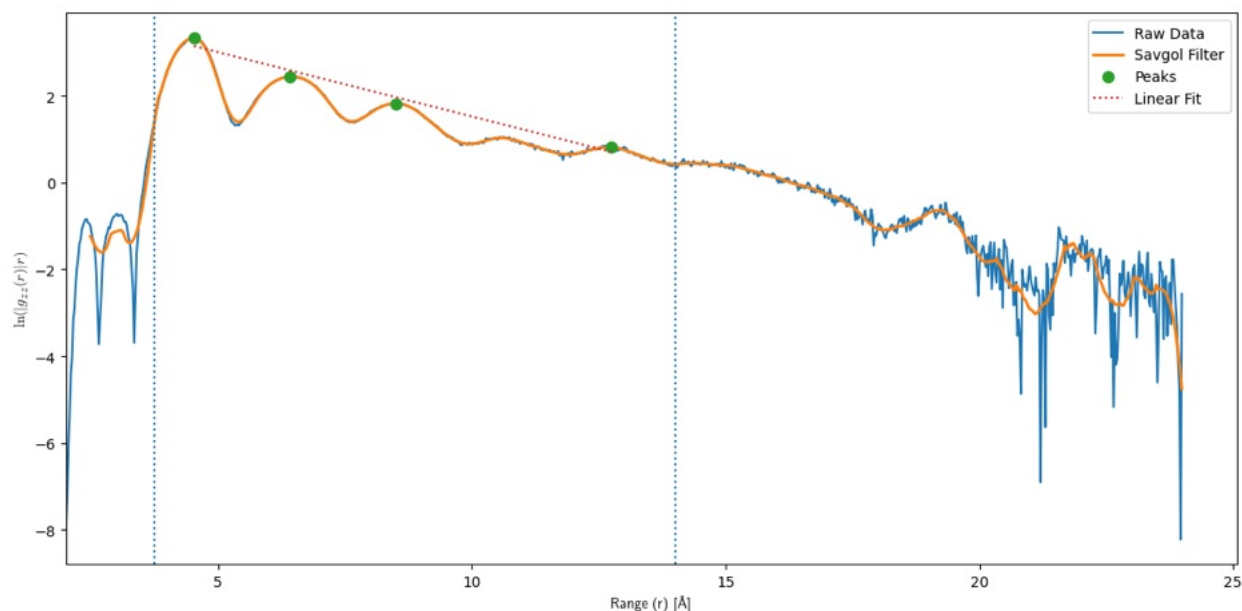


Figure S3. Fitting of aqueous LiCl at a concentration of 0.50 M. The envelope of the fit is determined by fitting through points at the top of each of the marked peaks. A Savgol filter was applied to smooth the data to assist peak finding, particularly at higher values of r . The vertical lines indicate the extrema that fitting was carried out over.

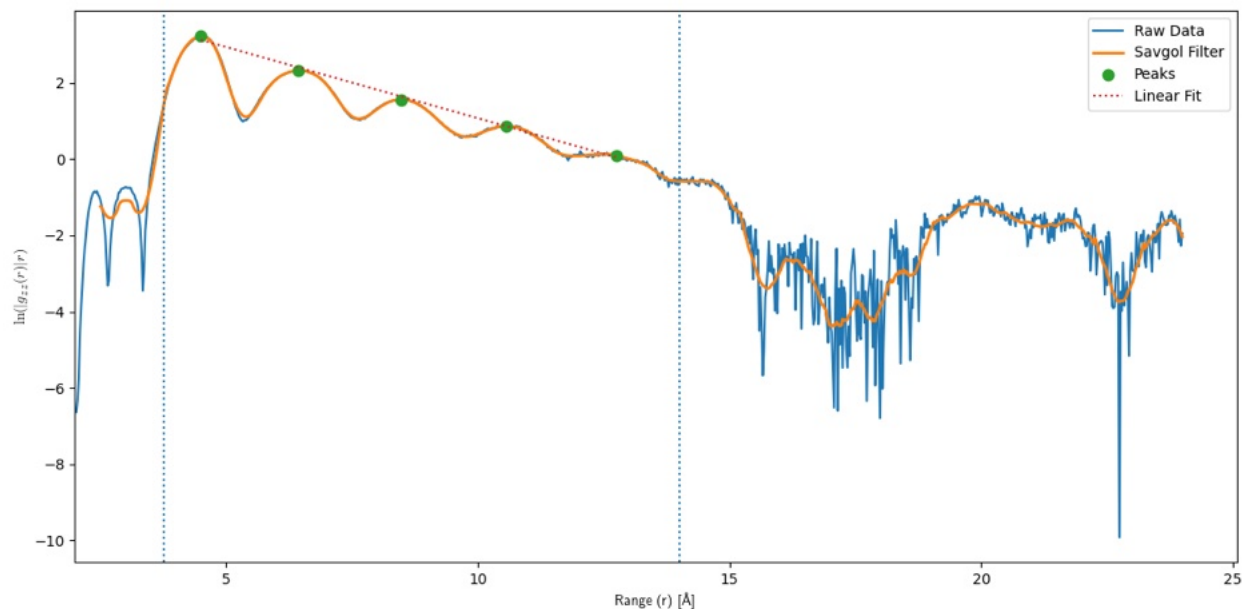


Figure S4. Fitting of aqueous LiCl at a concentration of 0.74 M. The envelope of the fit is determined by fitting through points at the top of each of the marked peaks. A Savgol filter was applied to smooth the data to assist peak finding, particularly at higher values of r . The vertical lines indicate the extrema that fitting was carried out over.

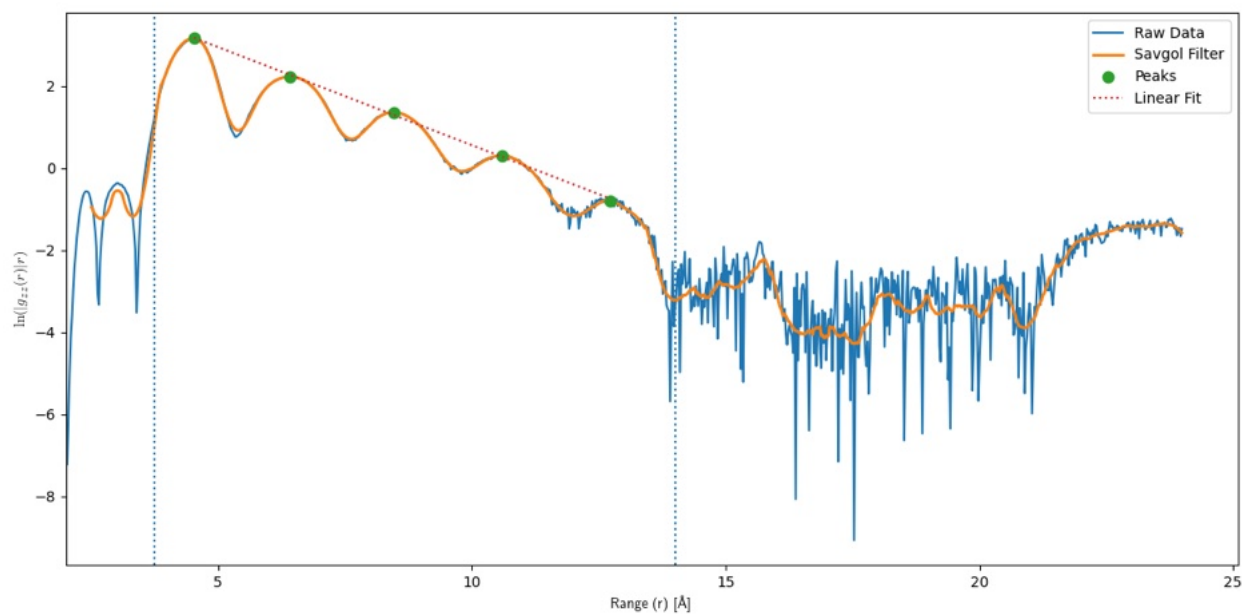


Figure S5. Fitting of aqueous LiCl at a concentration of 0.99 M. The envelope of the fit is determined by fitting through points at the top of each of the marked peaks. A Savgol filter was applied to smooth the data to assist peak finding, particularly at higher values of r . The vertical lines indicate the extrema that fitting was carried out over.

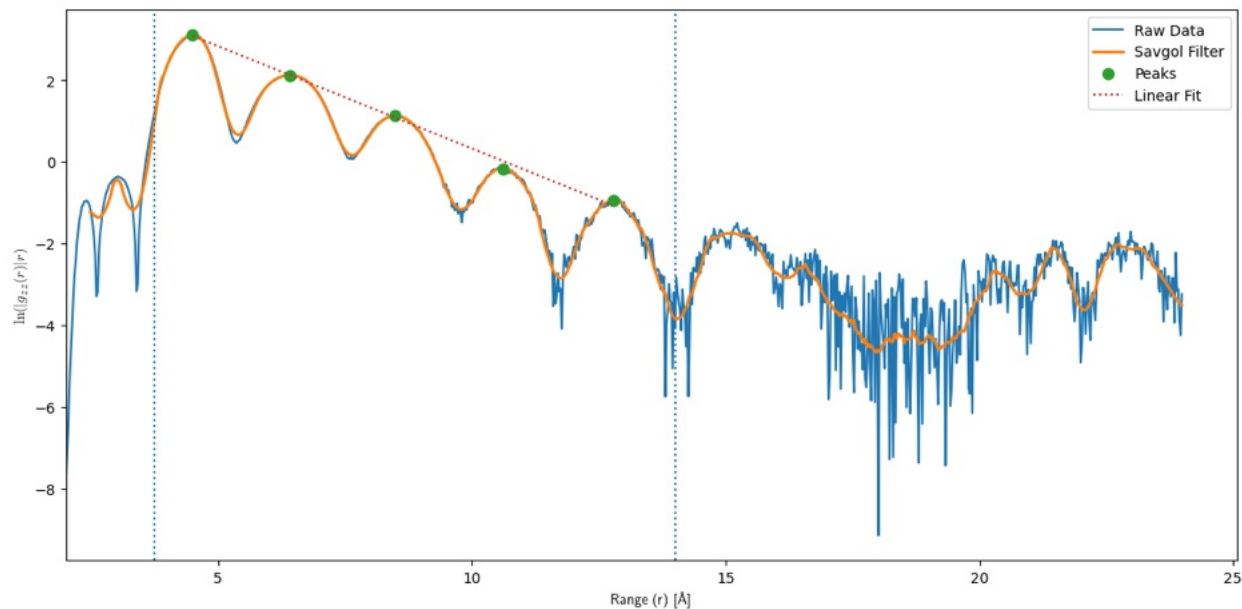


Figure S6. Fitting of aqueous LiCl at a concentration of 1.23 M. The envelope of the fit is determined by fitting through points at the top of each of the marked peaks. A Savgol filter was applied to smooth the data to assist peak finding, particularly at higher values of r . The vertical lines indicate the extrema that fitting was carried out over.

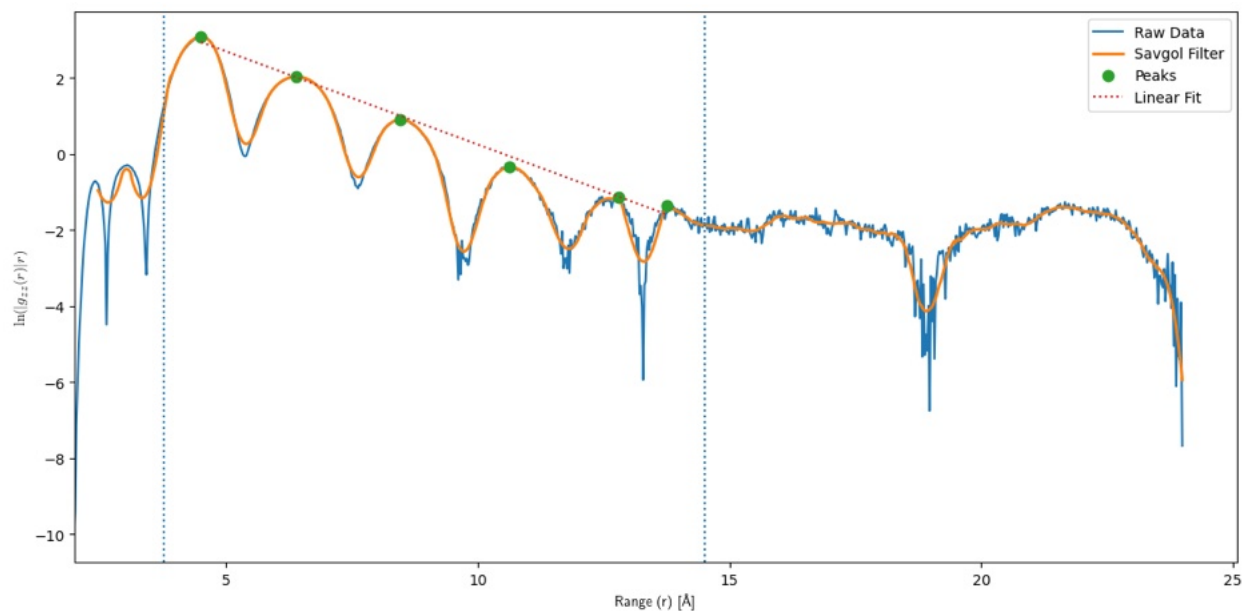


Figure S7. Fitting of aqueous LiCl at a concentration of 1.47 M. The envelope of the fit is determined by fitting through points at the top of each of the marked peaks. A Savgol filter was applied to smooth the data to assist peak finding, particularly at higher values of r . The vertical lines indicate the extrema that fitting was carried out over.

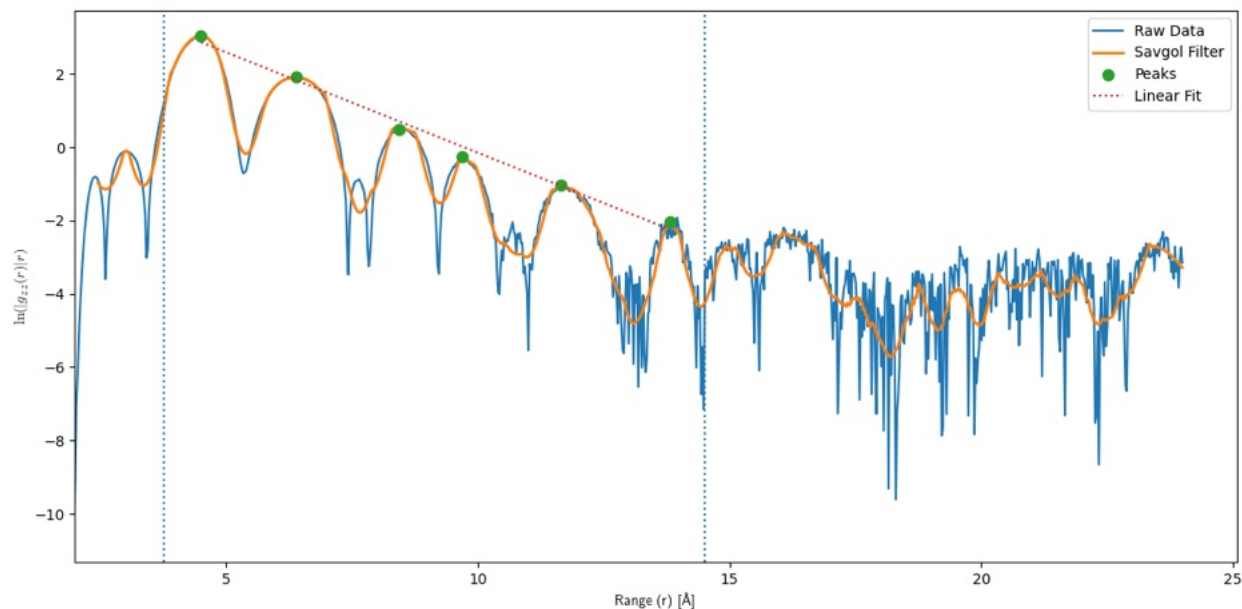


Figure S8. Fitting of aqueous LiCl at a concentration of 1.94 M. The envelope of the fit is determined by fitting through points at the top of each of the marked peaks. A Savgol filter was applied to smooth the data to assist peak finding, particularly at higher values of r . The vertical lines indicate the extrema that fitting was carried out over.

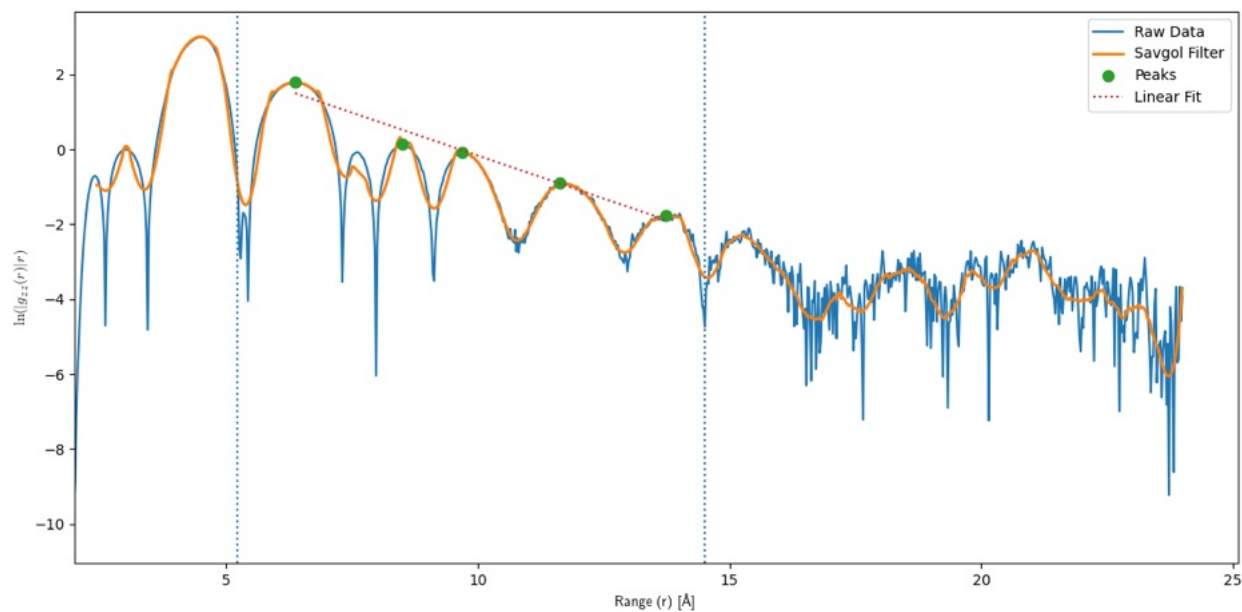


Figure S9. Fitting of aqueous LiCl at a concentration of 2.42 M. The envelope of the fit is determined by fitting through points at the top of each of the marked peaks. A Savgol filter was applied to smooth the data to assist peak finding, particularly at higher values of r . The vertical lines indicate the extrema that fitting was carried out over.

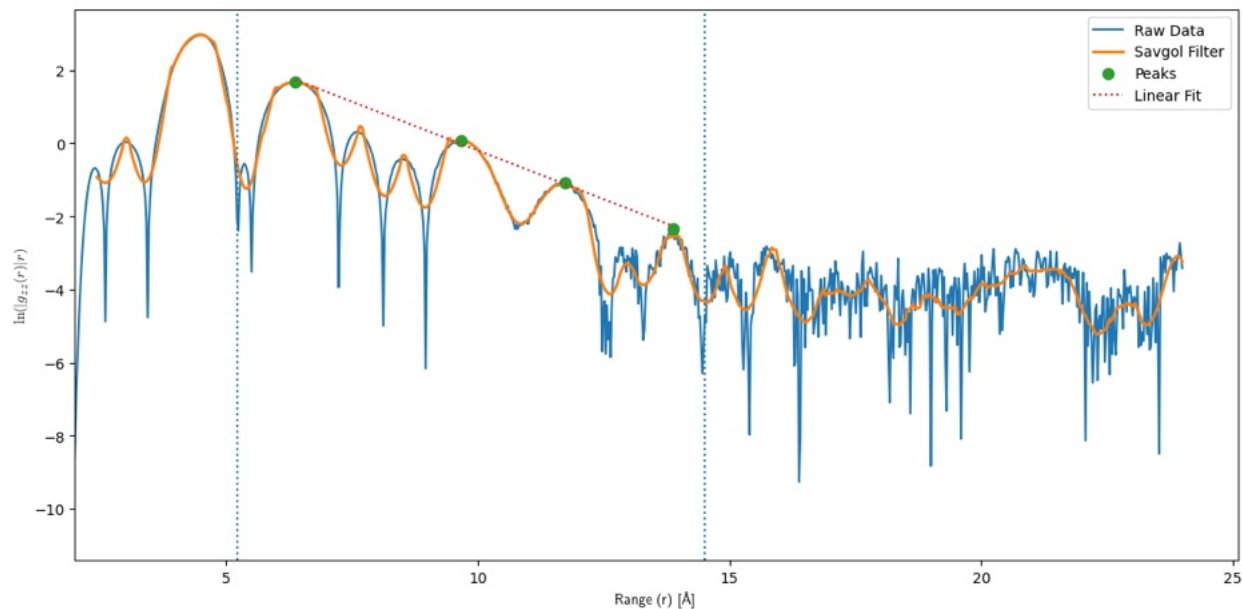


Figure S10. Fitting of aqueous LiCl at a concentration of 2.87 M. The envelope of the fit is determined by fitting through points at the top of each of the marked peaks. A Savgol filter was applied to smooth the data to assist peak finding, particularly at higher values of r . The vertical lines indicate the extrema that fitting was carried out over.

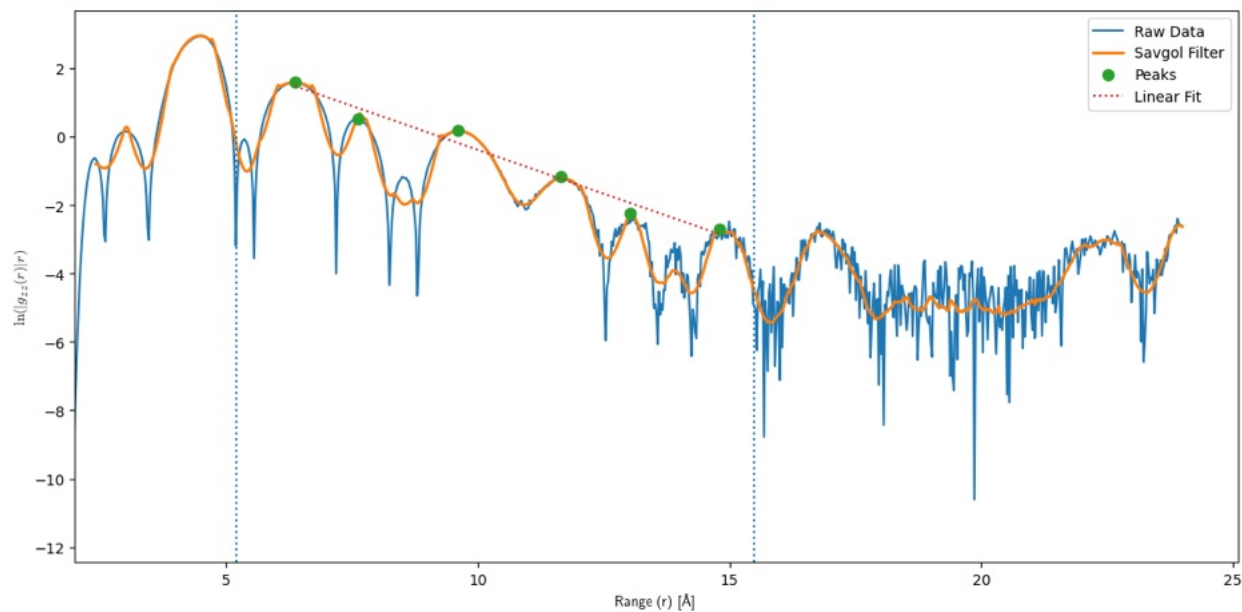


Figure S11. Fitting of aqueous LiCl at a concentration of 3.32 M. The envelope of the fit is determined by fitting through points at the top of each of the marked peaks. A Savgol filter was applied to smooth the data to assist peak finding, particularly at higher values of r . The vertical lines indicate the extrema that fitting was carried out over.

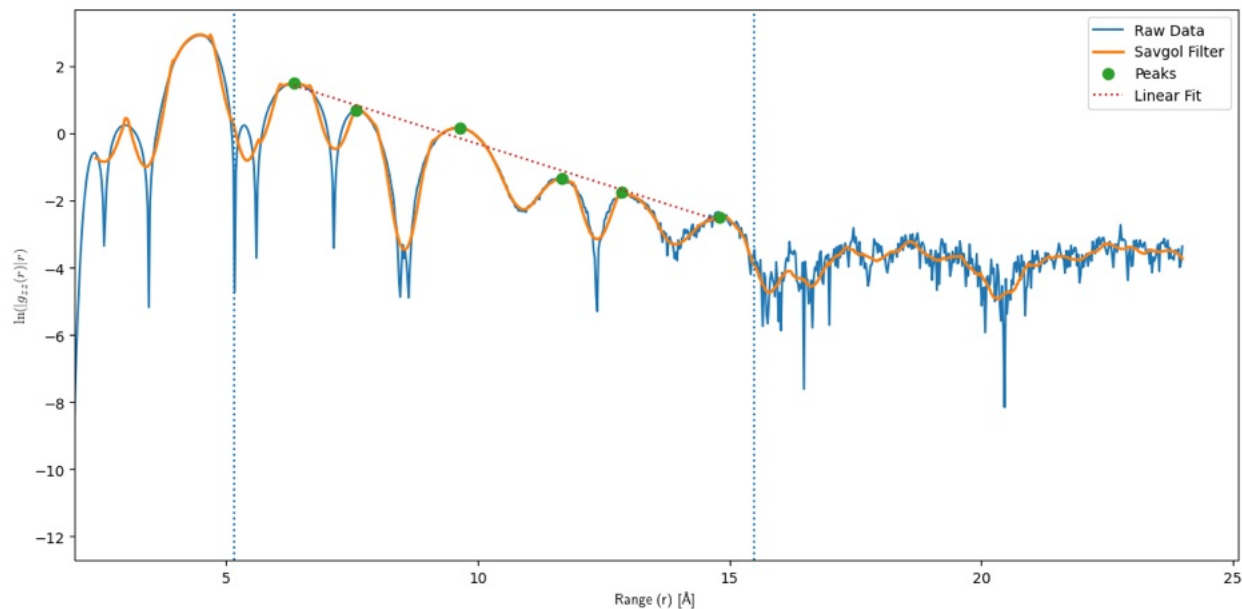


Figure S12. Fitting of aqueous LiCl at a concentration of 3.76 M. The envelope of the fit is determined by fitting through points at the top of each of the marked peaks. A Savgol filter was applied to smooth the data to assist peak finding, particularly at higher values of r . The vertical lines indicate the extrema that fitting was carried out over.

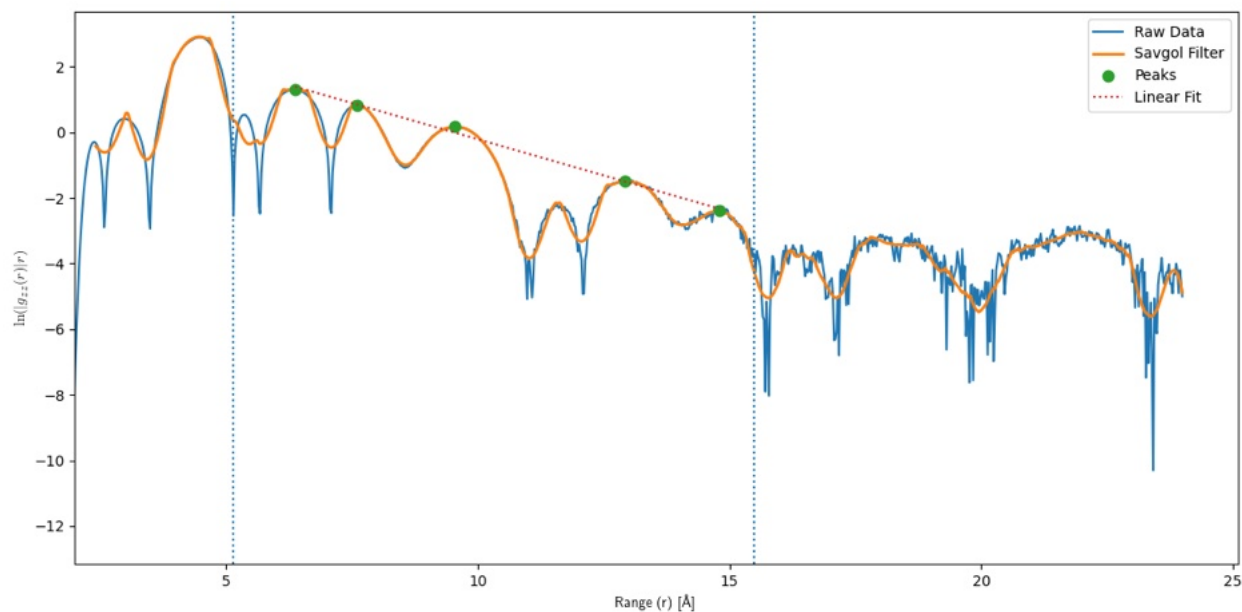


Figure S13. Fitting of aqueous LiCl at a concentration of 4.62 M. The envelope of the fit is determined by fitting through points at the top of each of the marked peaks. A Savgol filter was applied to smooth the data to assist peak finding, particularly at higher values of r . The vertical lines indicate the extrema that fitting was carried out over.

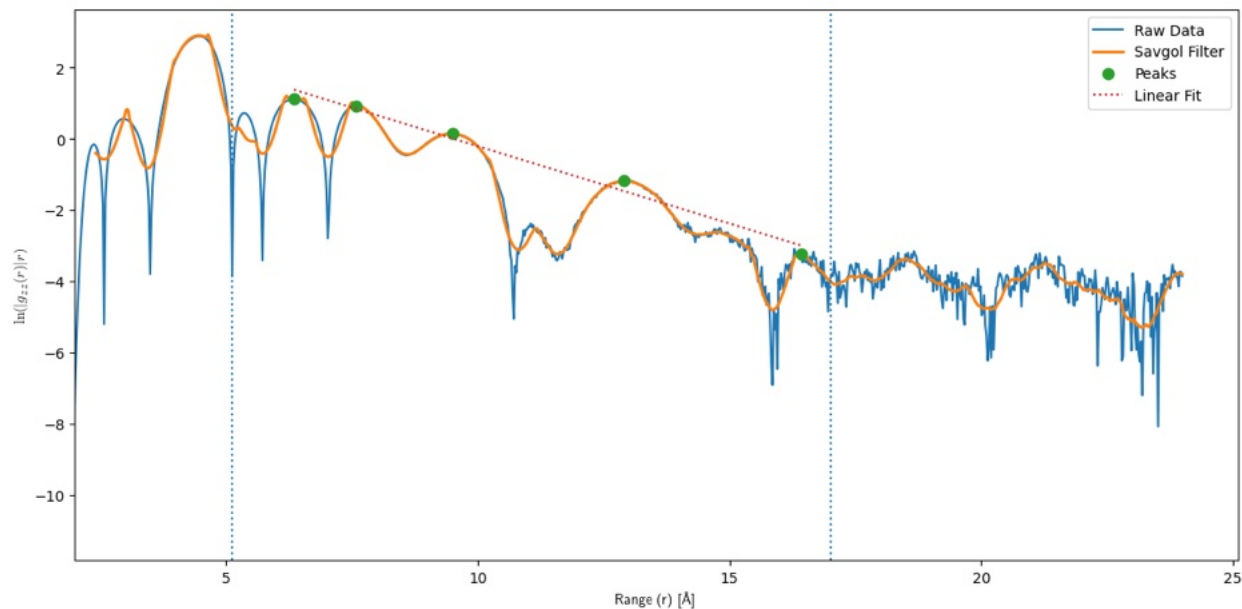


Figure S14. Fitting of aqueous LiCl at a concentration of 5.45 M. The envelope of the fit is determined by fitting through points at the top of each of the marked peaks. A Savgol filter was applied to smooth the data to assist peak finding, particularly at higher values of r . The vertical lines indicate the extrema that fitting was carried out over.

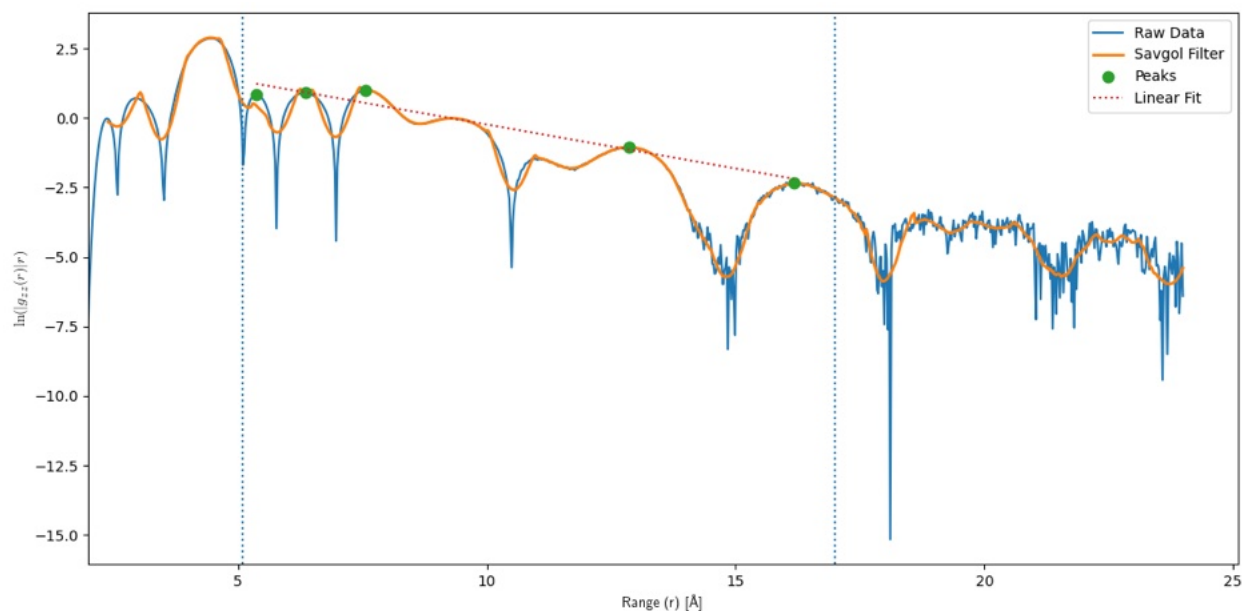


Figure S15. Fitting of aqueous LiCl at a concentration of 6.25 M. The envelope of the fit is determined by fitting through points at the top of each of the marked peaks. A Savgol filter was applied to smooth the data to assist peak finding, particularly at higher values of r . The vertical lines indicate the extrema that fitting was carried out over.

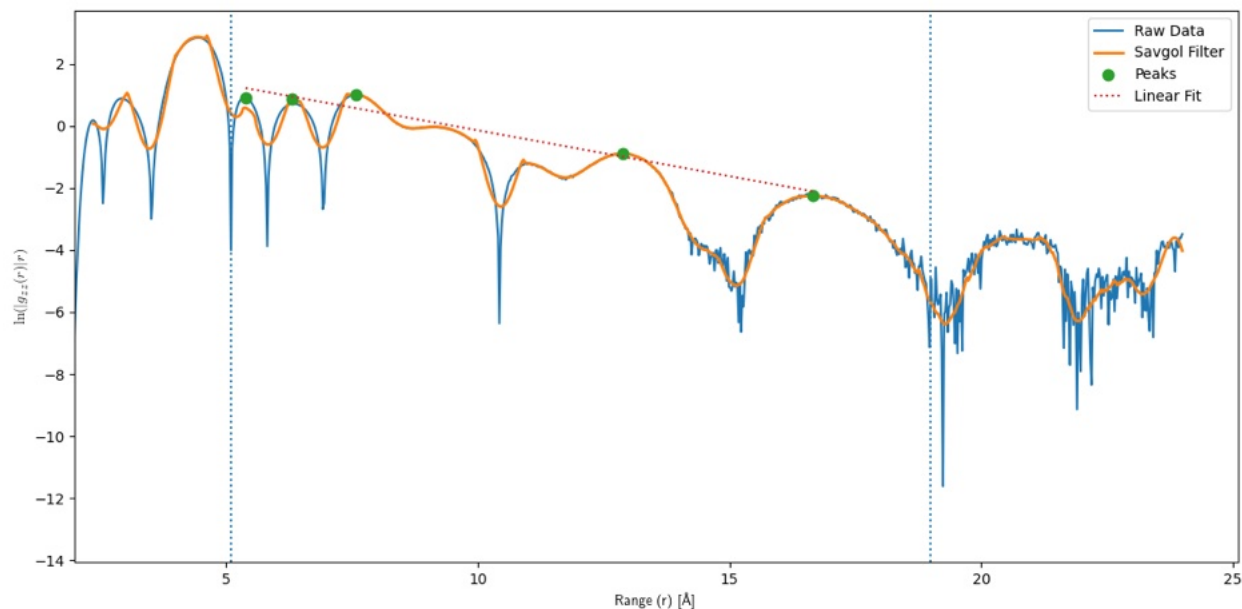


Figure S16. Fitting of aqueous LiCl at a concentration of 7.02 M. The envelope of the fit is determined by fitting through points at the top of each of the marked peaks. A Savgol filter was applied to smooth the data to assist peak finding, particularly at higher values of r . The vertical lines indicate the extrema that fitting was carried out over.

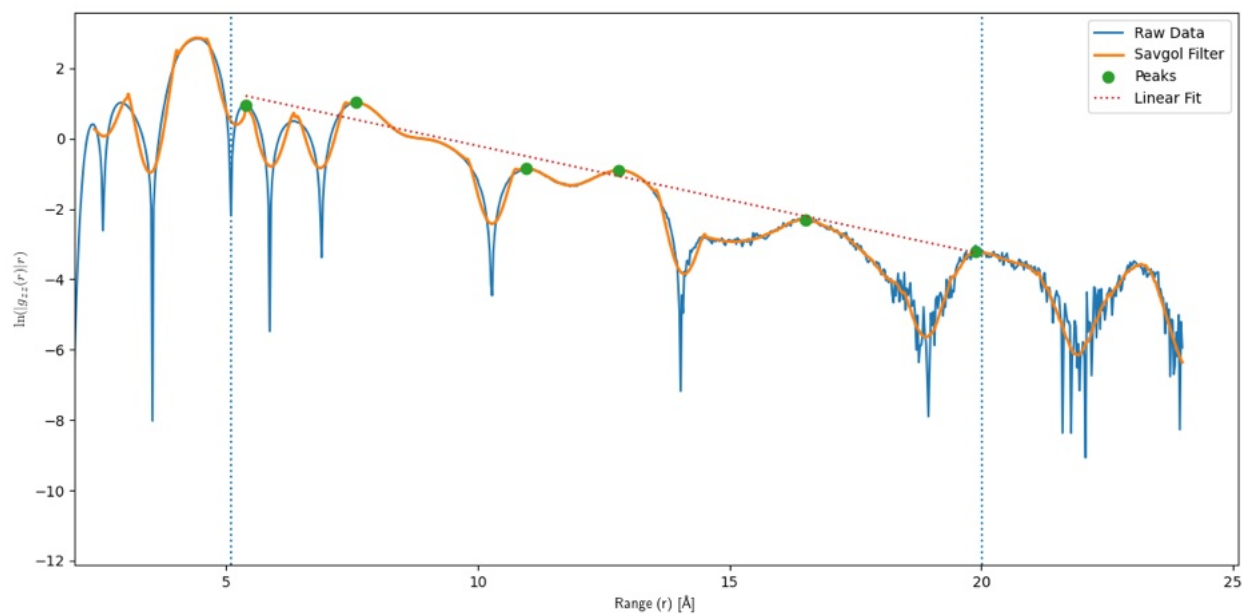


Figure S17. Fitting of aqueous LiCl at a concentration of 7.77 M. The envelope of the fit is determined by fitting through points at the top of each of the marked peaks. A Savgol filter was applied to smooth the data to assist peak finding, particularly at higher values of r . The vertical lines indicate the extrema that fitting was carried out over.

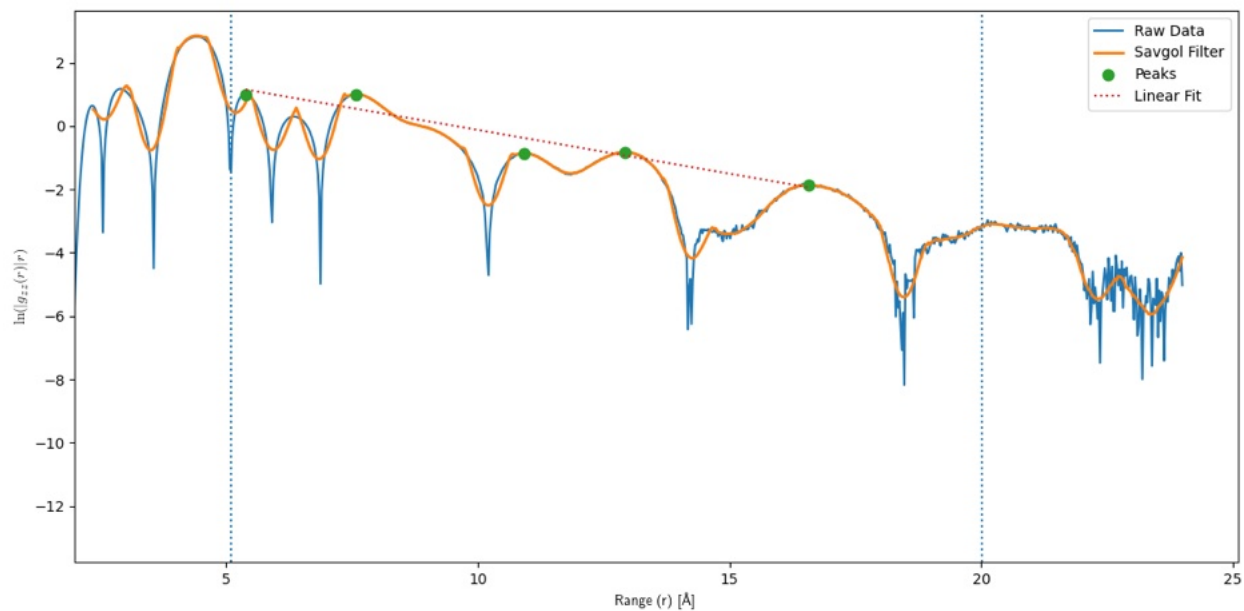


Figure S18. Fitting of aqueous LiCl at a concentration of 8.49 M. The envelope of the fit is determined by fitting through points at the top of each of the marked peaks. A Savgol filter was applied to smooth the data to assist peak finding, particularly at higher values of r . The vertical lines indicate the extrema that fitting was carried out over.

Sodium Chloride

Table S4. Concentrations and conventionally-derived λ_S values for aqueous NaCl simulations (see Figures S19-S31).

Conc (m)	Conc (M)	Decay Length (Å)
0.1	0.11	10.17 ± 0.24
0.5	0.50	3.07 ± 0.15
0.75	0.74	2.43 ± 0.05
1.0	0.99	2.07 ± 0.05
1.25	1.23	1.87 ± 0.08
1.5	1.48	1.95 ± 0.24
2.0	1.95	1.95 ± 0.15
2.5	2.42	2.12 ± 0.25
3.0	2.87	2.08 ± 0.10
3.5	3.32	2.24 ± 0.14
4.0	3.75	2.28 ± 0.19
5.0	4.60	2.56 ± 0.28
6.0	5.41	3.08 ± 0.49

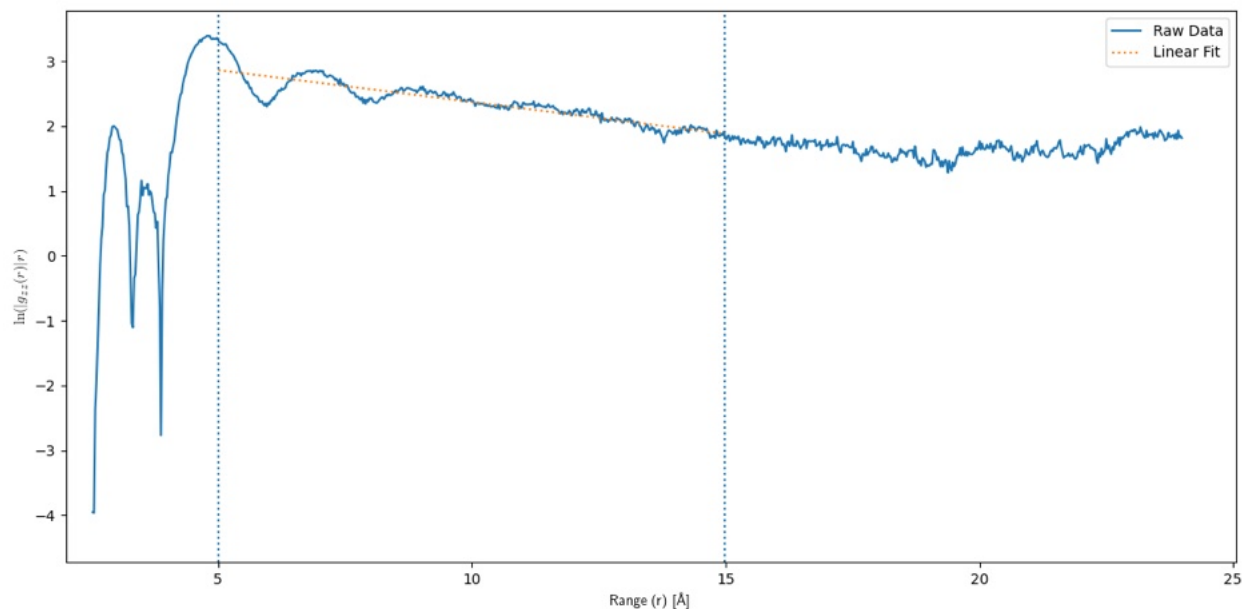


Figure S19. Fitting of aqueous NaCl at a concentration of 0.11 M. In this instance, because of the presence of a plateau in the data, a single straight line was used to fit to the points, rather than fitting the peaks. The vertical lines indicate the extrema that fitting was carried out over.

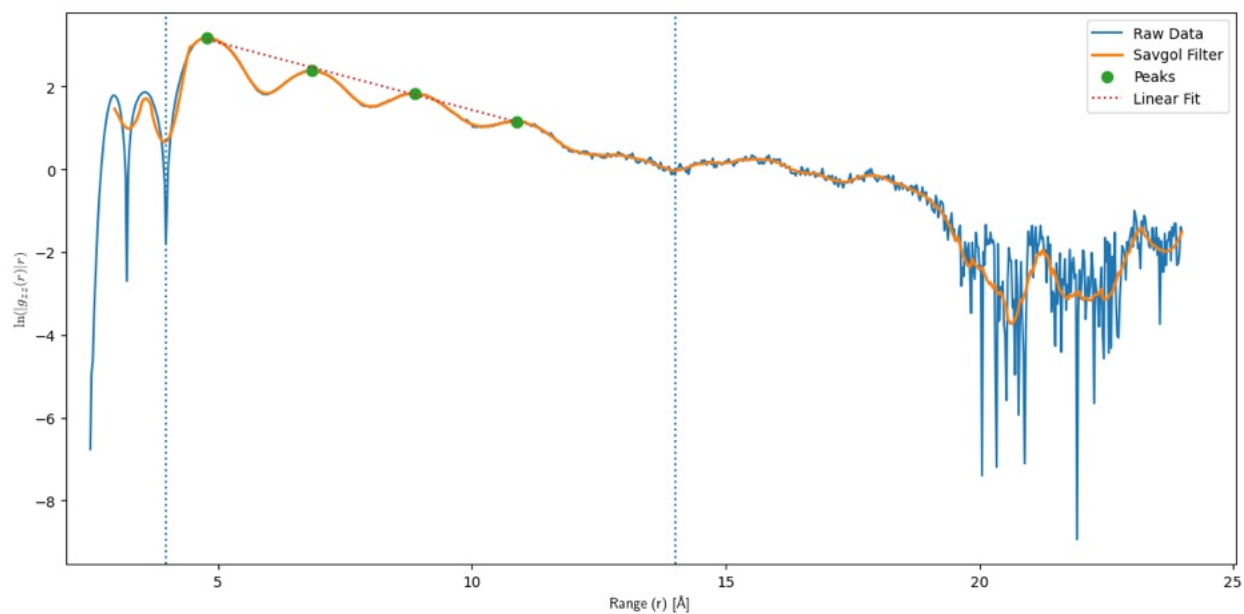


Figure S20. Fitting of aqueous NaCl at a concentration of 0.50 M. The envelope of the fit is determined by fitting through points at the top of each of the marked peaks. A Savgol filter was applied to smooth the data to assist peak finding, particularly at higher values of r . The vertical lines indicate the extrema that fitting was carried out over.

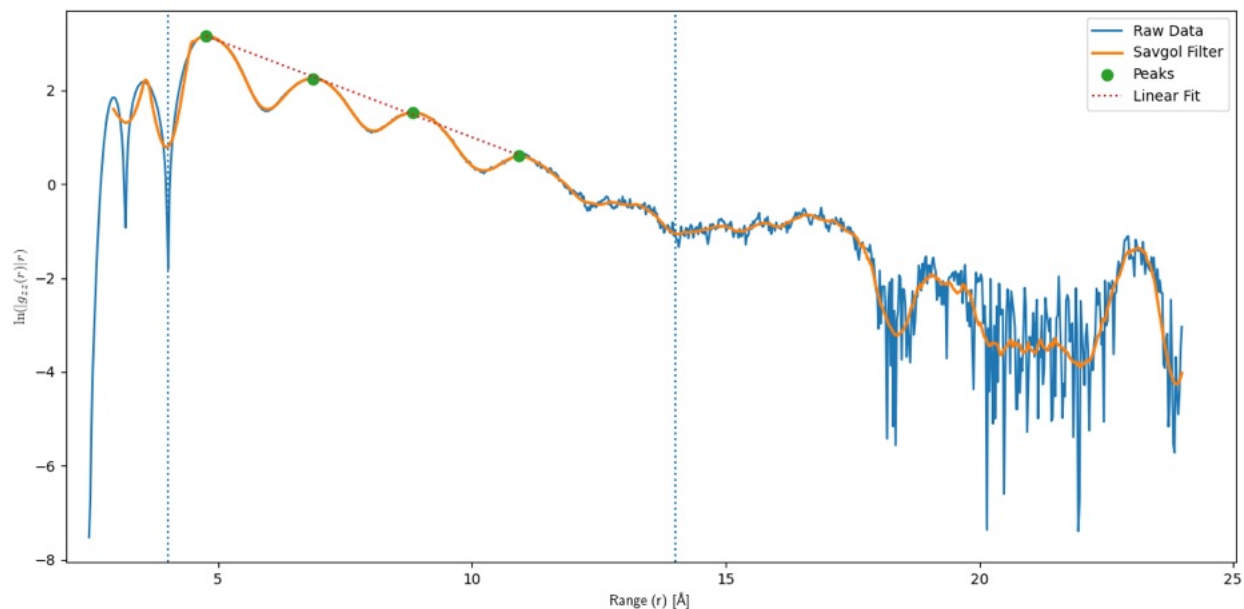


Figure S21. Fitting of aqueous NaCl at a concentration of 0.74 M. The envelope of the fit is determined by fitting through points at the top of each of the marked peaks. A Savgol filter was applied to smooth the data to assist peak finding, particularly at higher values of r . The vertical lines indicate the extrema that fitting was carried out over.

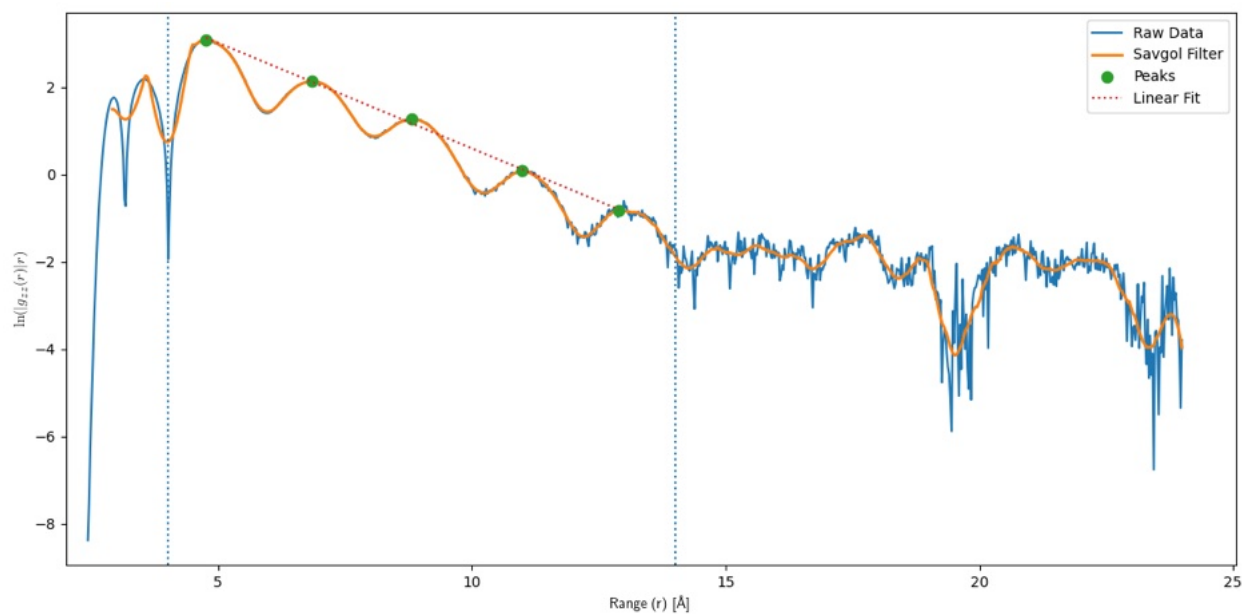


Figure S22. Fitting of aqueous NaCl at a concentration of 0.99 M. The envelope of the fit is determined by fitting through points at the top of each of the marked peaks. A Savgol filter was applied to smooth the data to assist peak finding, particularly at higher values of r . The vertical lines indicate the extrema that fitting was carried out over.

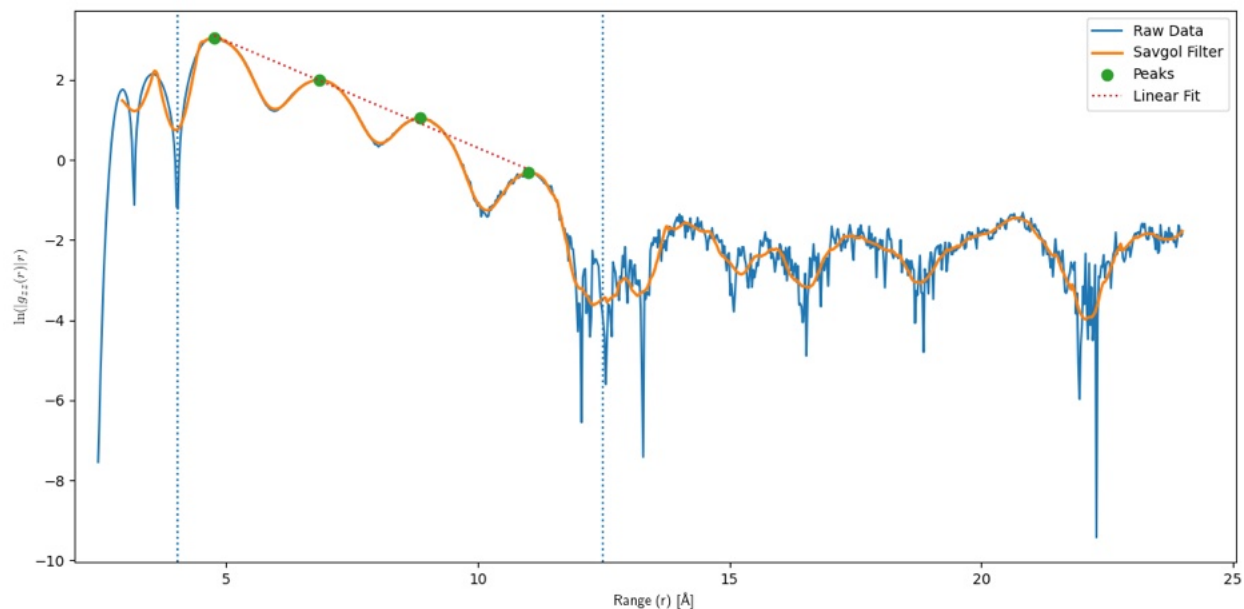


Figure S23. Fitting of aqueous NaCl at a concentration of 1.23 M. The envelope of the fit is determined by fitting through points at the top of each of the marked peaks. A Savgol filter was applied to smooth the data to assist peak finding, particularly at higher values of r . The vertical lines indicate the extrema that fitting was carried out over.

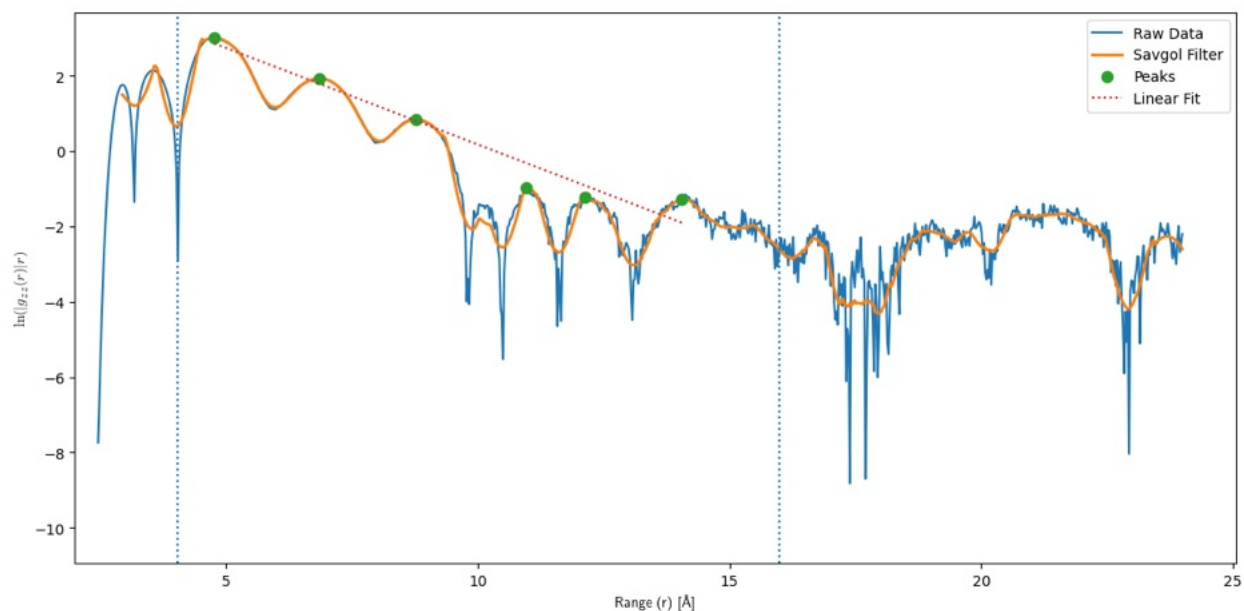


Figure S24. Fitting of aqueous NaCl at a concentration of 1.48 M. The envelope of the fit is determined by fitting through points at the top of each of the marked peaks. A Savgol filter was applied to smooth the data to assist peak finding, particularly at higher values of r . The vertical lines indicate the extrema that fitting was carried out over.

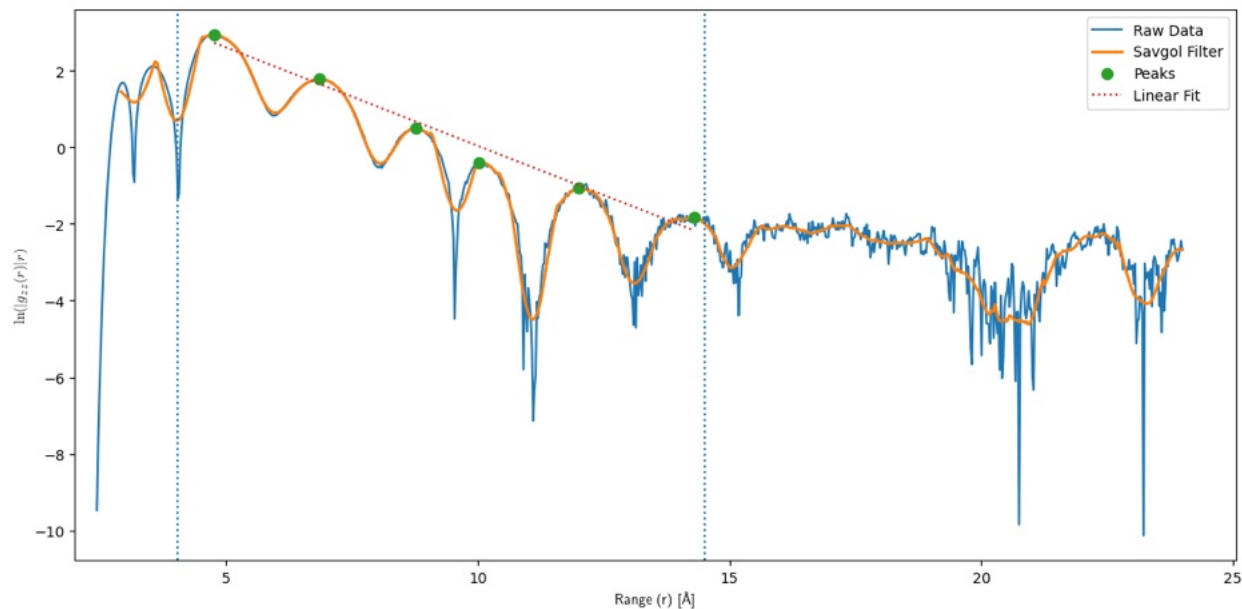


Figure S25. Fitting of aqueous NaCl at a concentration of 1.95 M. The envelope of the fit is determined by fitting through points at the top of each of the marked peaks. A Savgol filter was applied to smooth the data to assist peak finding, particularly at higher values of r . The vertical lines indicate the extrema that fitting was carried out over.

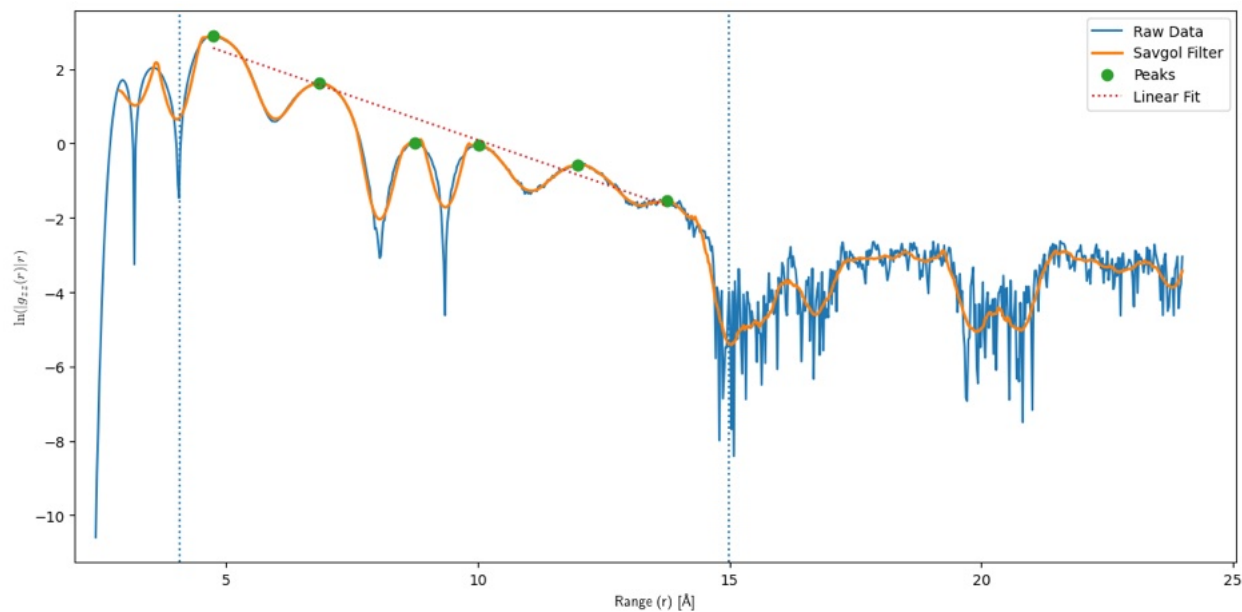


Figure S26. Fitting of aqueous NaCl at a concentration of 2.42 M. The envelope of the fit is determined by fitting through points at the top of each of the marked peaks. A Savgol filter was applied to smooth the data to assist peak finding, particularly at higher values of r . The vertical lines indicate the extrema that fitting was carried out over.

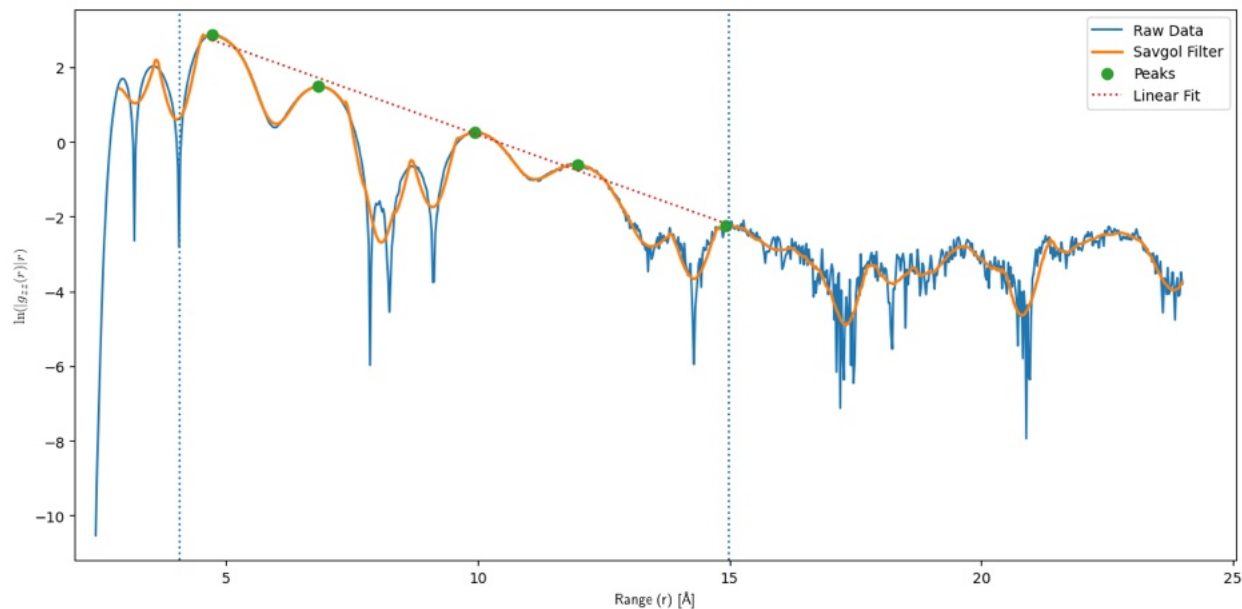


Figure S27. Fitting of aqueous NaCl at a concentration of 2.87 M. The envelope of the fit is determined by fitting through points at the top of each of the marked peaks. A Savgol filter was applied to smooth the data to assist peak finding, particularly at higher values of r . The vertical lines indicate the extrema that fitting was carried out over.

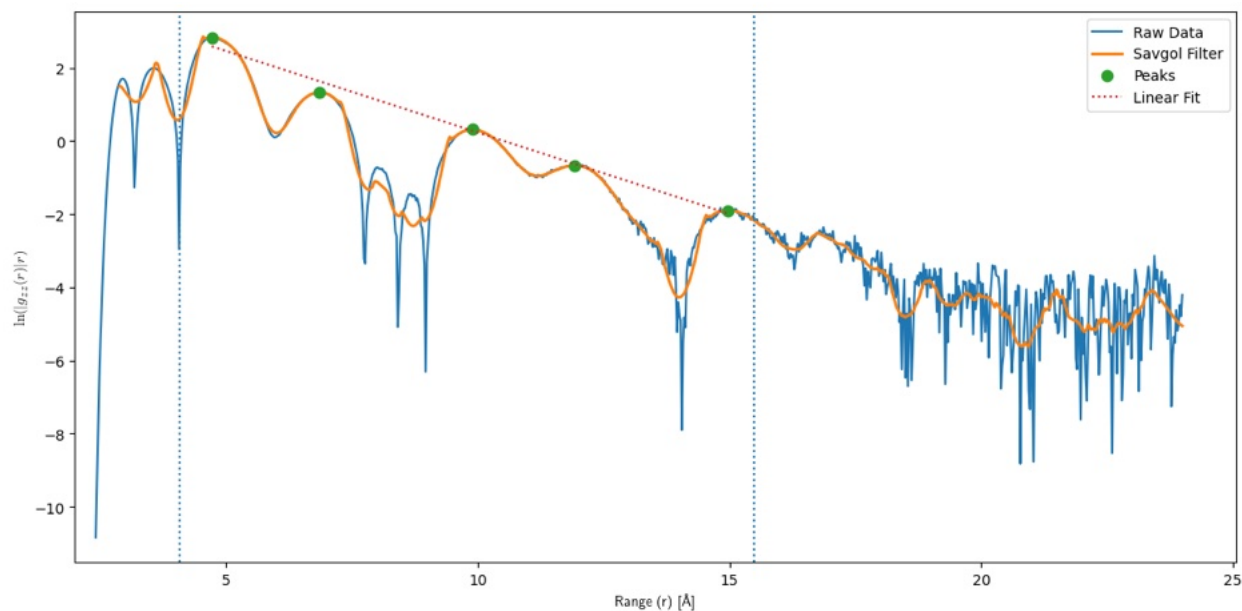


Figure S28. Fitting of aqueous NaCl at a concentration of 3.32 M. The envelope of the fit is determined by fitting through points at the top of each of the marked peaks. A Savgol filter was applied to smooth the data to assist peak finding, particularly at higher values of r . The vertical lines indicate the extrema that fitting was carried out over.

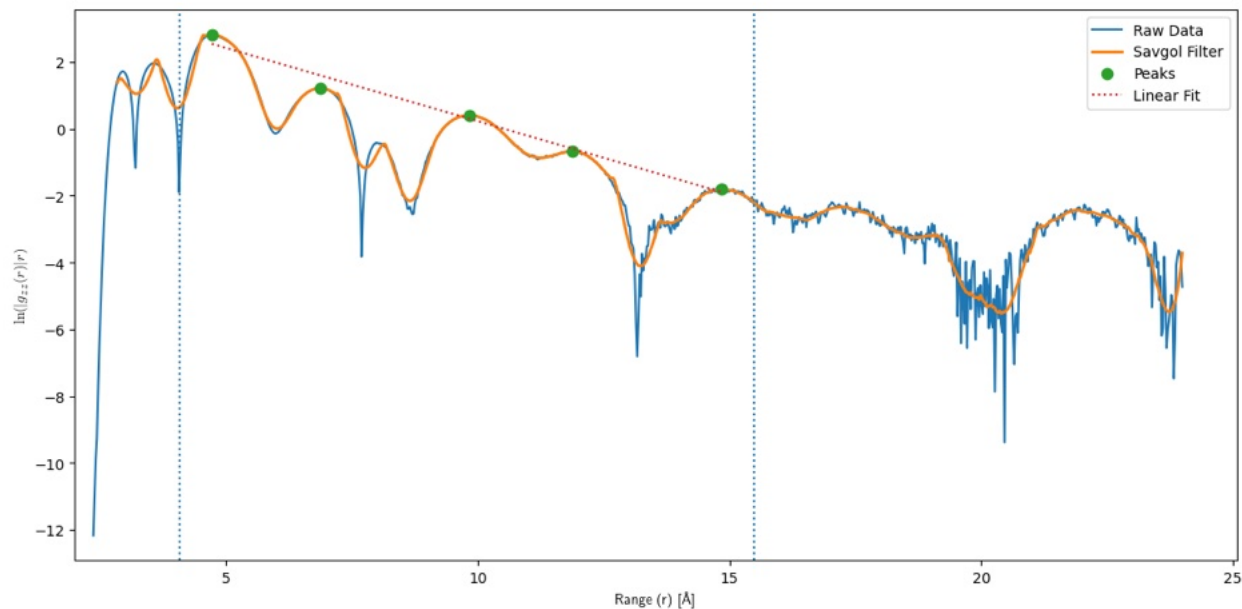


Figure S29. Fitting of aqueous NaCl at a concentration of 3.75 M. The envelope of the fit is determined by fitting through points at the top of each of the marked peaks. A Savgol filter was applied to smooth the data to assist peak finding, particularly at higher values of r . The vertical lines indicate the extrema that fitting was carried out over.

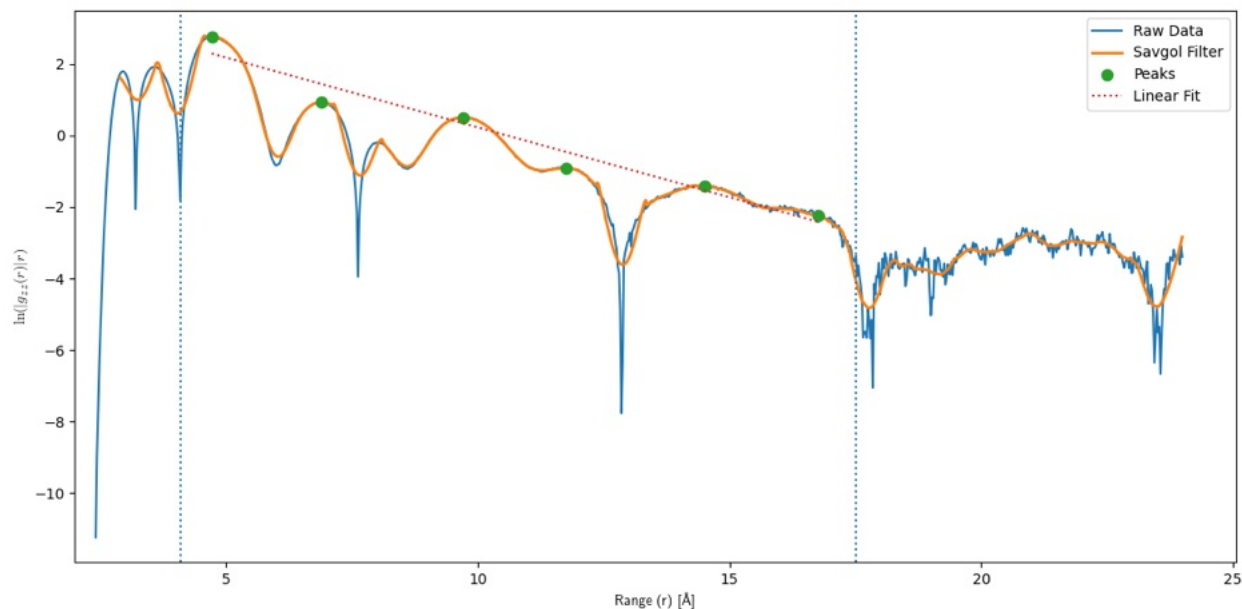


Figure S30. Fitting of aqueous NaCl at a concentration of 4.60 M. The envelope of the fit is determined by fitting through points at the top of each of the marked peaks. A Savgol filter was applied to smooth the data to assist peak finding, particularly at higher values of r . The vertical lines indicate the extrema that fitting was carried out over.

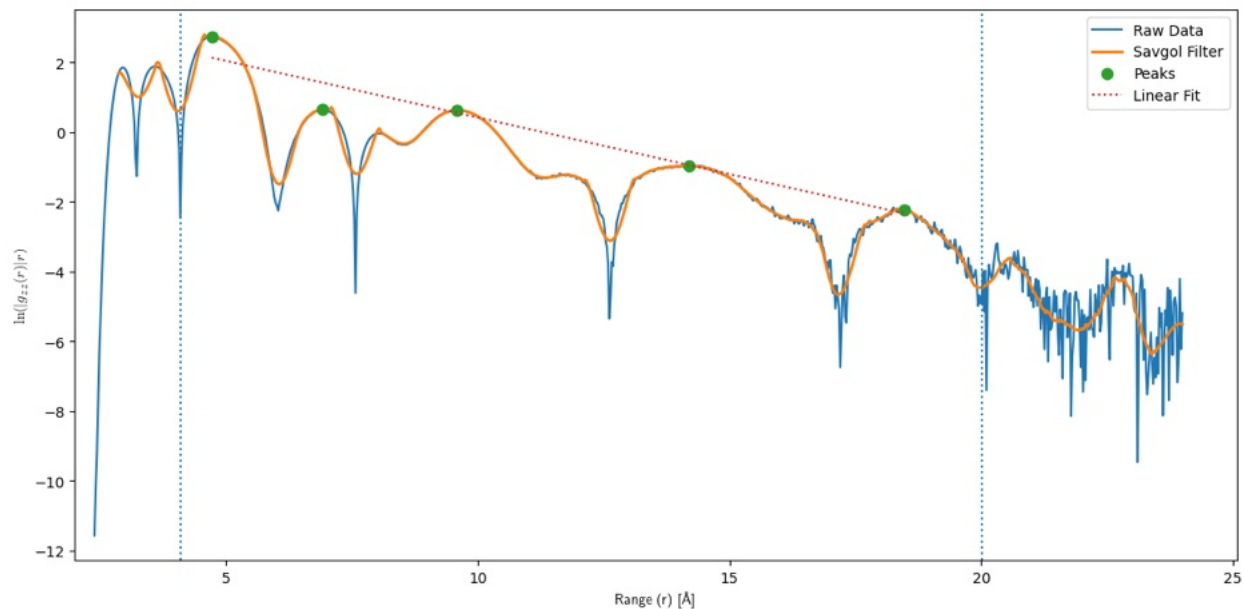


Figure S31. Fitting of aqueous NaCl at a concentration of 5.41 M. The envelope of the fit is determined by fitting through points at the top of each of the marked peaks. A Savgol filter was applied to smooth the data to assist peak finding, particularly at higher values of r . The vertical lines indicate the extrema that fitting was carried out over.

Potassium Chloride

Table S5. Concentrations and conventionally-derived λ_S values for aqueous KCl simulations (see Figures S32-S40).

Conc (m)	Conc (M)	Decay Length (Å)
0.1	0.11	8.60 ± 0.13
0.5	0.50	3.76 ± 0.33
0.75	0.73	2.70 ± 0.08
1.0	0.98	2.35 ± 0.04
1.25	1.22	2.45 ± 0.05
1.5	1.45	2.02 ± 0.16
2.0	1.90	1.79 ± 0.06
3.0	2.78	1.76 ± 0.09
4.0	3.60	2.15 ± 0.07

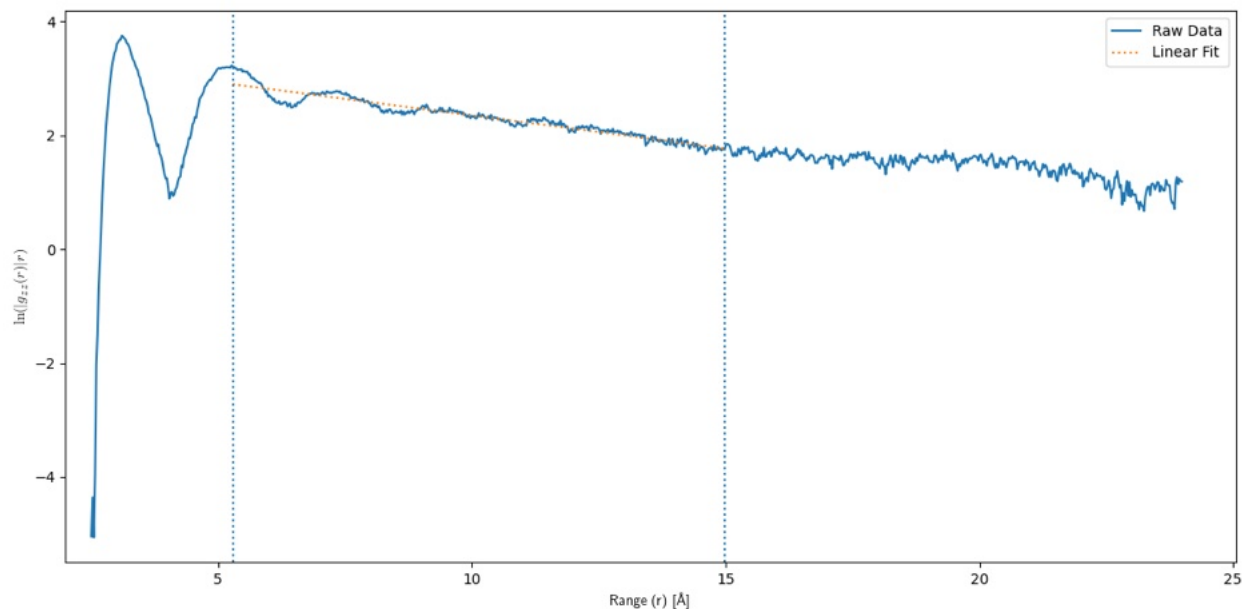


Figure S32. Fitting of aqueous KCl at a concentration of 0.11 M. In this instance, because of the presence of a plateau in the data, a single straight line was used to fit to the points, rather than fitting the peaks. The vertical lines indicate the extrema that fitting was carried out over.

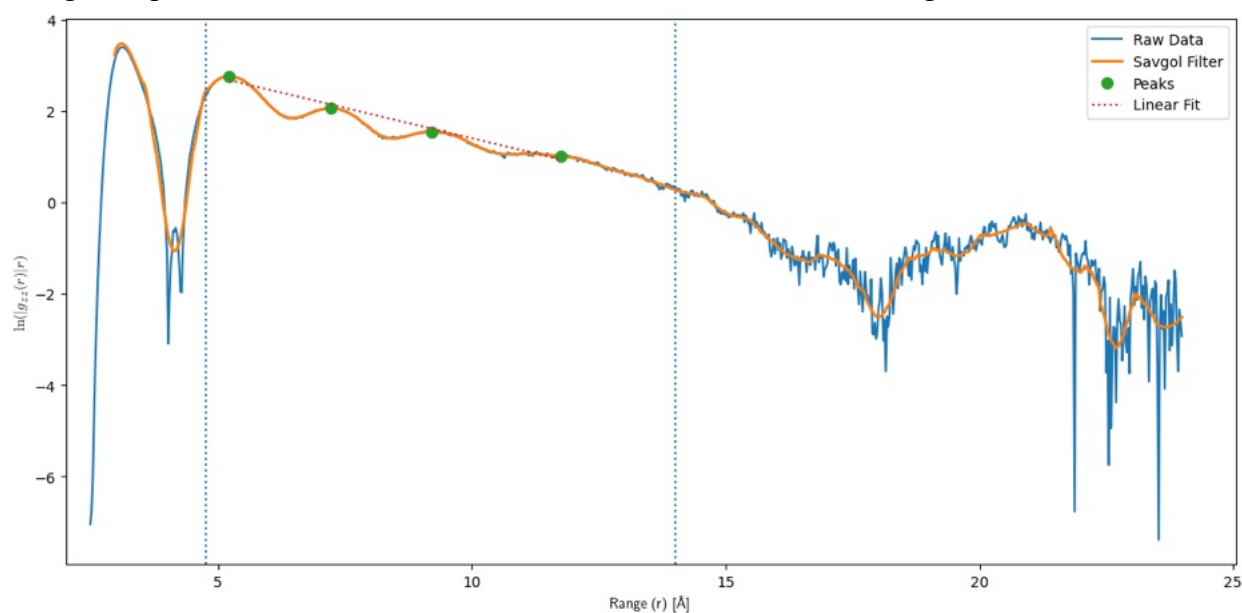


Figure S33. Fitting of aqueous KCl at a concentration of 0.50 M. The envelope of the fit is determined by fitting through points at the top of each of the marked peaks. A Savgol filter was applied to smooth the data to assist peak finding, particularly at higher values of r . The vertical lines indicate the extrema that fitting was carried out over.

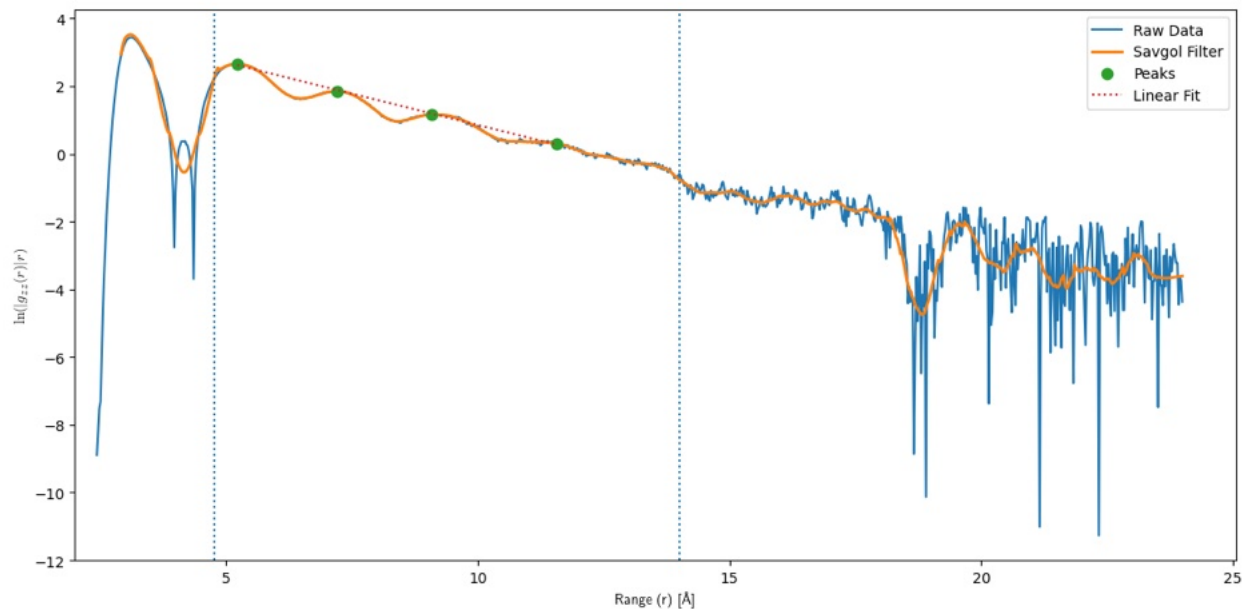


Figure S34. Fitting of aqueous KCl at a concentration of 0.73 M. The envelope of the fit is determined by fitting through points at the top of each of the marked peaks. A Savgol filter was applied to smooth the data to assist peak finding, particularly at higher values of r . The vertical lines indicate the extrema that fitting was carried out over.

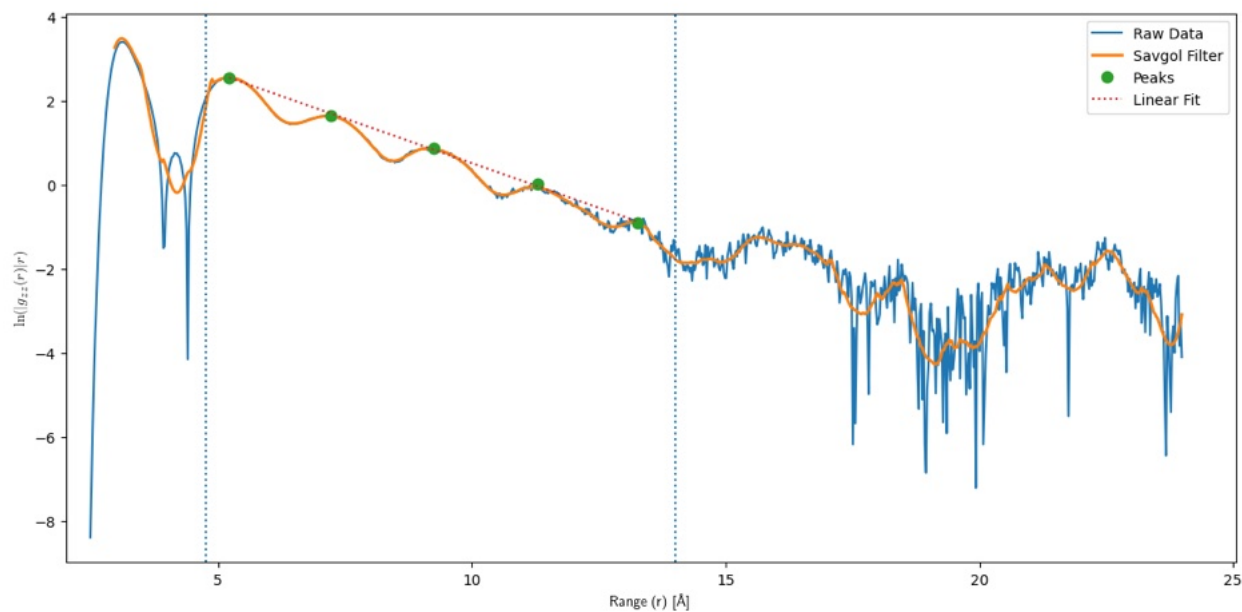


Figure S35. Fitting of aqueous KCl at a concentration of 0.98 M. The envelope of the fit is determined by fitting through points at the top of each of the marked peaks. A Savgol filter was applied to smooth the data to assist peak finding, particularly at higher values of r . The vertical lines indicate the extrema that fitting was carried out over.

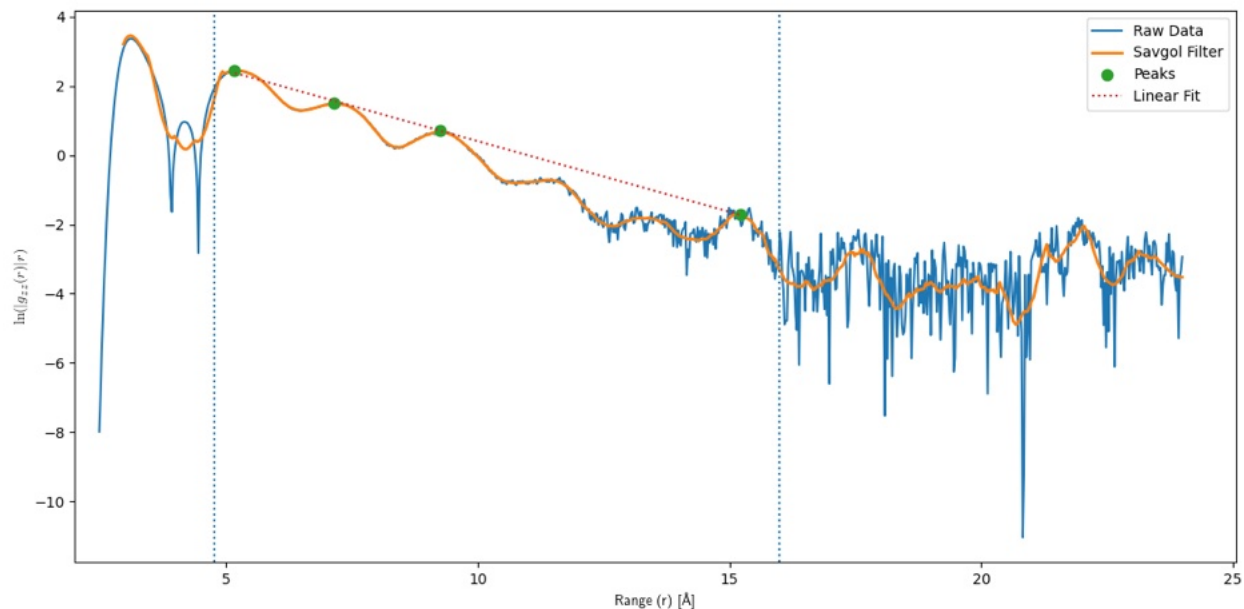


Figure S36. Fitting of aqueous KCl at a concentration of 1.22 M. The envelope of the fit is determined by fitting through points at the top of each of the marked peaks. A Savgol filter was applied to smooth the data to assist peak finding, particularly at higher values of r . The vertical lines indicate the extrema that fitting was carried out over.

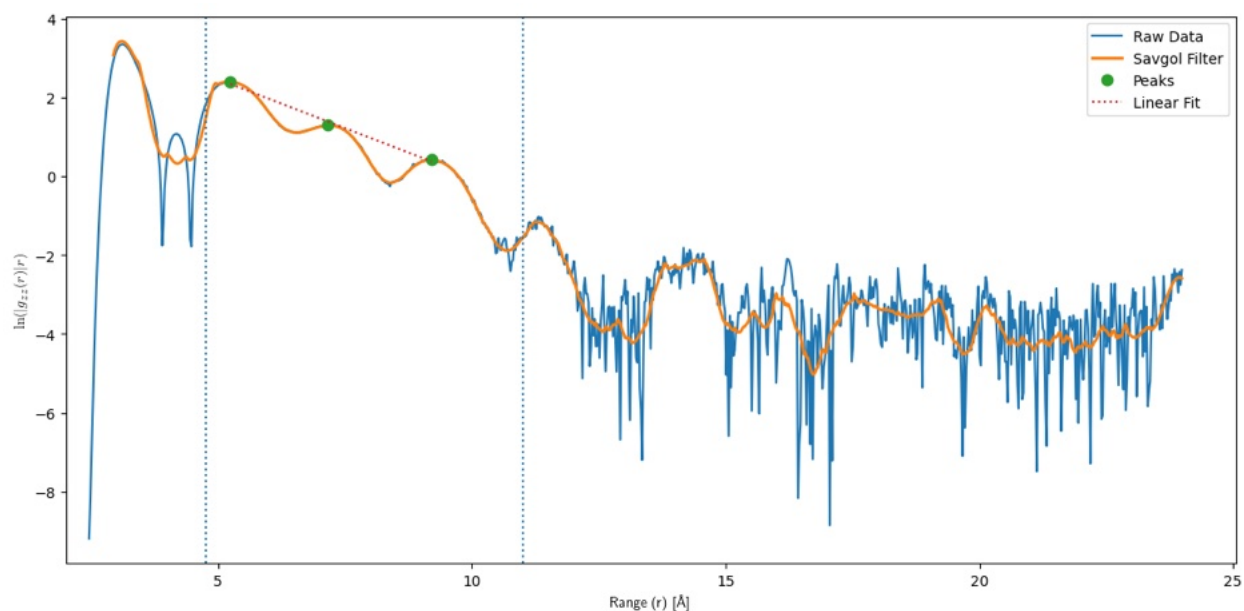


Figure S37. Fitting of aqueous KCl at a concentration of 1.45 M. The envelope of the fit is determined by fitting through points at the top of each of the marked peaks. A Savgol filter was applied to smooth the data to assist peak finding, particularly at higher values of r . The vertical lines indicate the extrema that fitting was carried out over.

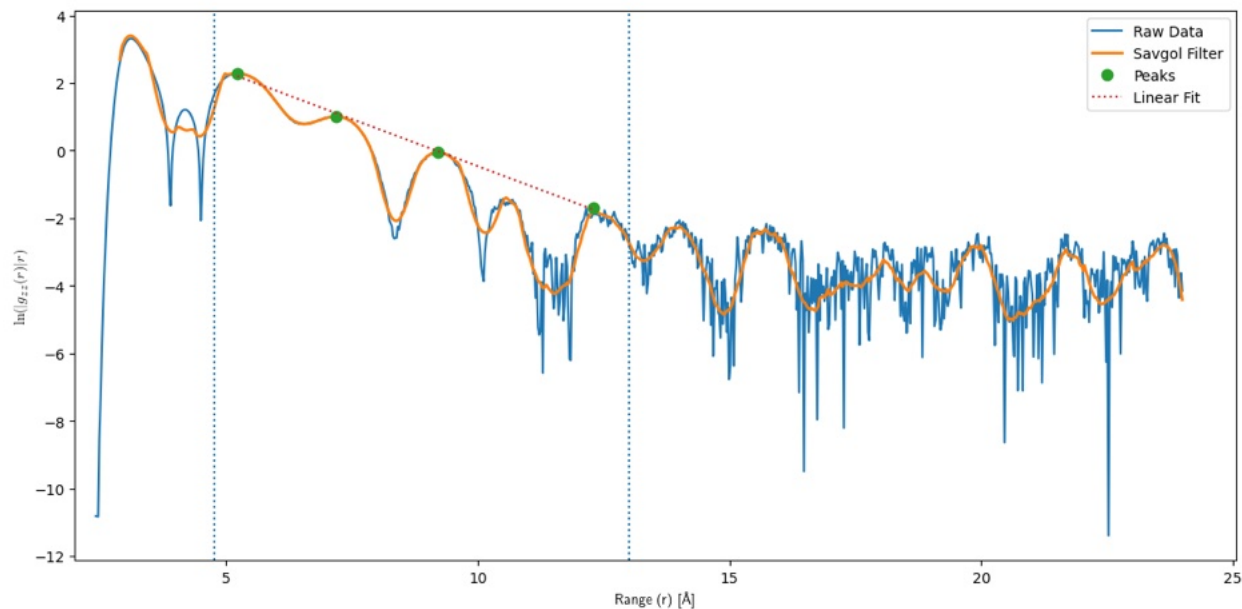


Figure S38. Fitting of aqueous KCl at a concentration of 1.90 M. The envelope of the fit is determined by fitting through points at the top of each of the marked peaks. A Savgol filter was applied to smooth the data to assist peak finding, particularly at higher values of r . The vertical lines indicate the extrema that fitting was carried out over.

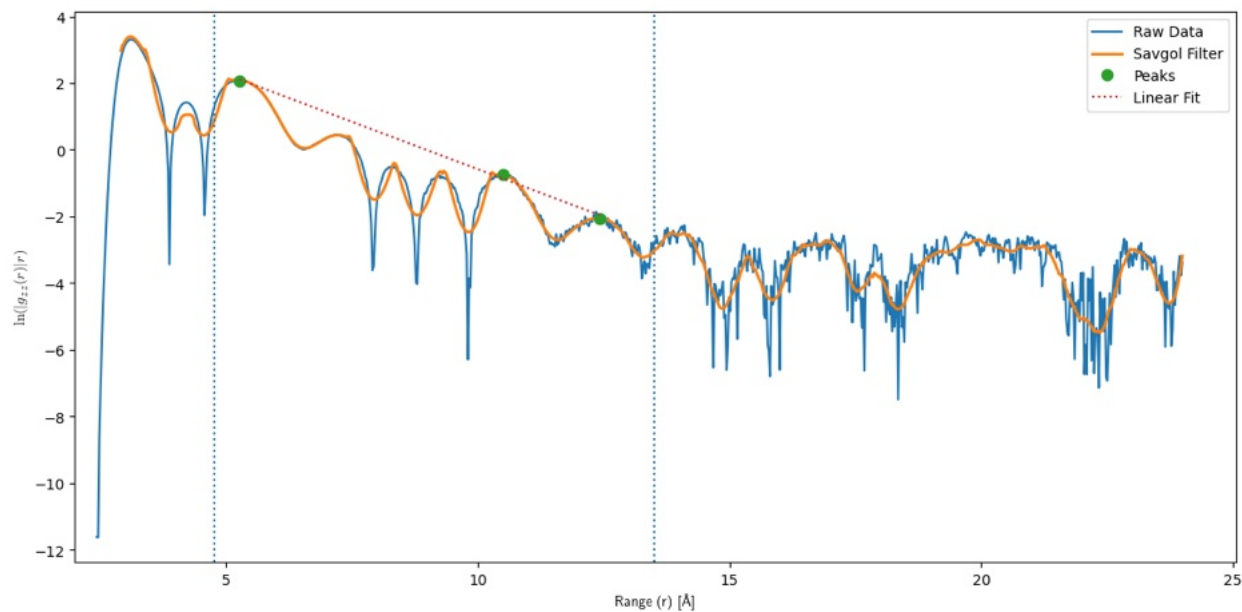


Figure S39. Fitting of aqueous KCl at a concentration of 2.78 M. The envelope of the fit is determined by fitting through points at the top of each of the marked peaks. A Savgol filter was applied to smooth the data to assist peak finding, particularly at higher values of r . The vertical lines indicate the extrema that fitting was carried out over.

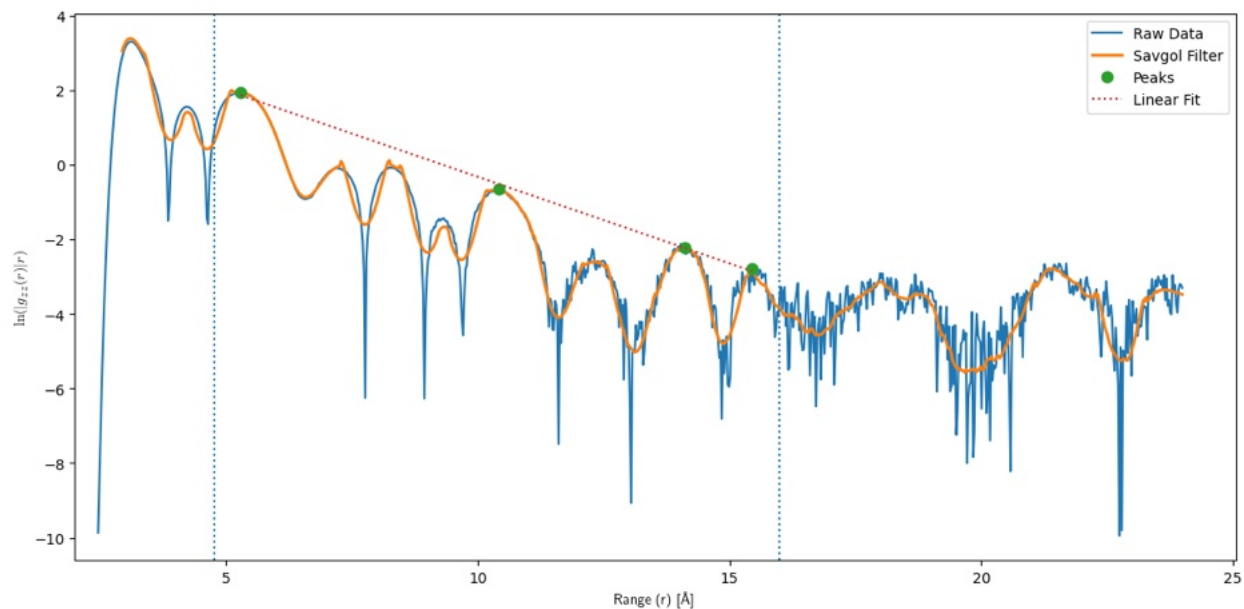


Figure S40. Fitting of aqueous KCl at a concentration of 3.60 M. The envelope of the fit is determined by fitting through points at the top of each of the marked peaks. A Savgol filter was applied to smooth the data to assist peak finding, particularly at higher values of r . The vertical lines indicate the extrema that fitting was carried out over.

Cesium Chloride

Table S6. Concentrations and conventionally-derived λ_S values for aqueous CsCl simulations (see Figures S41-S51).

Conc (m)	Conc (M)	Decay Length (Å)
0.1	0.11	6.02 ± 0.08
0.5	0.50	3.55 ± 0.23
0.75	0.73	3.07 ± 0.42
1.0	0.96	2.04 ± 0.26
1.25	1.20	1.94 ± 0.26
1.5	1.42	1.81 ± 0.17
2.0	1.86	1.38 ± 0.14
3.0	2.68	1.96 ± 0.11
4.0	3.44	1.93 ± 0.11
5.0	4.15	2.01 ± 0.14
10.0	6.96	2.29 ± 0.13

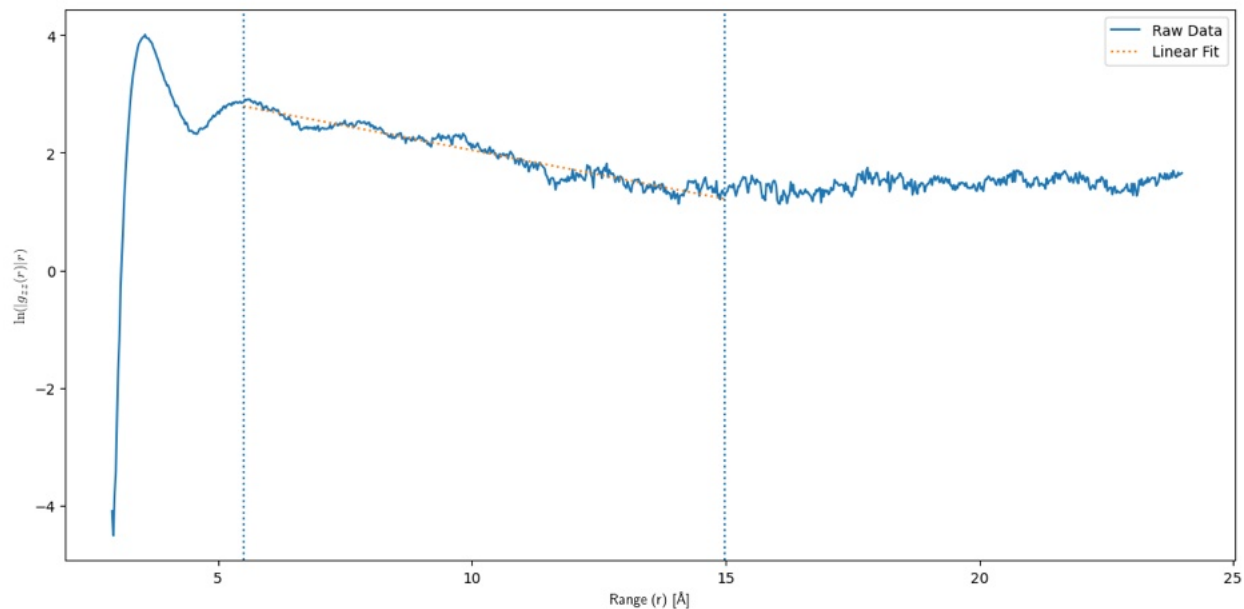


Figure S41. Fitting of aqueous CsCl at a concentration of 0.11 M. In this instance, because of the presence of a plateau in the data, a single straight line was used to fit to the points, rather than fitting the peaks. The vertical lines indicate the extrema that fitting was carried out over.

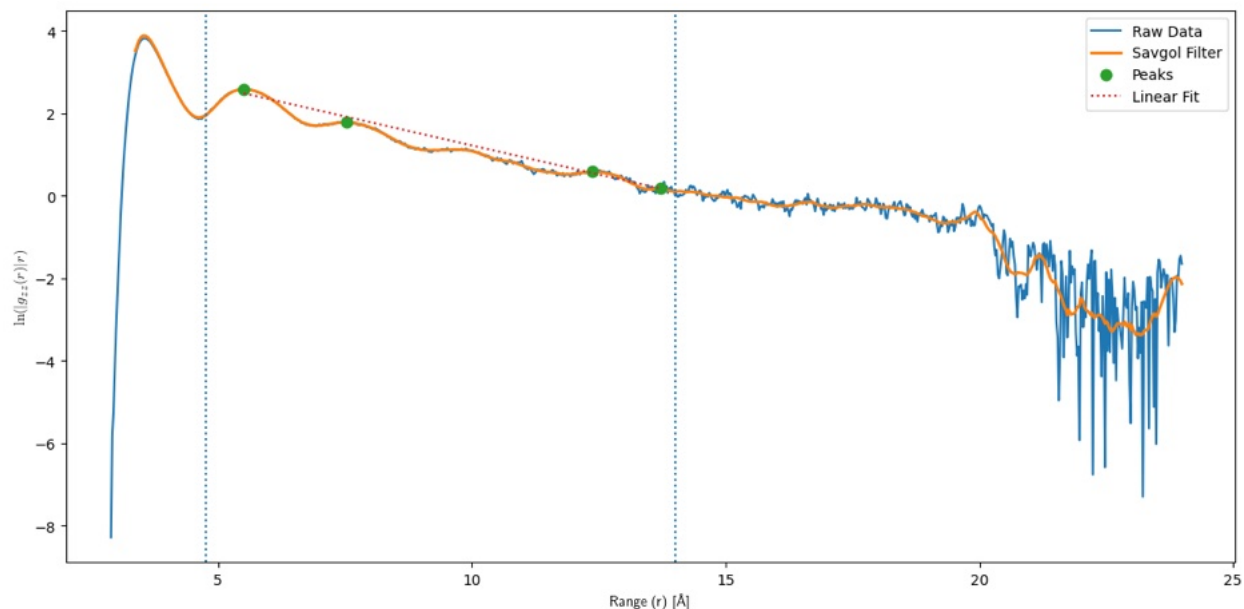


Figure S42. Fitting of aqueous CsCl at a concentration of 0.50 M. The envelope of the fit is determined by fitting through points at the top of each of the marked peaks. A Savgol filter was applied to smooth the data to assist peak finding, particularly at higher values of r . The vertical lines indicate the extrema that fitting was carried out over.

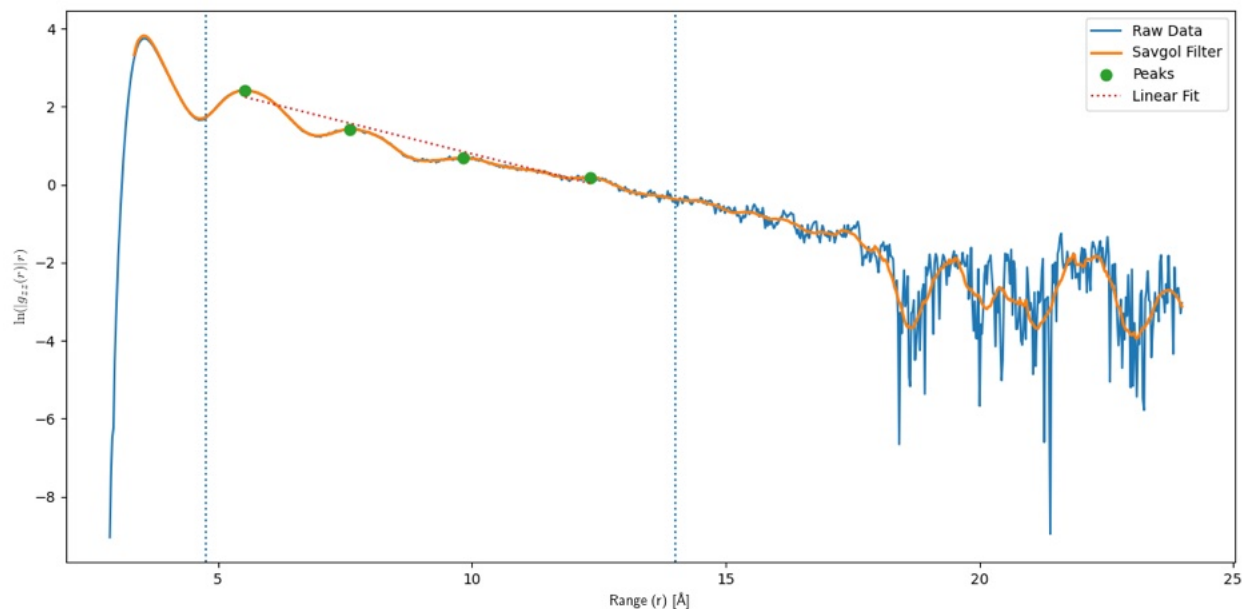


Figure S43. Fitting of aqueous CsCl at a concentration of 0.73 M. The envelope of the fit is determined by fitting through points at the top of each of the marked peaks. A Savgol filter was applied to smooth the data to assist peak finding, particularly at higher values of r . The vertical lines indicate the extrema that fitting was carried out over.

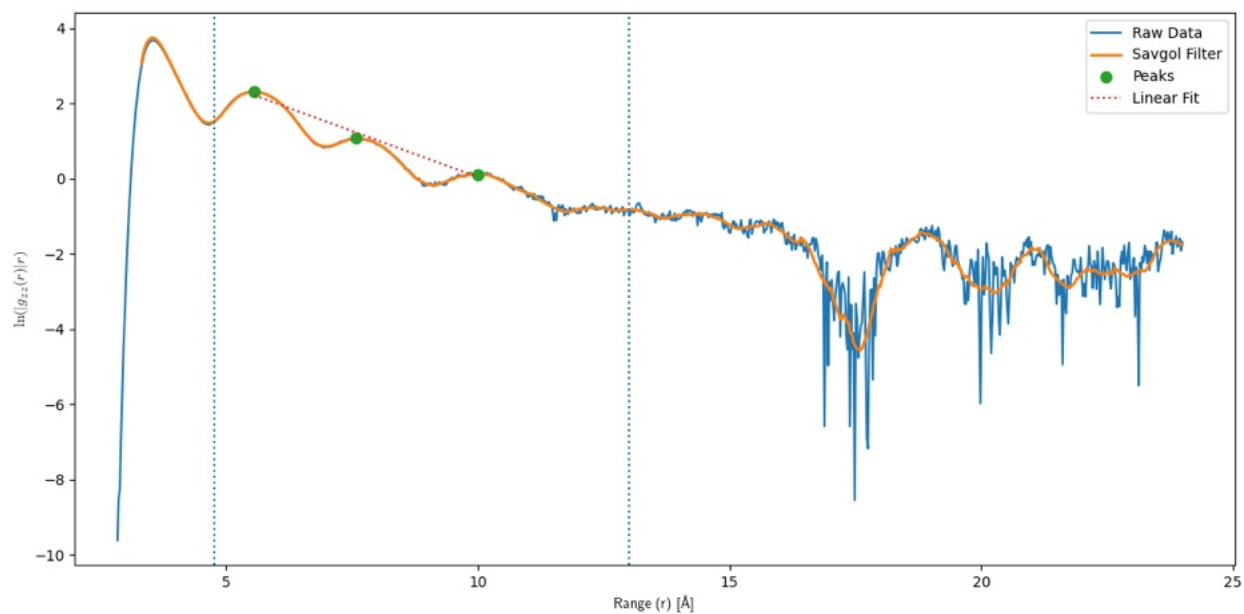


Figure S44. Fitting of aqueous CsCl at a concentration of 0.96 M. The envelope of the fit is determined by fitting through points at the top of each of the marked peaks. A Savgol filter was applied to smooth the data to assist peak finding, particularly at higher values of r . The vertical lines indicate the extrema that fitting was carried out over.

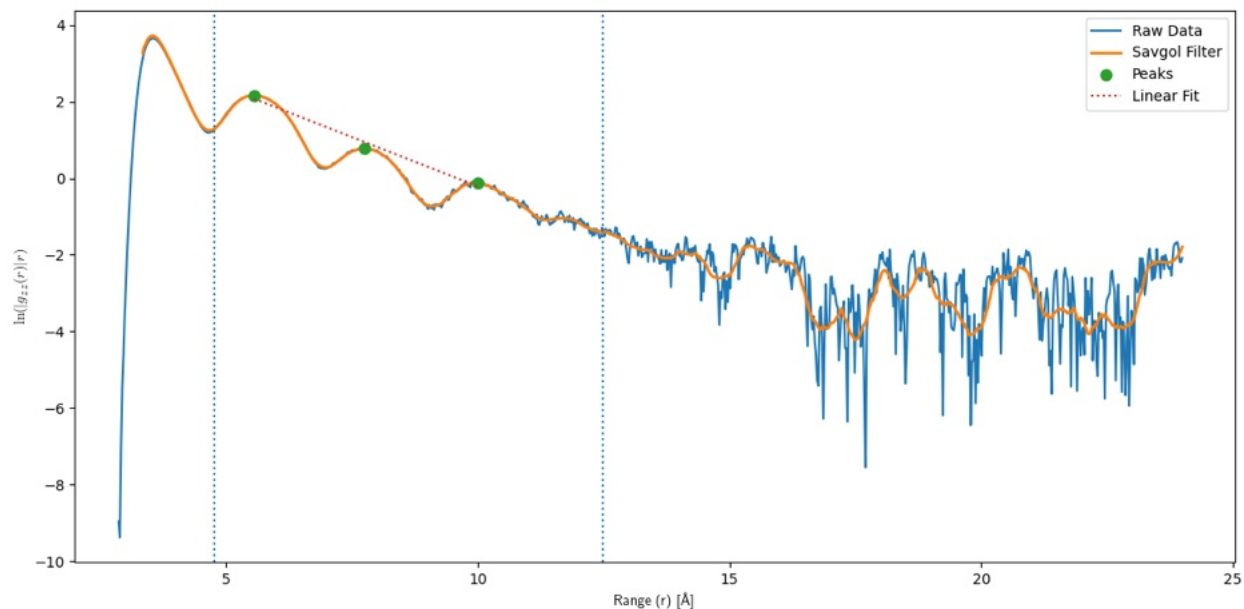


Figure S45. Fitting of aqueous CsCl at a concentration of 1.20 M. The envelope of the fit is determined by fitting through points at the top of each of the marked peaks. A Savgol filter was applied to smooth the data to assist peak finding, particularly at higher values of r . The vertical lines indicate the extrema that fitting was carried out over.

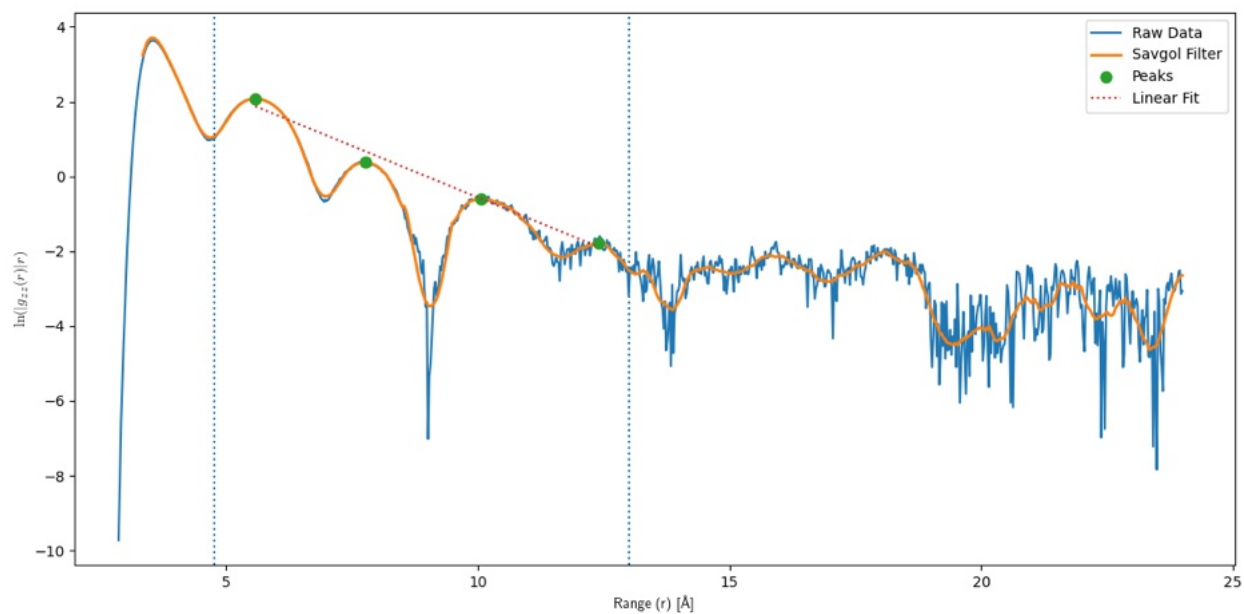


Figure S46. Fitting of aqueous CsCl at a concentration of 1.42 M. The envelope of the fit is determined by fitting through points at the top of each of the marked peaks. A Savgol filter was applied to smooth the data to assist peak finding, particularly at higher values of r . The vertical lines indicate the extrema that fitting was carried out over.

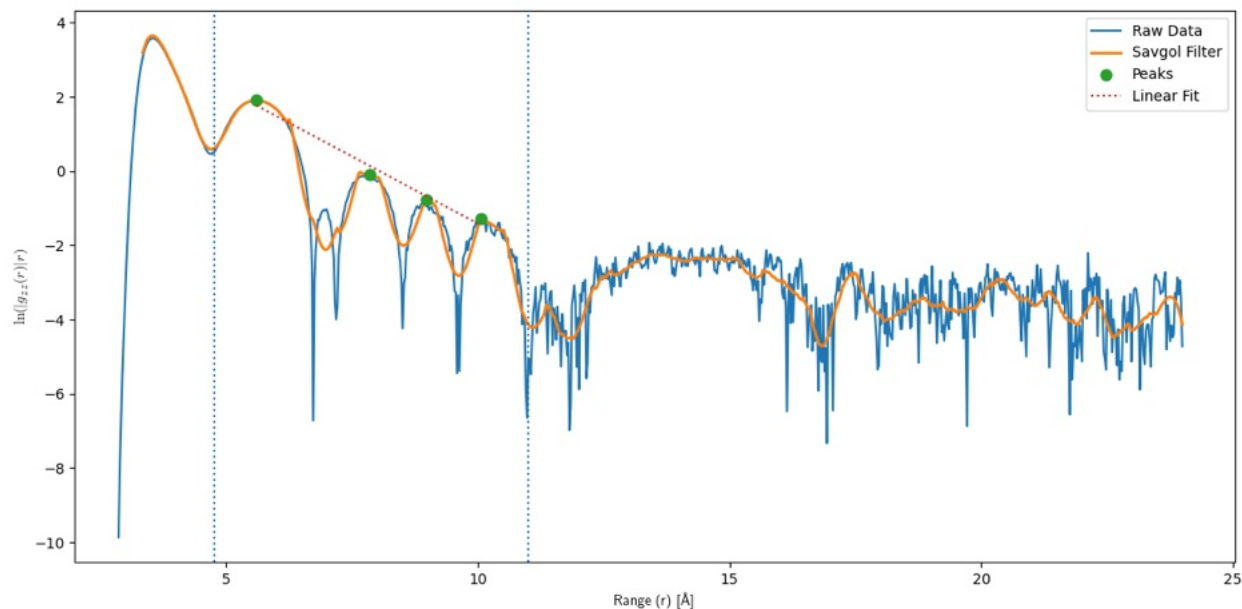


Figure S47. Fitting of aqueous CsCl at a concentration of 1.86 M. The envelope of the fit is determined by fitting through points at the top of each of the marked peaks. A Savgol filter was applied to smooth the data to assist peak finding, particularly at higher values of r . The vertical lines indicate the extrema that fitting was carried out over.

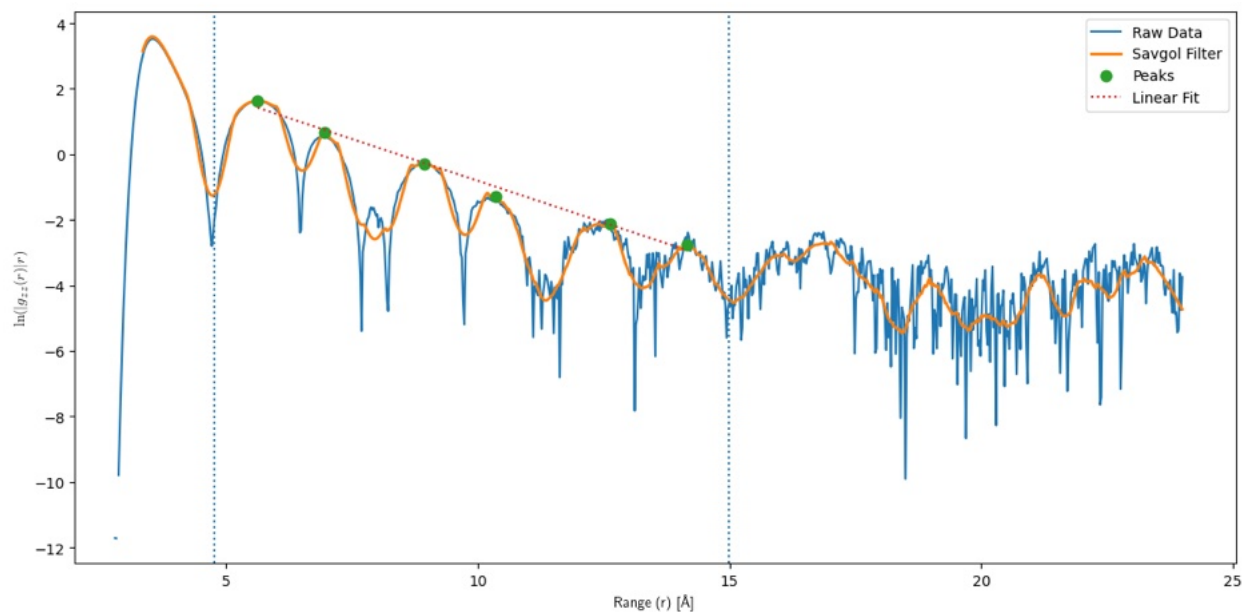


Figure S48. Fitting of aqueous CsCl at a concentration of 2.68 M. The envelope of the fit is determined by fitting through points at the top of each of the marked peaks. A Savgol filter was applied to smooth the data to assist peak finding, particularly at higher values of r . The vertical lines indicate the extrema that fitting was carried out over.

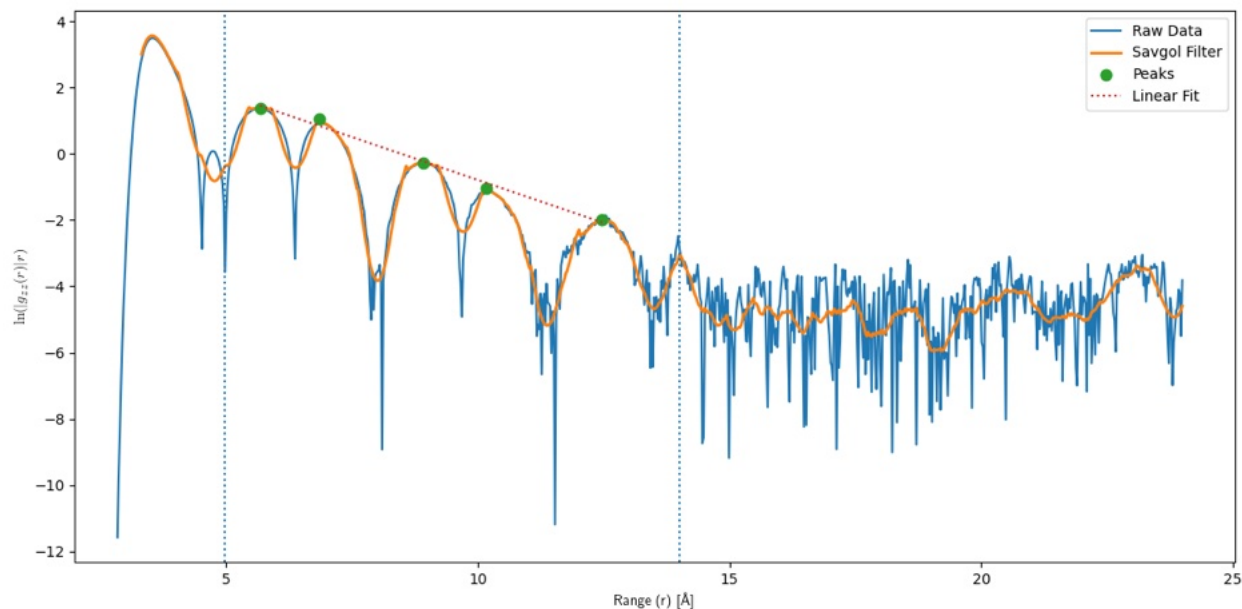


Figure S49. Fitting of aqueous CsCl at a concentration of 3.44 M. The envelope of the fit is determined by fitting through points at the top of each of the marked peaks. A Savgol filter was applied to smooth the data to assist peak finding, particularly at higher values of r . The vertical lines indicate the extrema that fitting was carried out over.

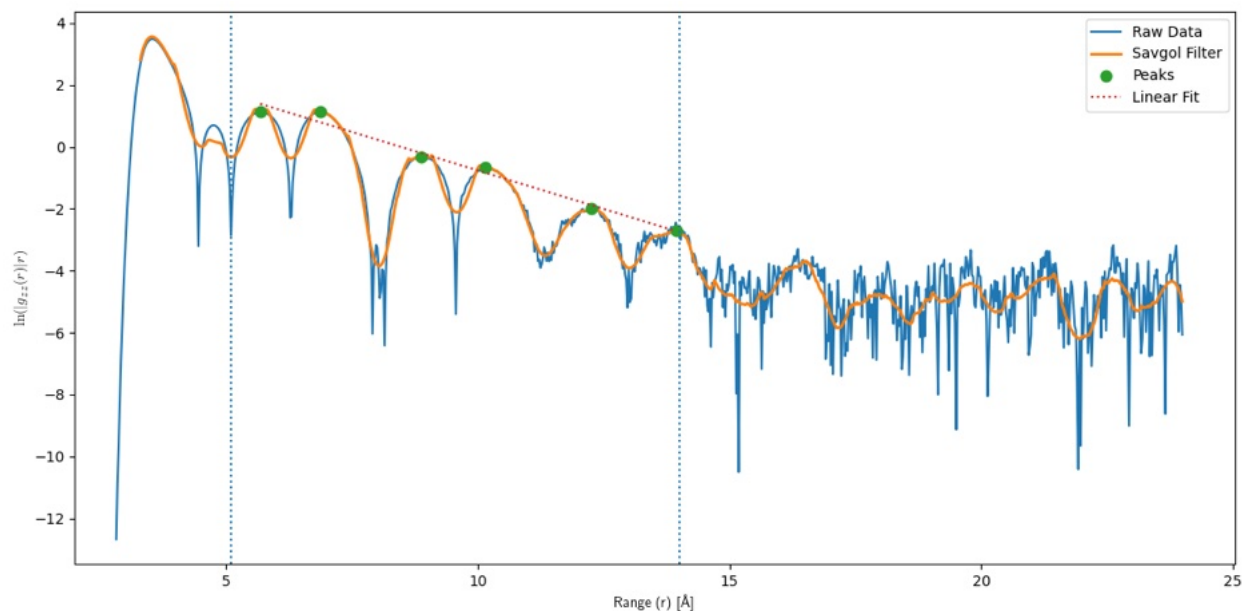


Figure S50. Fitting of aqueous CsCl at a concentration of 4.15 M. The envelope of the fit is determined by fitting through points at the top of each of the marked peaks. A Savgol filter was applied to smooth the data to assist peak finding, particularly at higher values of r . The vertical lines indicate the extrema that fitting was carried out over.

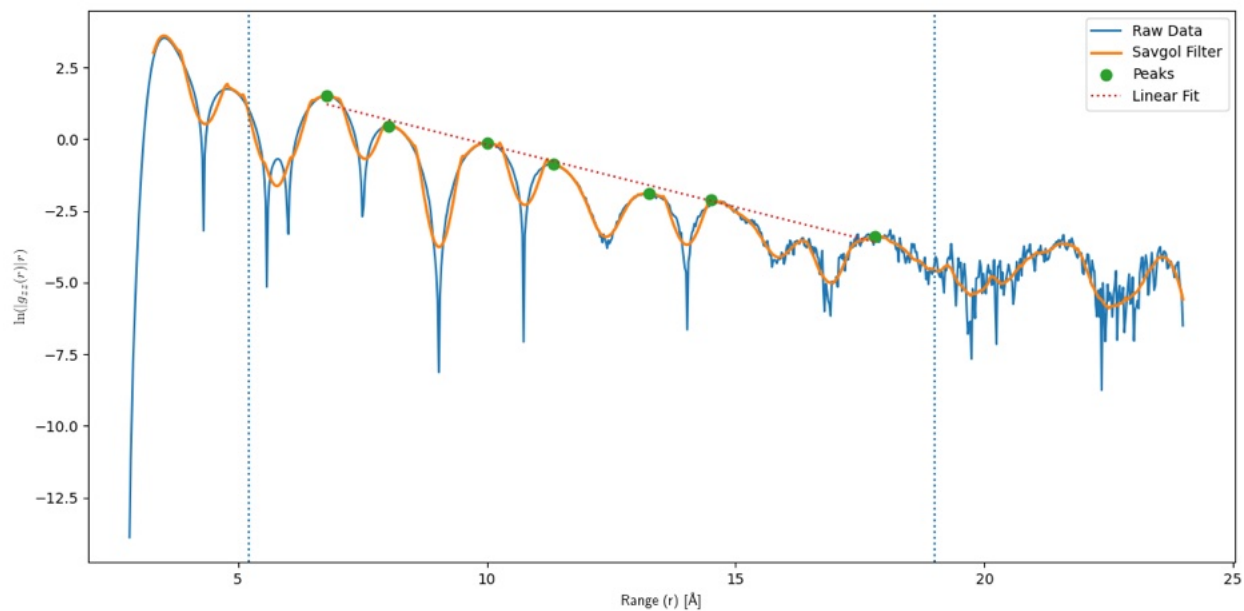


Figure S51. Fitting of aqueous CsCl at a concentration of 6.96 M. The envelope of the fit is determined by fitting through points at the top of each of the marked peaks. A Savgol filter was applied to smooth the data to assist peak finding, particularly at higher values of r . The vertical lines indicate the extrema that fitting was carried out over.

Ionic Liquid: [C₂C₁im][BF₄]

Table S7. Concentration and conventionally-derived λ_5 values for [C₂C₁im][BF₄] (see Figure S52).

Conc (M)	Decay Length (Å)
6.54	5.95 ± 0.02

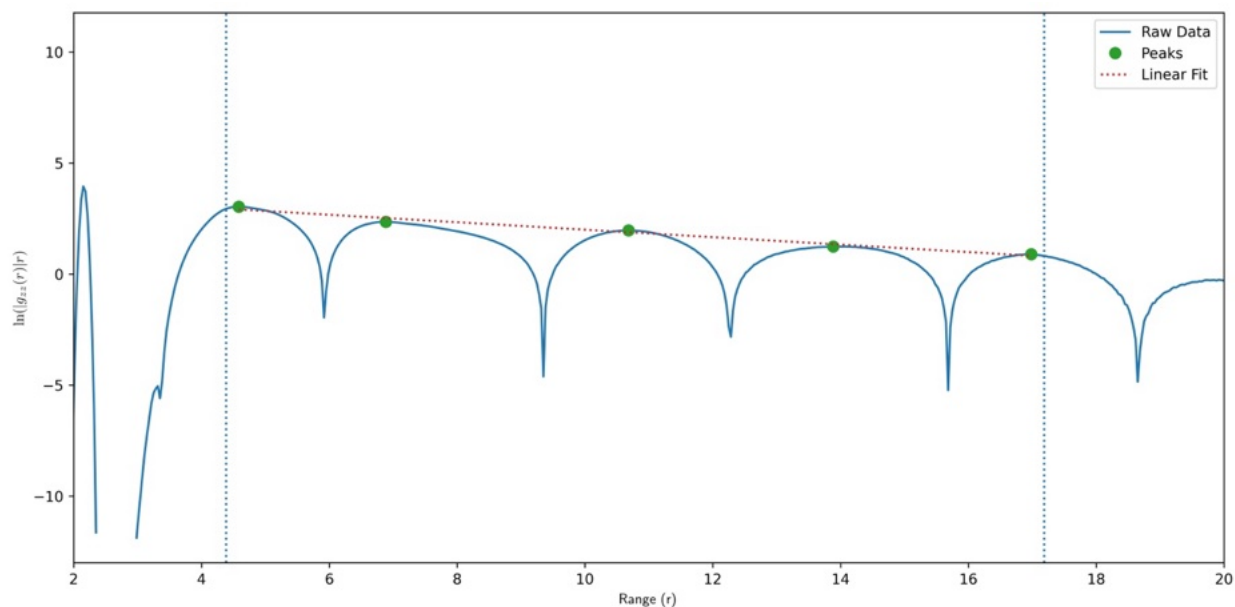


Figure S52. Fitting of [C₂C₁im][BF₄]. The envelope of the fit is determined by fitting through points at the top of each of the marked peaks. A Savgol filter was applied to smooth the data to assist peak finding, particularly at higher values of r . The vertical lines indicate the extrema that fitting was carried out over.

Derivation of λ_s via Discrete Fourier Analysis of $g_{zz}(r).r$

Lithium Chloride

Table S8. Concentration and derived λ_s values (Å) using discrete Fourier analysis for LiCl. See accompanying Figures S53-S69.

Conc (m)	Conc (M)	Mode Frequency (Å ⁻¹)						
		0.08	0.13	0.46	0.79	1.33	1.78	2.24
0.1	0.11			5.61 ± 0.08				
0.5	0.50			4.30 ± 0.05				
0.75	0.74			4.13 ± 0.05				
1.0	0.99			5.04 ± 0.07		25.91 ± 1.77		
1.25	1.23			5.21 ± 0.07		14.92 ± 0.59		
1.5	1.47			5.30 ± 0.07		21.91 ± 1.27		
2.0	1.94			5.21 ± 0.23		21.48 ± 5.60		
2.5	2.42			5.23 ± 0.23		25.21 ± 4.53	135.36 ± 30.83	
3.0	2.87			5.17 ± 0.28		30.86 ± 5.90	104.13 ± 20.33	
3.5	3.32	4.69 ± 0.22		5.26 ± 0.26		34.96 ± 5.73	120.01 ± 25.04	
4.0	3.76	4.44 ± 0.20		5.26 ± 0.25		38.85 ± 11.44	90.51 ± 23.69	
5.0	4.62	5.20 ± 0.15		5.31 ± 0.26		91.18 ± 20.62	273.45 ± 66.83	
6.0	5.45		4.93 ± 0.08	5.31 ± 0.26		126.08 ± 29.62	541.64 ± 127.59	
7.0	6.25		4.30 ± 0.28	5.33 ± 0.28		99.02 ± 29.29	552.39 ± 157.83	500.84 ± 108.54
8.0	7.02		4.15 ± 0.26	5.42 ± 0.31		140.77 ± 53.44	166.75 ± 66.46	228.93 ± 74.04
9.0	7.77		4.05 ± 0.23	5.50 ± 0.36		202.91 ± 101.63	238.11 ± 103.31	237.78 ± 52.09
10	8.49		3.89 ± 0.16	6.04 ± 0.72	11.85 ± 2.44	209.36 ± 126.96	242.41 ± 112.68	132.49 ± 23.32

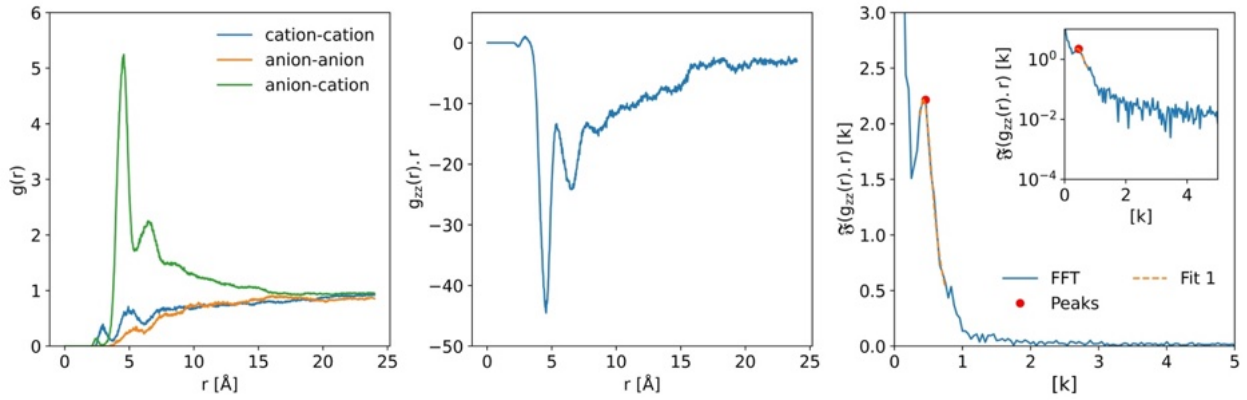


Figure S53. Derivation of λ_S using discrete Fourier Analysis for LiCl 0.11 M. (a) $g_{++}(r)$, $g_{--}(r)$ and $g_{\pm}(r)$ (b) $g_{zz}(r) \cdot r$ (c) $\mathfrak{F}[g_{zz}(r) \cdot r]$, peaks are fitted with the equation $\frac{1}{\sqrt{2\pi}} \frac{-\kappa_{\mathfrak{R}}}{k^2 + \kappa_{\mathfrak{R}}^2}$ to extract screening lengths ($\lambda = 1/\kappa$).

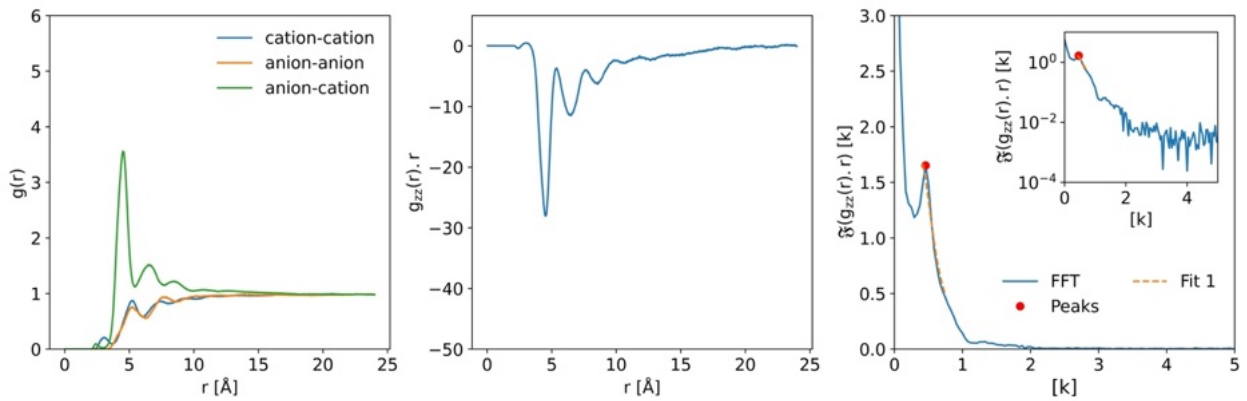


Figure S54. Derivation of λ_S using discrete Fourier Analysis for LiCl 0.50 M. (a) $g_{++}(r)$, $g_{--}(r)$ and $g_{\pm}(r)$ (b) $g_{zz}(r) \cdot r$ (c) $\mathfrak{F}[g_{zz}(r) \cdot r]$, peaks are fitted with the equation $\frac{1}{\sqrt{2\pi}} \frac{-\kappa_{\mathfrak{R}}}{k^2 + \kappa_{\mathfrak{R}}^2}$ to extract screening lengths ($\lambda = 1/\kappa$).

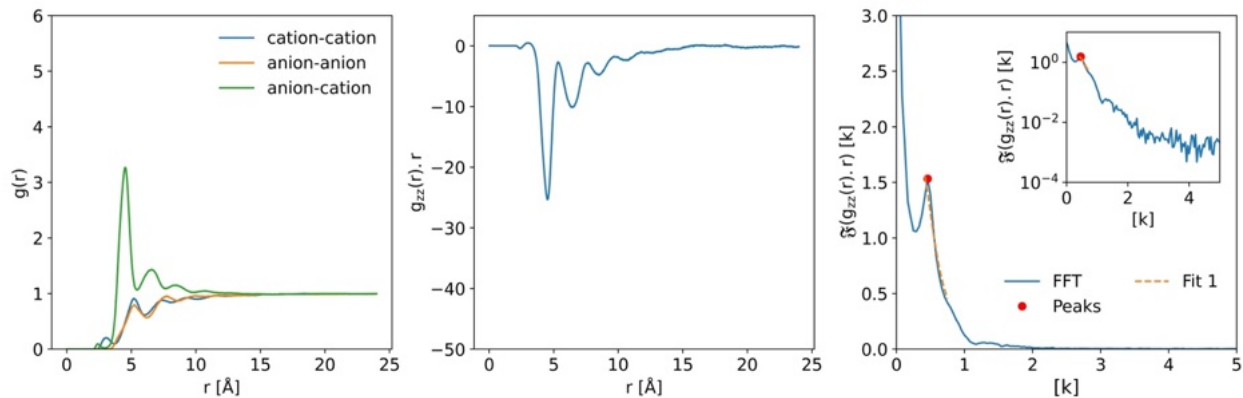


Figure S55. Derivation of λ_S using discrete Fourier Analysis for LiCl 0.74 M. (a) $g_{++}(r)$, $g_{--}(r)$ and $g_{\pm}(r)$ (b) $g_{zz}(r) \cdot r$ (c) $\mathfrak{F}[g_{zz}(r) \cdot r]$, peaks are fitted with the equation $\frac{1}{\sqrt{2\pi}} \frac{-\kappa_{\mathfrak{R}}}{k^2 + \kappa_{\mathfrak{R}}^2}$ to extract screening lengths ($\lambda = 1/\kappa$).

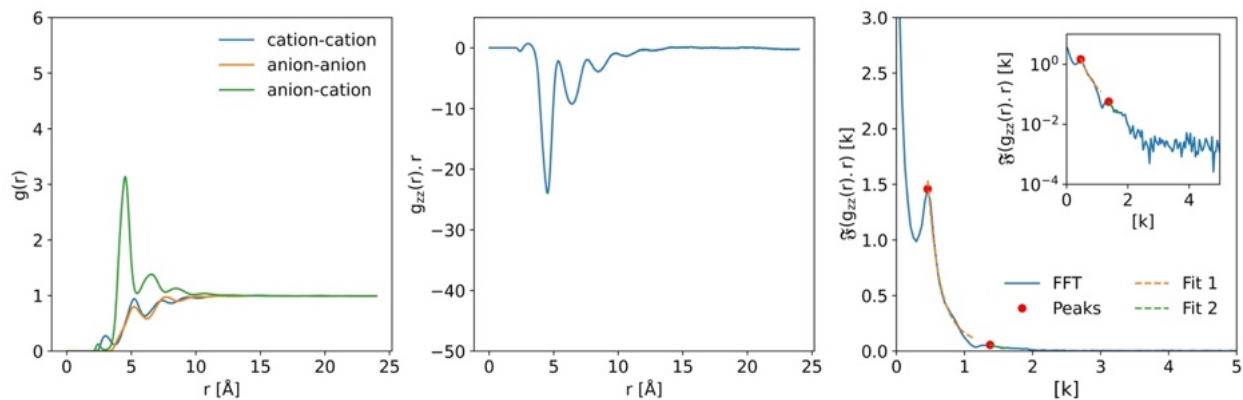


Figure S56. Derivation of λ_S using discrete Fourier Analysis for LiCl 0.99 M. (a) $g_{++}(r)$, $g_{--}(r)$ and $g_{\pm}(r)$ (b) $g_{zz}(r) \cdot r$ (c) $\mathfrak{F}[g_{zz}(r) \cdot r]$, peaks are fitted with the equation $\frac{1}{\sqrt{2\pi}} \frac{-\kappa_{\mathfrak{R}}}{k^2 + \kappa_{\mathfrak{R}}^2}$ to extract screening lengths ($\lambda = 1/\kappa$).

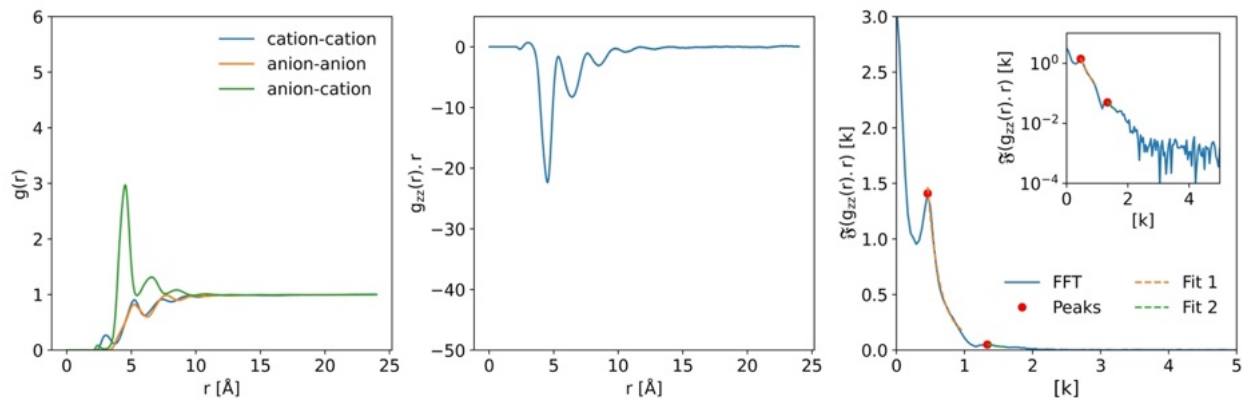


Figure S57. Derivation of λ_S using discrete Fourier Analysis for LiCl 1.23 M. (a) $g_{++}(r)$, $g_{--}(r)$ and $g_{\pm}(r)$ (b) $g_{zz}(r) \cdot r$ (c) $\mathfrak{F}[g_{zz}(r) \cdot r]$, peaks are fitted with the equation $\frac{1}{\sqrt{2\pi}} \frac{-\kappa_{\mathfrak{R}}}{k^2 + \kappa_{\mathfrak{R}}^2}$ to extract screening lengths ($\lambda = 1/\kappa$).

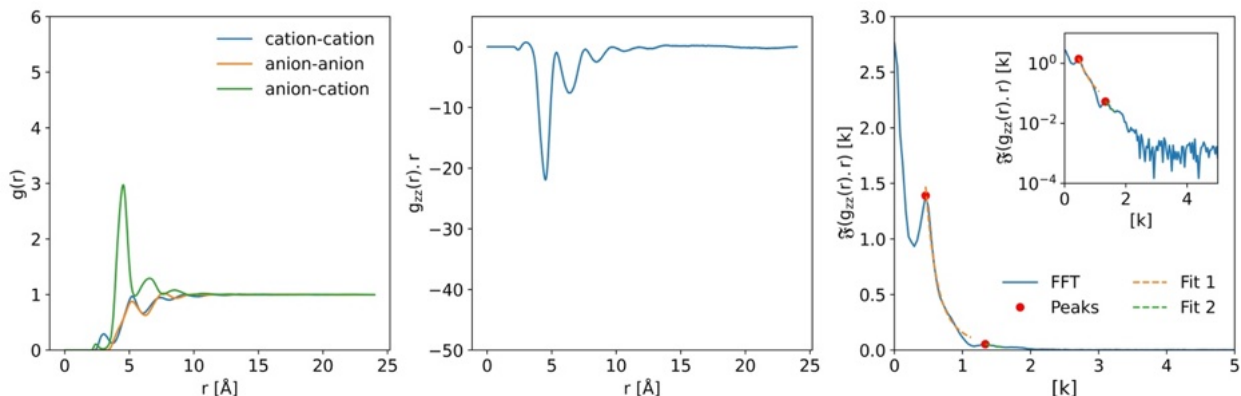


Figure S58. Derivation of λ_S using discrete Fourier Analysis for LiCl 1.47 M. (a) $g_{++}(r)$, $g_{--}(r)$ and $g_{\pm}(r)$ (b) $g_{zz}(r) \cdot r$ (c) $\mathfrak{F}[g_{zz}(r) \cdot r]$, peaks are fitted with the equation $\frac{1}{\sqrt{2\pi}} \frac{-\kappa_{\mathfrak{R}}}{k^2 + \kappa_{\mathfrak{R}}^2}$ to extract screening lengths ($\lambda = 1/\kappa$).

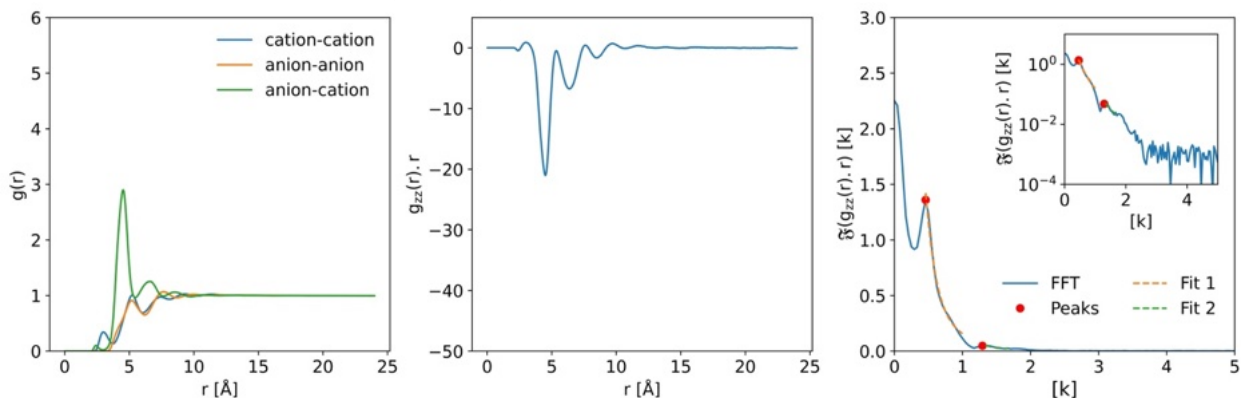


Figure S59. Derivation of λ_S using discrete Fourier Analysis for LiCl 1.94 M. (a) $g_{++}(r)$, $g_{--}(r)$ and $g_{\pm}(r)$ (b) $g_{zz}(r) \cdot r$ (c) $\mathfrak{F}[g_{zz}(r) \cdot r]$, peaks are fitted with the equation $\frac{1}{\sqrt{2\pi}} \frac{-\kappa_{\mathfrak{R}}}{k^2 + \kappa_{\mathfrak{R}}^2}$ to extract screening lengths ($\lambda = 1/\kappa$).

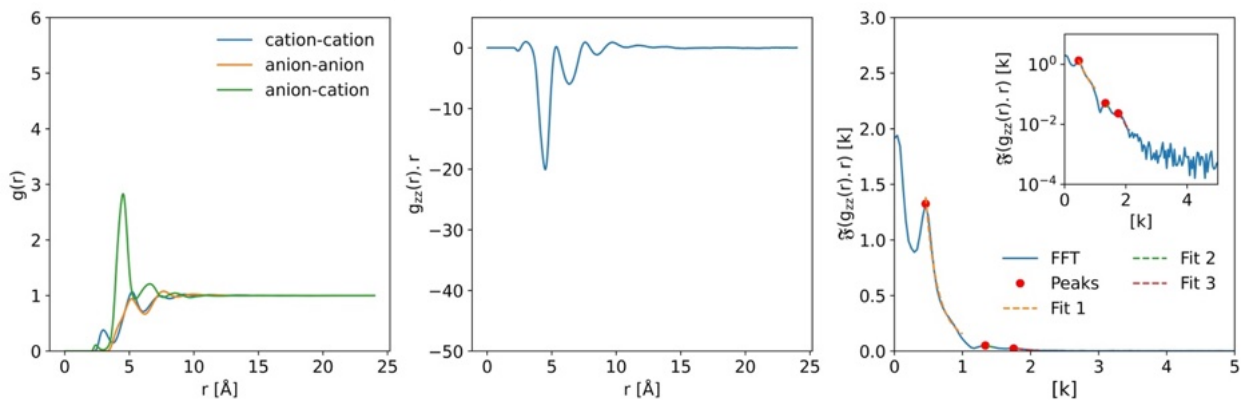


Figure S60. Derivation of λ_S using discrete Fourier Analysis for LiCl 2.42 M. (a) $g_{++}(r)$, $g_{--}(r)$ and $g_{\pm}(r)$ (b) $g_{zz}(r) \cdot r$ (c) $\mathfrak{F}[g_{zz}(r) \cdot r]$, peaks are fitted with the equation $\frac{1}{\sqrt{2\pi}} \frac{-\kappa_{\mathfrak{R}}}{k^2 + \kappa_{\mathfrak{R}}^2}$ to extract screening lengths ($\lambda = 1/\kappa$).

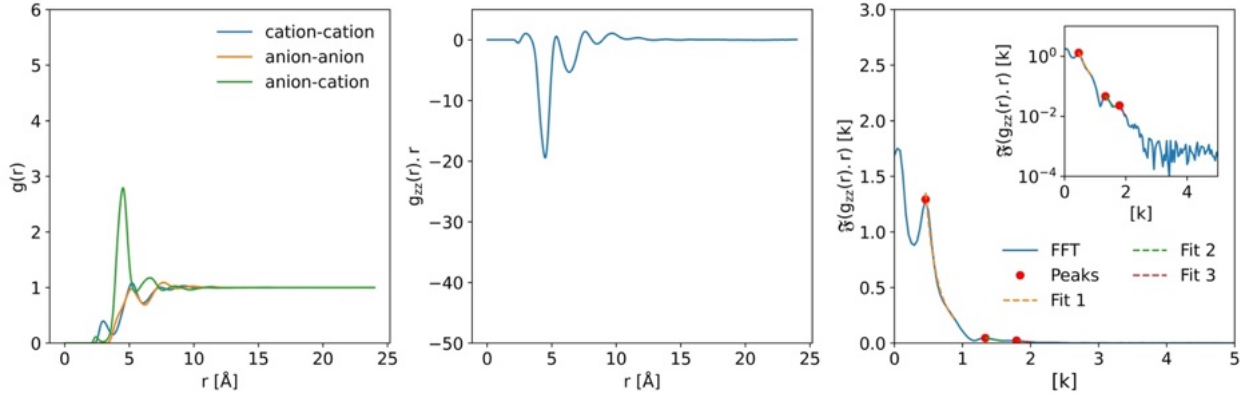


Figure S61. Derivation of λ_S using discrete Fourier Analysis for LiCl 2.87 M. (a) $g_{++}(r)$, $g_{--}(r)$ and $g_{+-}(r)$ (b) $g_{zz}(r) \cdot r$ (c) $\mathfrak{F}[g_{zz}(r) \cdot r]$, peaks are fitted with the equation $\frac{1}{\sqrt{2\pi}} \frac{e^{-\kappa_{\mathfrak{F}} r}}{k^2 + \kappa_{\mathfrak{F}}^2}$ to extract screening lengths ($\lambda = 1/\kappa$).

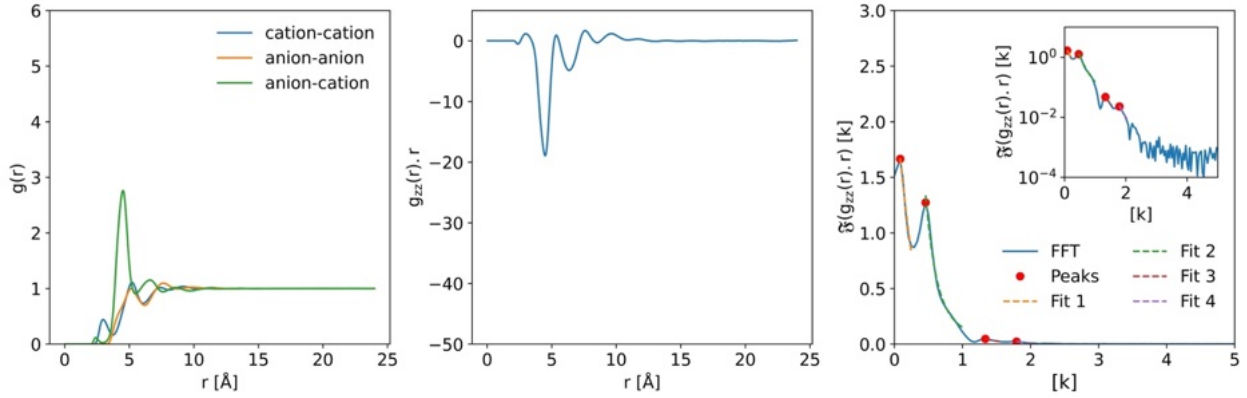


Figure S62. Derivation of λ_S using discrete Fourier Analysis for LiCl 3.32 M. (a) $g_{++}(r)$, $g_{--}(r)$ and $g_{+-}(r)$ (b) $g_{zz}(r) \cdot r$ (c) $\mathfrak{F}[g_{zz}(r) \cdot r]$, peaks are fitted with the equation $\frac{1}{\sqrt{2\pi}} \frac{e^{-\kappa_{\mathfrak{F}} r}}{k^2 + \kappa_{\mathfrak{F}}^2}$ to extract screening lengths ($\lambda = 1/\kappa$).

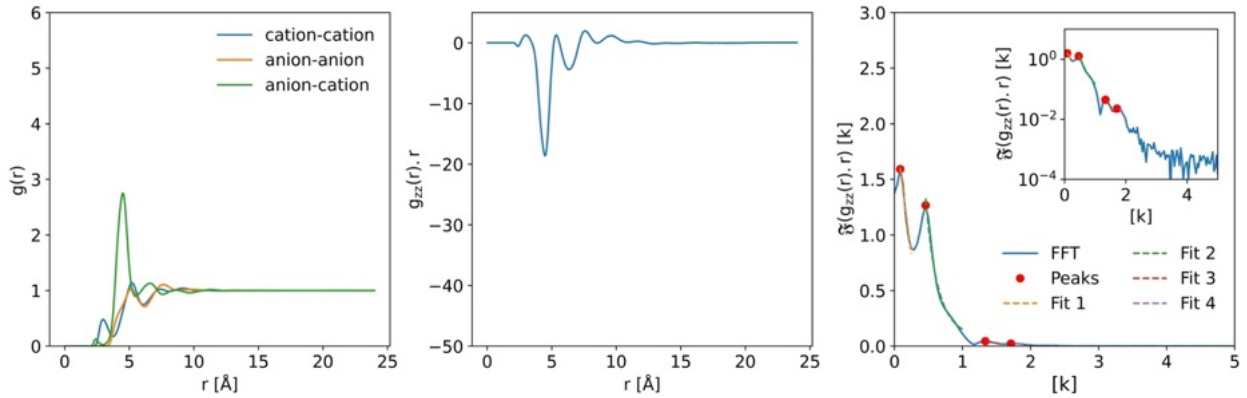


Figure S63. Derivation of λ_S using discrete Fourier Analysis for LiCl 3.76 M. (a) $g_{++}(r)$, $g_{--}(r)$ and $g_{+-}(r)$ (b) $g_{zz}(r) \cdot r$ (c) $\mathfrak{F}[g_{zz}(r) \cdot r]$, peaks are fitted with the equation $\frac{1}{\sqrt{2\pi}} \frac{e^{-\kappa_{\mathfrak{F}} r}}{k^2 + \kappa_{\mathfrak{F}}^2}$ to extract screening lengths ($\lambda = 1/\kappa$).

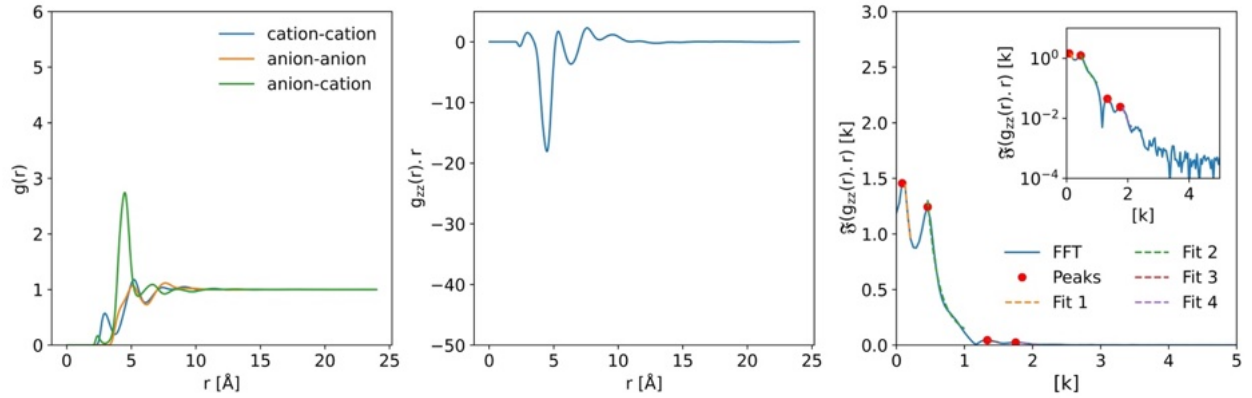


Figure S64. Derivation of λ_S using discrete Fourier Analysis for LiCl 4.62 M. (a) $g_{++}(r)$, $g_{--}(r)$ and $g_{\pm}(r)$ (b) $g_{zz}(r) \cdot r$ (c) $\mathfrak{F}[g_{zz}(r) \cdot r]$, peaks are fitted with the equation $\frac{1}{\sqrt{2\pi}} \frac{e^{-\kappa_{\mathfrak{F}} r}}{k^2 + \kappa_{\mathfrak{F}}^2}$ to extract screening lengths ($\lambda = 1/\kappa$).

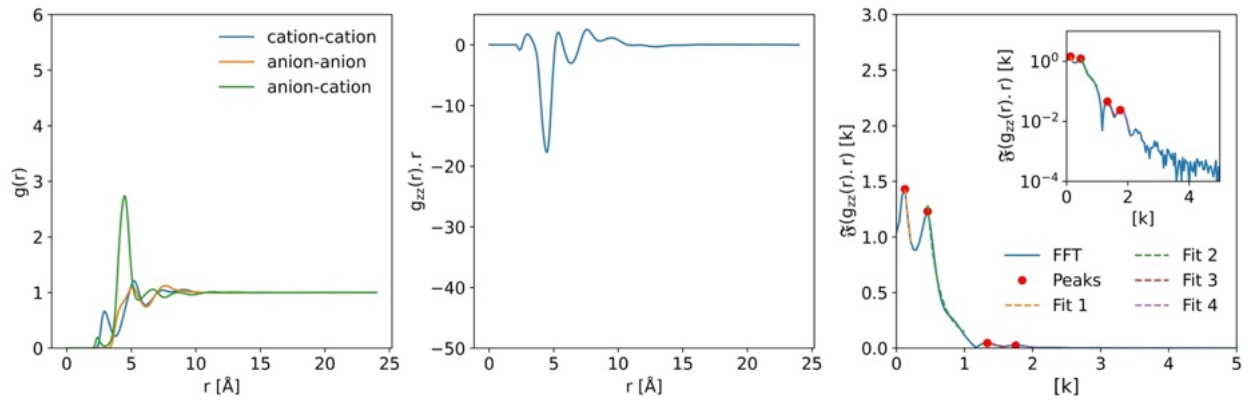


Figure S65. Derivation of λ_S using discrete Fourier Analysis for LiCl 5.45 M. (a) $g_{++}(r)$, $g_{--}(r)$ and $g_{\pm}(r)$ (b) $g_{zz}(r) \cdot r$ (c) $\mathfrak{F}[g_{zz}(r) \cdot r]$, peaks are fitted with the equation $\frac{1}{\sqrt{2\pi}} \frac{e^{-\kappa_{\mathfrak{F}} r}}{k^2 + \kappa_{\mathfrak{F}}^2}$ to extract screening lengths ($\lambda = 1/\kappa$).

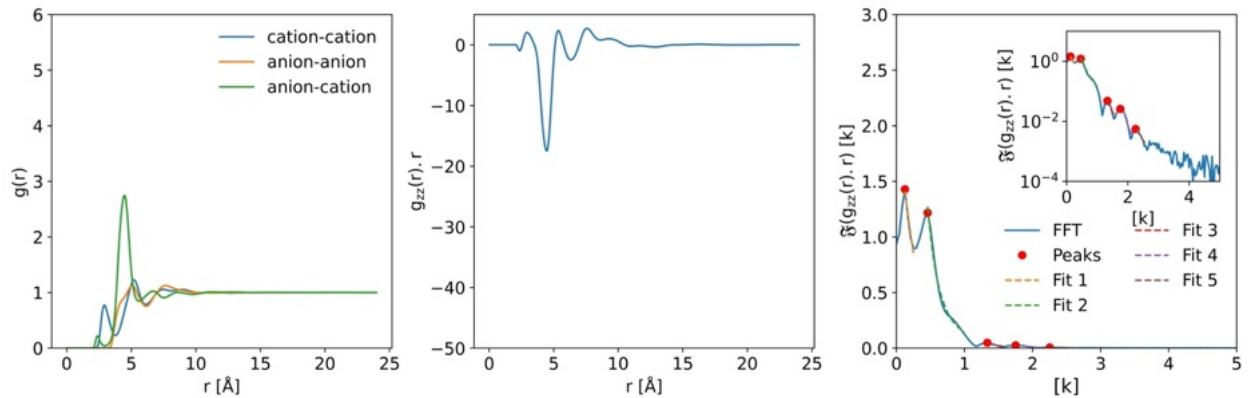


Figure S66. Derivation of λ_S using discrete Fourier Analysis for LiCl 6.25 M. (a) $g_{++}(r)$, $g_{--}(r)$ and $g_{\pm}(r)$ (b) $g_{zz}(r) \cdot r$ (c) $\mathfrak{F}[g_{zz}(r) \cdot r]$, peaks are fitted with the equation $\frac{1}{\sqrt{2\pi}} \frac{e^{-\kappa_{\mathfrak{F}} r}}{k^2 + \kappa_{\mathfrak{F}}^2}$ to extract screening lengths ($\lambda = 1/\kappa$).

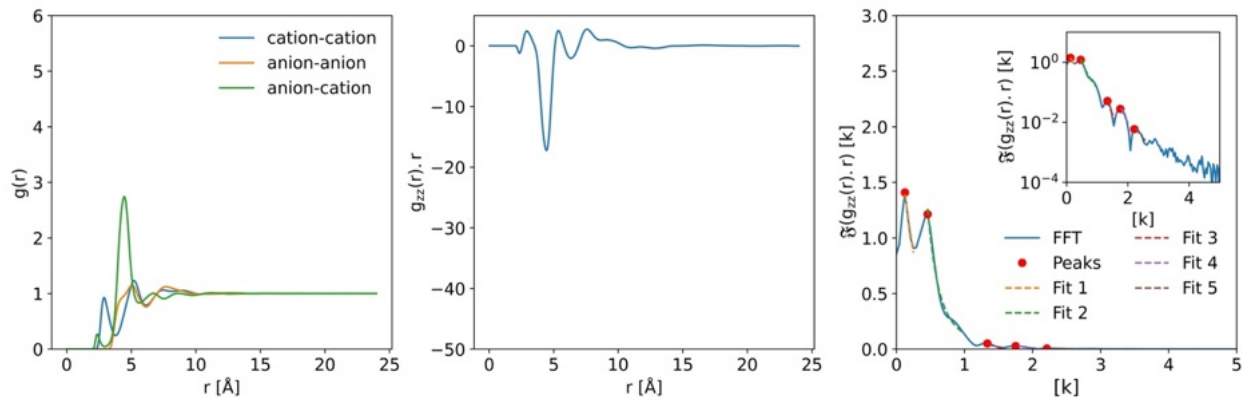


Figure S67. Derivation of λ_S using discrete Fourier Analysis for LiCl 7.02 M. (a) $g_{++}(r)$, $g_{--}(r)$ and $g_{\pm}(r)$ (b) $g_{zz}(r) \cdot r$ (c) $\mathfrak{F}[g_{zz}(r) \cdot r]$, peaks are fitted with the equation $\frac{1}{\sqrt{2\pi}} \frac{e^{-\kappa_{\mathfrak{F}} r}}{k^2 + \kappa_{\mathfrak{F}}^2}$ to extract screening lengths ($\lambda = 1/\kappa$).

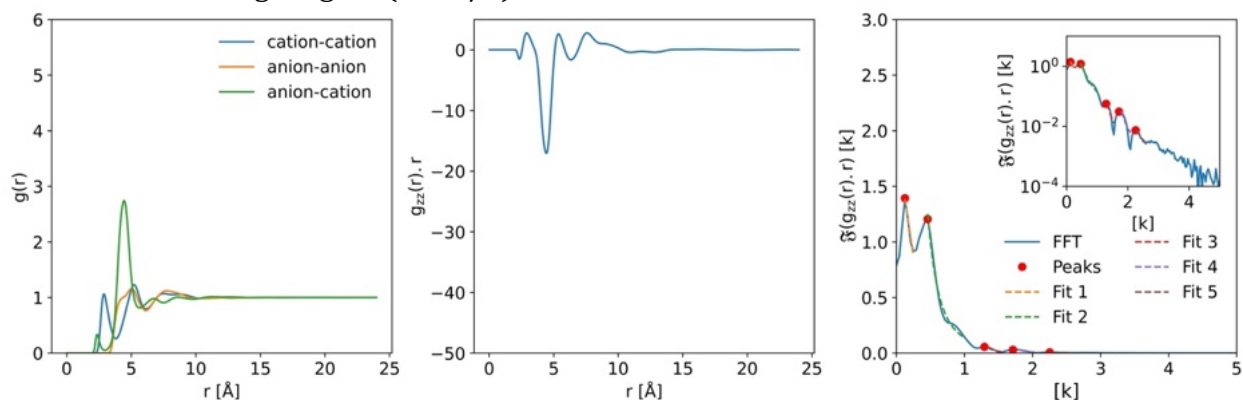


Figure S68. Derivation of λ_S using discrete Fourier Analysis for LiCl 7.78 M. (a) $g_{++}(r)$, $g_{--}(r)$ and $g_{\pm}(r)$ (b) $g_{zz}(r) \cdot r$ (c) $\mathfrak{F}[g_{zz}(r) \cdot r]$, peaks are fitted with the equation $\frac{1}{\sqrt{2\pi}} \frac{e^{-\kappa_{\mathfrak{F}} r}}{k^2 + \kappa_{\mathfrak{F}}^2}$ to extract screening lengths ($\lambda = 1/\kappa$).

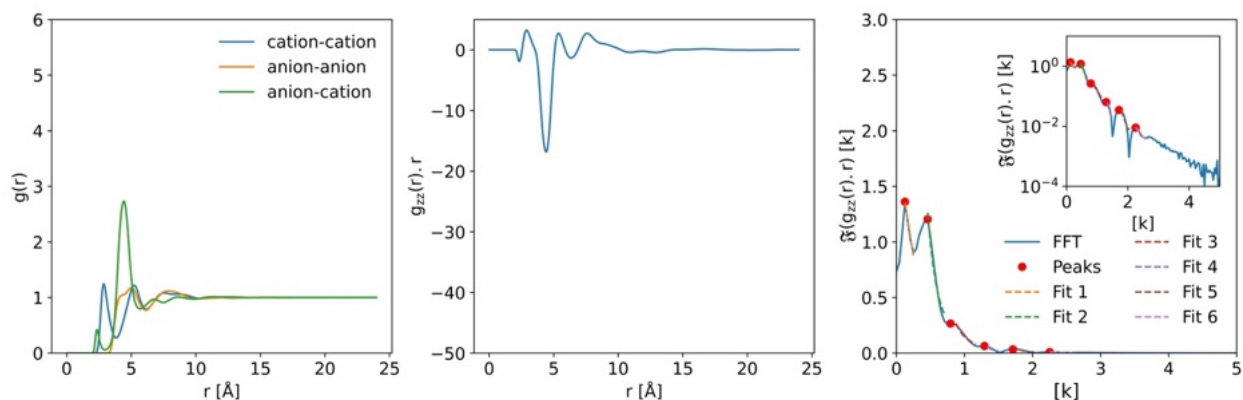


Figure S69. Derivation of λ_S using discrete Fourier Analysis for LiCl 8.49 M. (a) $g_{++}(r)$, $g_{--}(r)$ and $g_{\pm}(r)$ (b) $g_{zz}(r) \cdot r$ (c) $\mathfrak{F}[g_{zz}(r) \cdot r]$, peaks are fitted with the equation $\frac{1}{\sqrt{2\pi}} \frac{e^{-\kappa_{\mathfrak{F}} r}}{k^2 + \kappa_{\mathfrak{F}}^2}$ to extract screening lengths ($\lambda = 1/\kappa$).

Sodium Chloride

Table S9. Concentration and derived λ_{G} values (\AA) using discrete Fourier analysis for NaCl. See accompanying Figures S70-S82.

Conc (m)	Conc (M)	Mode Frequency (\AA^{-1})				
		0.04	0.08	0.46	1.21	1.78
0.1	0.11			7.25 ± 1.88		
0.5	0.50			6.95 ± 0.58		
0.75	0.74			6.64 ± 0.60		
1.0	0.99			6.66 ± 0.63	23.23 ± 6.38	
1.25	1.23			6.60 ± 0.47	25.01 ± 7.51	16.33 ± 2.22
1.5	1.48			6.47 ± 0.48	25.22 ± 6.14	16.98 ± 2.74
2.0	1.95	5.43 ± 0.13		6.51 ± 0.19	25.69 ± 5.63	20.21 ± 4.14
2.5	2.42	4.70 ± 0.25		6.36 ± 0.58	25.58 ± 6.72	18.12 ± 2.48
3.0	2.87		5.12 ± 0.26	6.18 ± 0.55	23.53 ± 6.77	18.05 ± 3.14
3.5	3.32		4.46 ± 0.41	6.04 ± 0.56	24.16 ± 6.83	20.45 ± 2.34
4.0	3.75		4.45 ± 0.41	5.89 ± 0.56	24.93 ± 6.84	17.03 ± 3.82
5.0	4.60		4.68 ± 0.39	5.47 ± 0.53	23.61 ± 6.04	21.92 ± 2.95
6.0	5.41		4.19 ± 0.53	5.16 ± 0.50	23.15 ± 5.11	22.56 ± 1.63

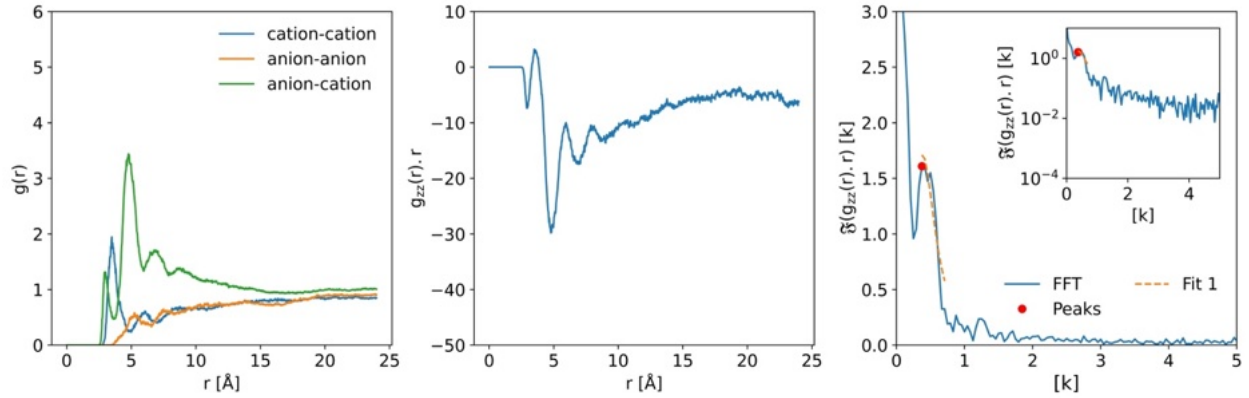


Figure S70. Derivation of λ_S using discrete Fourier Analysis for NaCl 0.11 M. (a) $g_{++}(r)$, $g_{--}(r)$ and $g_{\pm}(r)$ (b) $g_{zz}(r) \cdot r$ (c) $\mathfrak{F}[g_{zz}(r) \cdot r]$, peaks are fitted with the equation $\frac{1}{\sqrt{2\pi}} \frac{e^{-\kappa_{\mathfrak{F}} r}}{k^2 + \kappa_{\mathfrak{F}}^2}$ to extract screening lengths ($\lambda = 1/\kappa$).

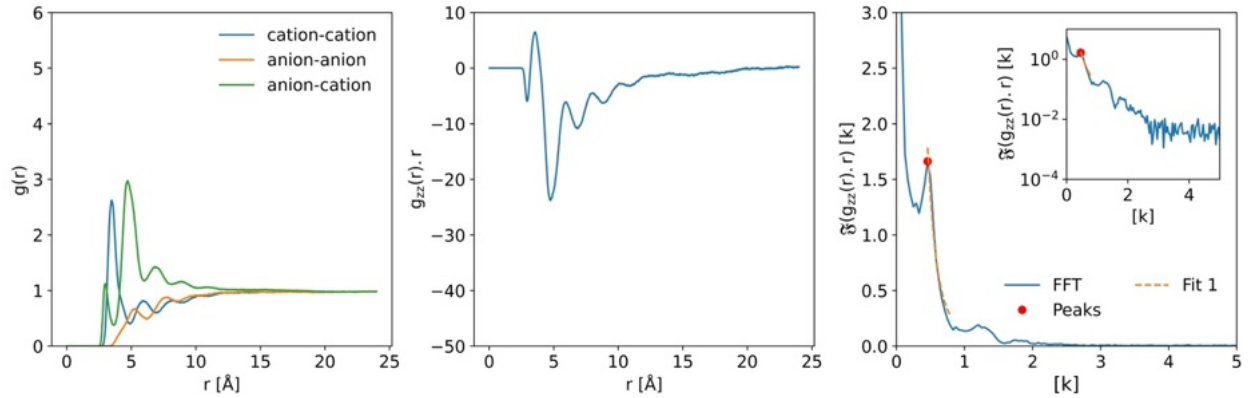


Figure S71. Derivation of λ_S using discrete Fourier Analysis for NaCl 0.50 M. (a) $g_{++}(r)$, $g_{--}(r)$ and $g_{\pm}(r)$ (b) $g_{zz}(r) \cdot r$ (c) $\mathfrak{F}[g_{zz}(r) \cdot r]$, peaks are fitted with the equation $\frac{1}{\sqrt{2\pi}} \frac{e^{-\kappa_{\mathfrak{F}} r}}{k^2 + \kappa_{\mathfrak{F}}^2}$ to extract screening lengths ($\lambda = 1/\kappa$).

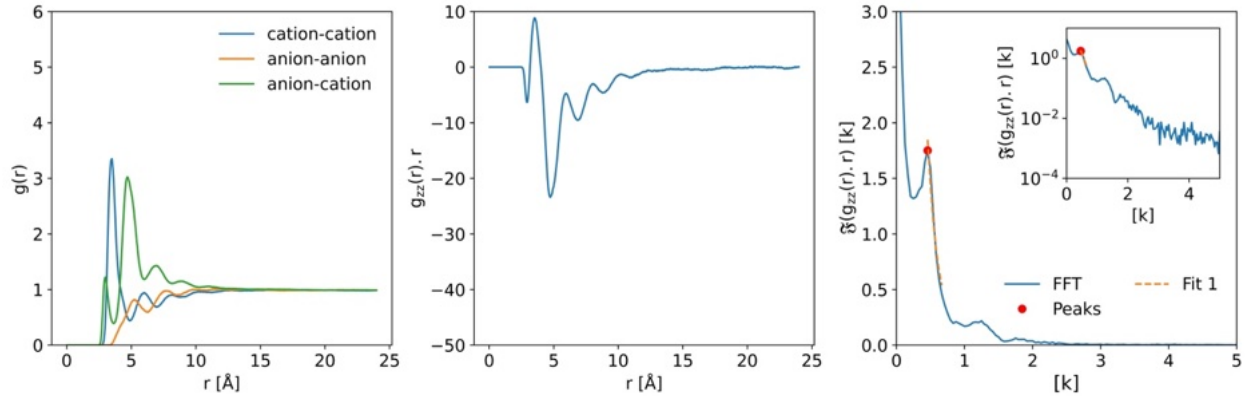


Figure S72. Derivation of λ_S using discrete Fourier Analysis for NaCl 0.74 M. (a) $g_{++}(r)$, $g_{--}(r)$ and $g_{\pm}(r)$ (b) $g_{zz}(r) \cdot r$ (c) $\mathfrak{F}[g_{zz}(r) \cdot r]$, peaks are fitted with the equation $\frac{1}{\sqrt{2\pi}} \frac{e^{-\kappa_{\mathfrak{F}} r}}{k^2 + \kappa_{\mathfrak{F}}^2}$ to extract screening lengths ($\lambda = 1/\kappa$).

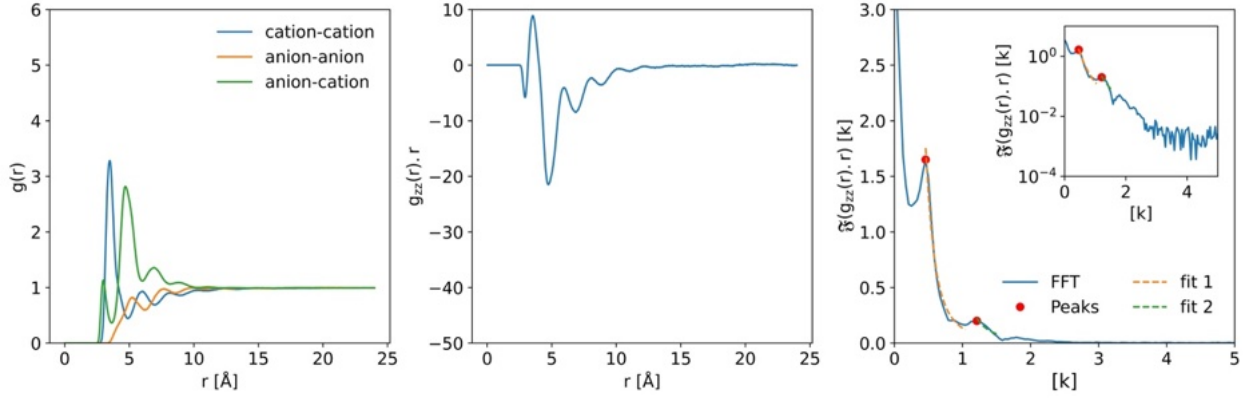


Figure S73. Derivation of λ_S using discrete Fourier Analysis for NaCl 0.99 M. (a) $g_{++}(r)$, $g_{--}(r)$ and $g_{+-}(r)$ (b) $g_{zz}(r) \cdot r$ (c) $\mathfrak{F}[g_{zz}(r) \cdot r]$, peaks are fitted with the equation $\frac{1}{\sqrt{2\pi}} \frac{e^{-\kappa_{\mathfrak{F}} r}}{k^2 + \kappa_{\mathfrak{F}}^2}$ to extract screening lengths ($\lambda = 1/\kappa$).

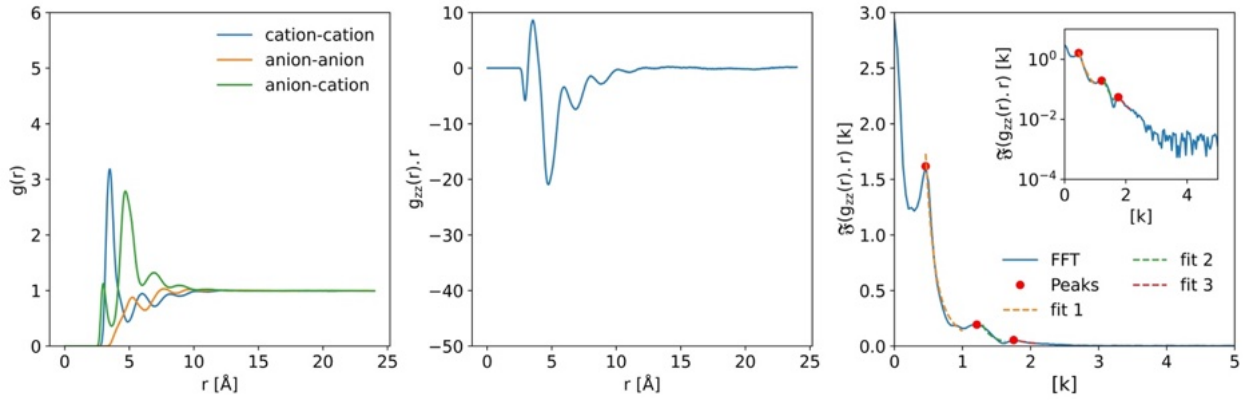


Figure S74. Derivation of λ_S using discrete Fourier Analysis for NaCl 1.23 M. (a) $g_{++}(r)$, $g_{--}(r)$ and $g_{+-}(r)$ (b) $g_{zz}(r) \cdot r$ (c) $\mathfrak{F}[g_{zz}(r) \cdot r]$, peaks are fitted with the equation $\frac{1}{\sqrt{2\pi}} \frac{e^{-\kappa_{\mathfrak{F}} r}}{k^2 + \kappa_{\mathfrak{F}}^2}$ to extract screening lengths ($\lambda = 1/\kappa$).

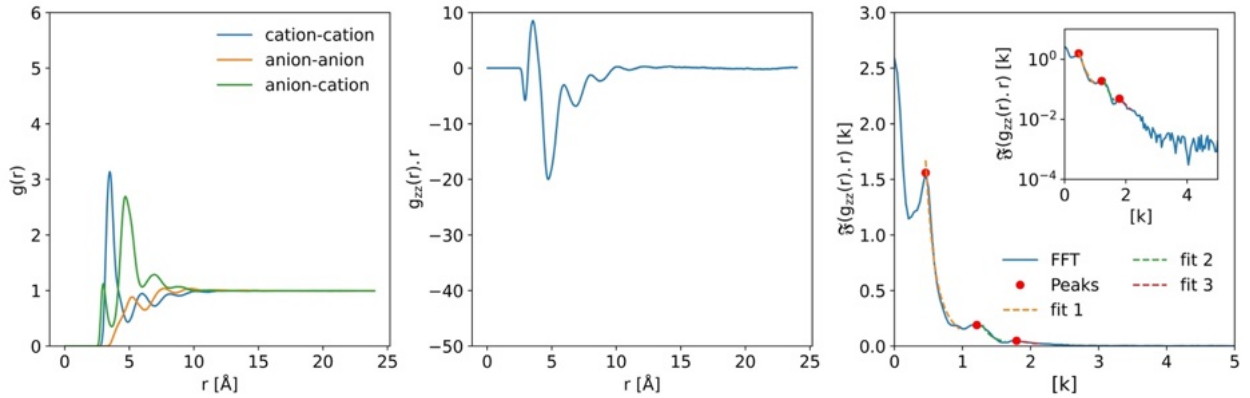


Figure S75. Derivation of λ_S using discrete Fourier Analysis for NaCl 1.48 M. (a) $g_{++}(r)$, $g_{--}(r)$ and $g_{+-}(r)$ (b) $g_{zz}(r) \cdot r$ (c) $\mathfrak{F}[g_{zz}(r) \cdot r]$, peaks are fitted with the equation $\frac{1}{\sqrt{2\pi}} \frac{e^{-\kappa_{\mathfrak{F}} r}}{k^2 + \kappa_{\mathfrak{F}}^2}$ to extract screening lengths ($\lambda = 1/\kappa$).

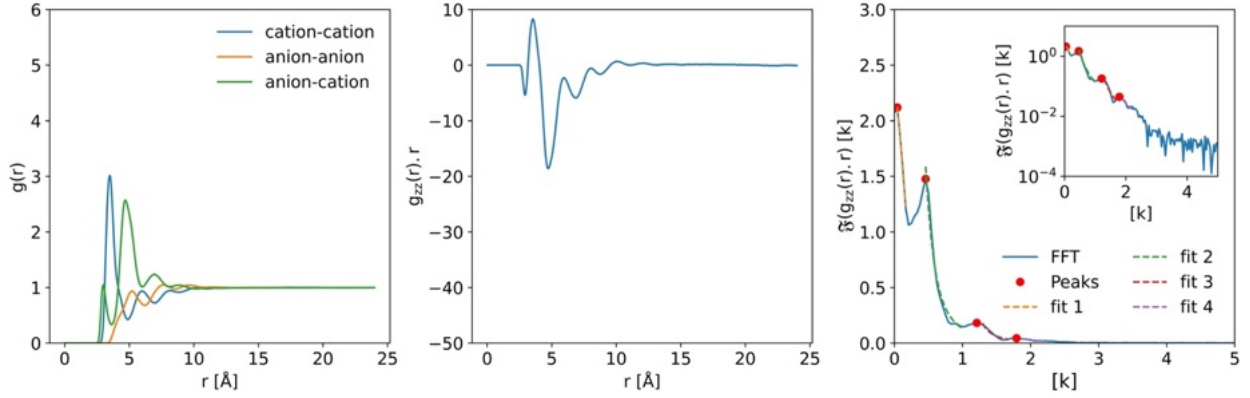


Figure S76. Derivation of λ_S using discrete Fourier Analysis for NaCl 1.95 M. (a) $g_{++}(r)$, $g_{--}(r)$ and $g_{+-}(r)$ (b) $g_{zz}(r) \cdot r$ (c) $\mathfrak{F}[g_{zz}(r) \cdot r]$, peaks are fitted with the equation $\frac{1}{\sqrt{2\pi}} \frac{-\kappa_{\mathfrak{F}}}{k^2 + \kappa_{\mathfrak{F}}^2}$ to extract screening lengths ($\lambda = 1/\kappa$).

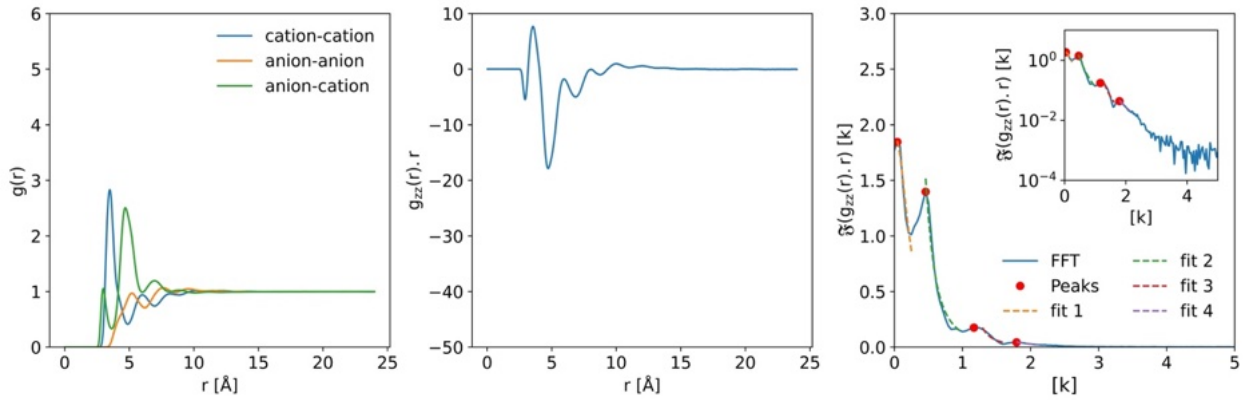


Figure S77. Derivation of λ_S using discrete Fourier Analysis for NaCl 2.42 M. (a) $g_{++}(r)$, $g_{--}(r)$ and $g_{+-}(r)$ (b) $g_{zz}(r) \cdot r$ (c) $\mathfrak{F}[g_{zz}(r) \cdot r]$, peaks are fitted with the equation $\frac{1}{\sqrt{2\pi}} \frac{-\kappa_{\mathfrak{F}}}{k^2 + \kappa_{\mathfrak{F}}^2}$ to extract screening lengths ($\lambda = 1/\kappa$).

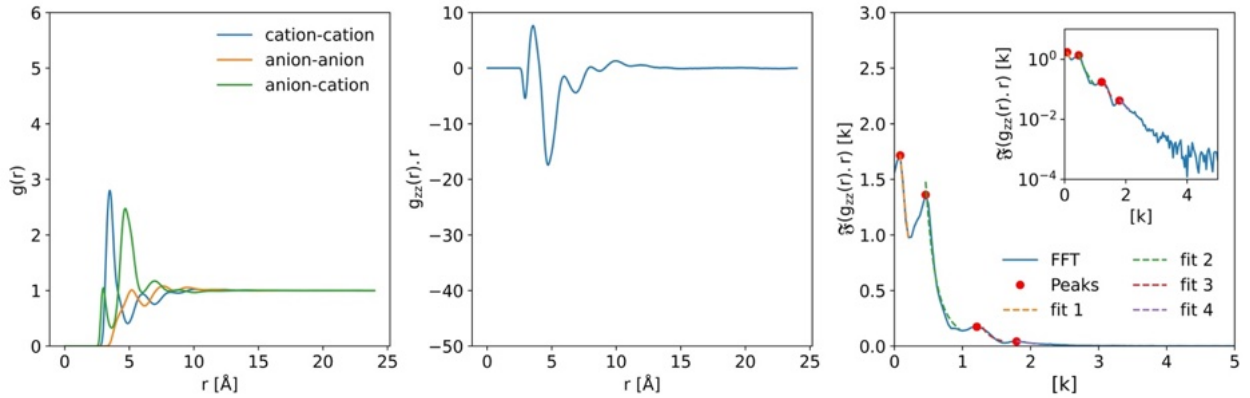


Figure S78. Derivation of λ_S using discrete Fourier Analysis for NaCl 2.87 M. (a) $g_{++}(r)$, $g_{--}(r)$ and $g_{+-}(r)$ (b) $g_{zz}(r) \cdot r$ (c) $\mathfrak{F}[g_{zz}(r) \cdot r]$, peaks are fitted with the equation $\frac{1}{\sqrt{2\pi}} \frac{-\kappa_{\mathfrak{F}}}{k^2 + \kappa_{\mathfrak{F}}^2}$ to extract screening lengths ($\lambda = 1/\kappa$).

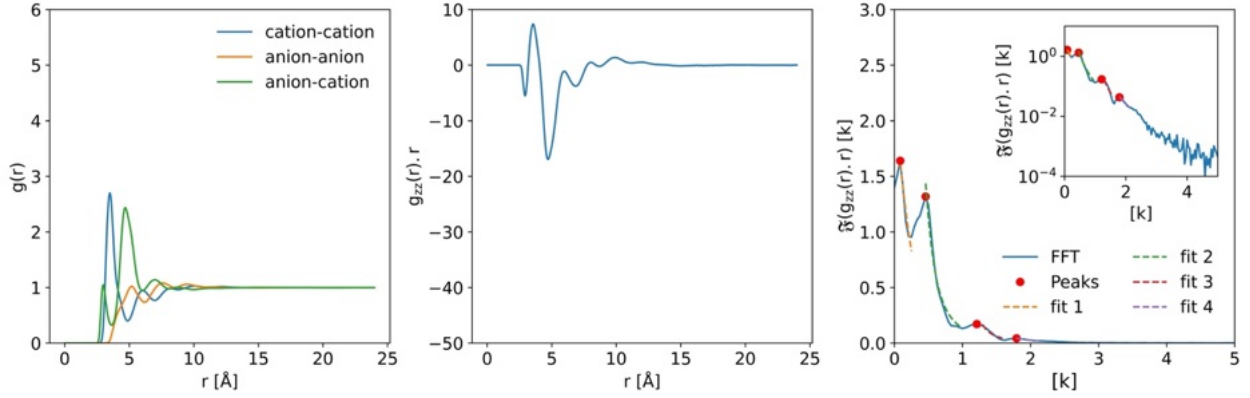


Figure S79. Derivation of λ_S using discrete Fourier Analysis for NaCl 3.32 M. (a) $g_{++}(r)$, $g_{--}(r)$ and $g_{+-}(r)$ (b) $g_{zz}(r) \cdot r$ (c) $\mathfrak{F}[g_{zz}(r) \cdot r]$, peaks are fitted with the equation $\frac{1}{\sqrt{2\pi}} \frac{e^{-\kappa_{\mathfrak{F}} r}}{k^2 + \kappa_{\mathfrak{F}}^2}$ to extract screening lengths ($\lambda = 1/\kappa$).

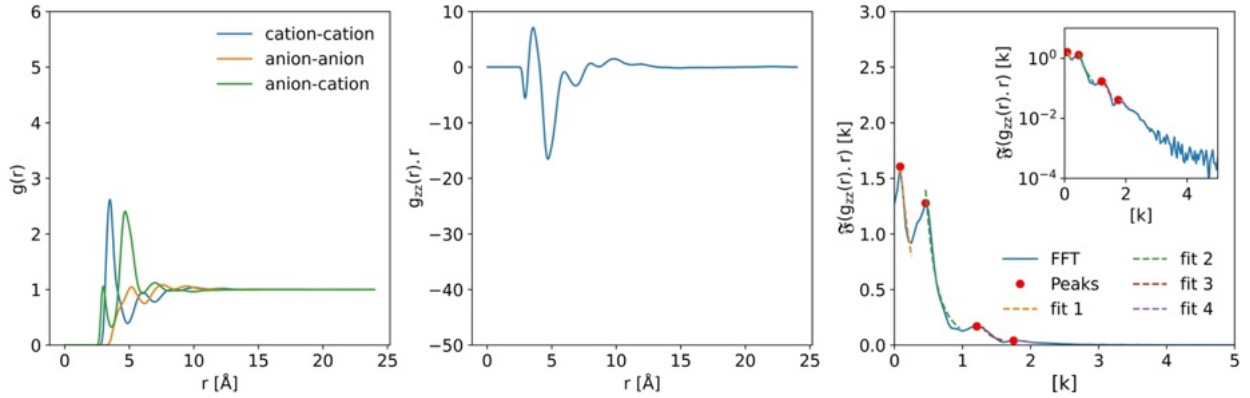


Figure S80. Derivation of λ_S using discrete Fourier Analysis for NaCl 3.75 M. (a) $g_{++}(r)$, $g_{--}(r)$ and $g_{+-}(r)$ (b) $g_{zz}(r) \cdot r$ (c) $\mathfrak{F}[g_{zz}(r) \cdot r]$, peaks are fitted with the equation $\frac{1}{\sqrt{2\pi}} \frac{e^{-\kappa_{\mathfrak{F}} r}}{k^2 + \kappa_{\mathfrak{F}}^2}$ to extract screening lengths ($\lambda = 1/\kappa$).

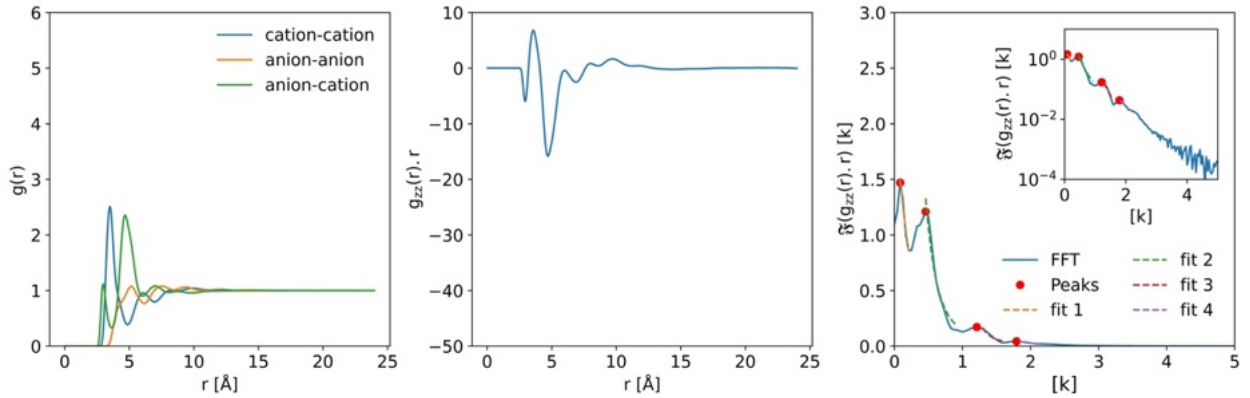


Figure S81. Derivation of λ_S using discrete Fourier Analysis for NaCl 4.60 M. (a) $g_{++}(r)$, $g_{--}(r)$ and $g_{+-}(r)$ (b) $g_{zz}(r) \cdot r$ (c) $\mathfrak{F}[g_{zz}(r) \cdot r]$, peaks are fitted with the equation $\frac{1}{\sqrt{2\pi}} \frac{e^{-\kappa_{\mathfrak{F}} r}}{k^2 + \kappa_{\mathfrak{F}}^2}$ to extract screening lengths ($\lambda = 1/\kappa$).

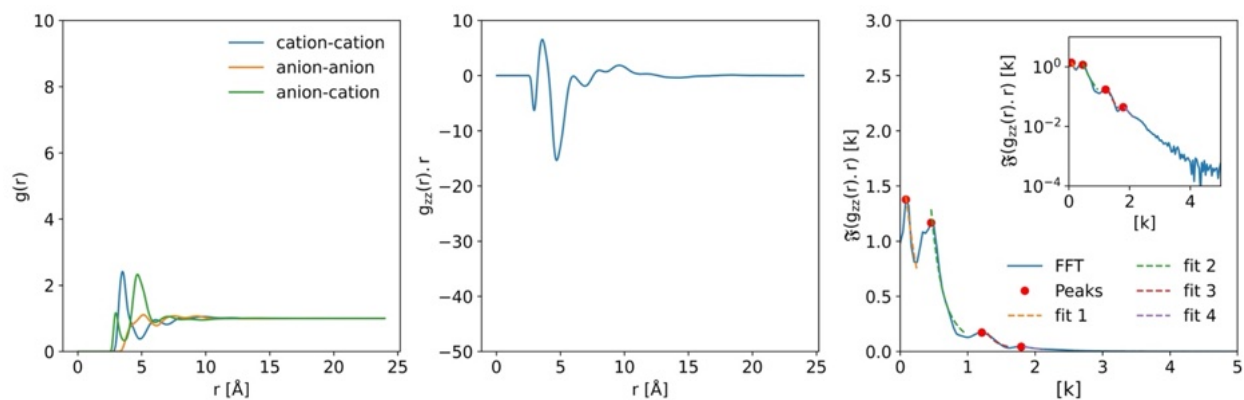


Figure S82. Derivation of λ_s using discrete Fourier Analysis for NaCl 5.41 M. (a) $g_{++}(r)$, $g_{--}(r)$ and $g_{\pm}(r)$ (b) $g_{zz}(r) \cdot r$ (c) $\mathfrak{F}[g_{zz}(r) \cdot r]$, peaks are fitted with the equation $\frac{1}{\sqrt{2\pi}} \frac{-\kappa_{\mathfrak{R}}}{k^2 + \kappa_{\mathfrak{I}}^2}$ to extract screening lengths ($\lambda = 1/\kappa$).

Potassium Chloride

Table S10. Concentration and derived λ_S values (\AA) using discrete Fourier analysis for KCl. See accompanying Figures S83-S91.

Conc (m)	Conc (M)	Mode Frequency $0.46 \text{ (\AA}^{-1}\text{)}$
0.1	0.11	5.61 ± 5.61
0.5	0.50	4.70 ± 4.70
0.75	0.73	4.72 ± 4.72
1.0	0.98	4.55 ± 4.55
1.25	1.22	4.47 ± 4.47
1.5	1.45	4.34 ± 4.34
2.0	1.90	4.28 ± 4.28
3.0	2.78	4.23 ± 4.23
4.0	3.60	4.19 ± 4.19

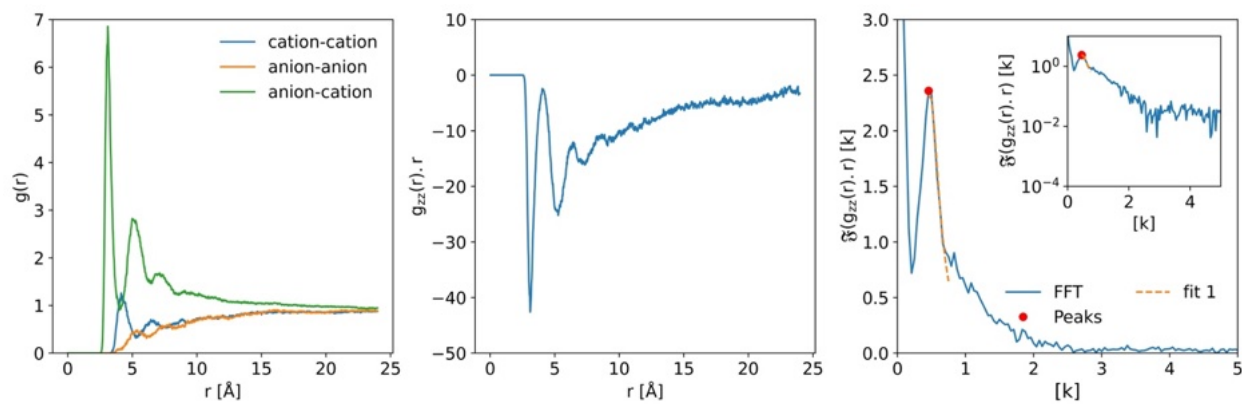


Figure S83. Derivation of λ_S using discrete Fourier Analysis for KCl 0.11 M. (a) $g_{++}(r)$, $g_{--}(r)$ and $g_{+-}(r)$ (b) $g_{zz}(r) \cdot r$ (c) $\mathfrak{F}[g_{zz}(r) \cdot r]$, peaks are fitted with the equation $\frac{1}{\sqrt{2\pi}} \frac{e^{-\kappa_{\text{fit}} r}}{k^2 + \kappa_{\text{fit}}^2}$ to extract screening lengths ($\lambda = 1/\kappa$).

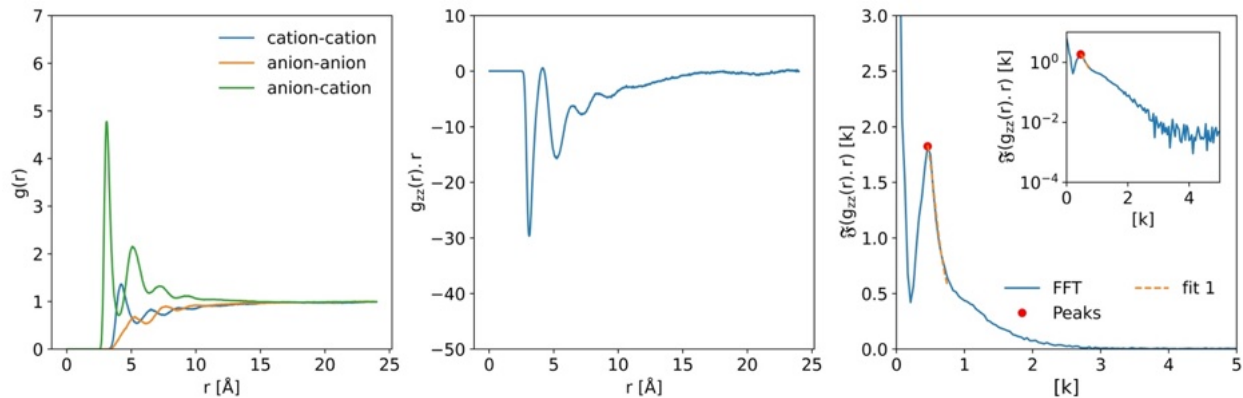


Figure S84. Derivation of λ_S using discrete Fourier Analysis for KCl 0.50 M. (a) $g_{++}(r)$, $g_{--}(r)$ and $g_{+-}(r)$ (b) $g_{zz}(r) \cdot r$ (c) $\mathfrak{F}[g_{zz}(r) \cdot r]$, peaks are fitted with the equation $\frac{1}{\sqrt{2\pi}} \frac{-\kappa_{\mathfrak{R}}}{k^2 + \kappa_{\mathfrak{I}}^2}$ to extract screening lengths ($\lambda = 1/\kappa$).

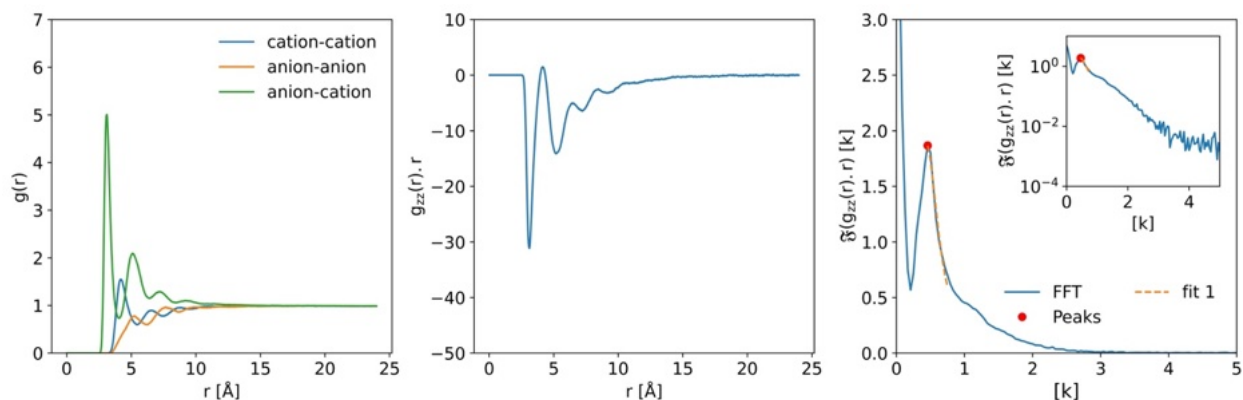


Figure S85. Derivation of λ_S using discrete Fourier Analysis for KCl 0.73 M. (a) $g_{++}(r)$, $g_{--}(r)$ and $g_{+-}(r)$ (b) $g_{zz}(r) \cdot r$ (c) $\mathfrak{F}[g_{zz}(r) \cdot r]$, peaks are fitted with the equation $\frac{1}{\sqrt{2\pi}} \frac{-\kappa_{\mathfrak{R}}}{k^2 + \kappa_{\mathfrak{I}}^2}$ to extract screening lengths ($\lambda = 1/\kappa$).

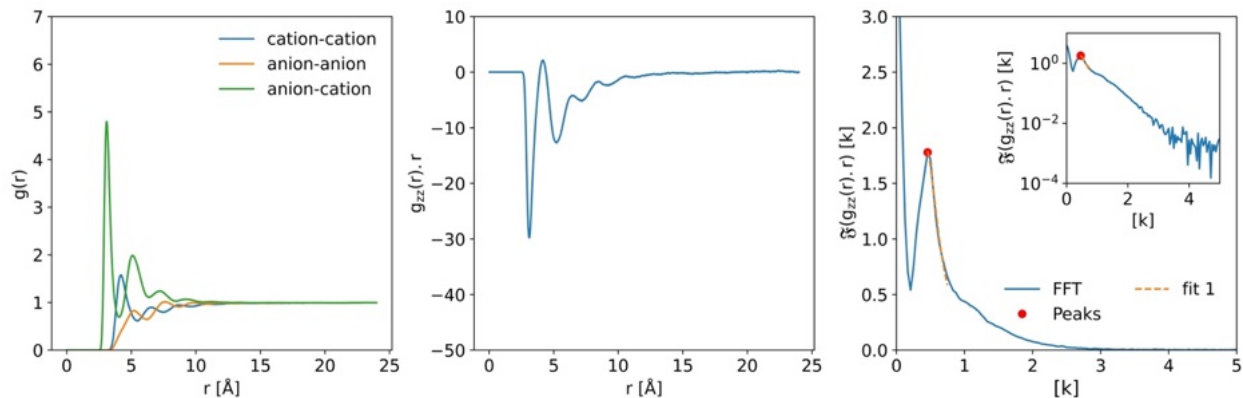


Figure S86. Derivation of λ_S using discrete Fourier Analysis for KCl 0.98 M. (a) $g_{++}(r)$, $g_{--}(r)$ and $g_{+-}(r)$ (b) $g_{zz}(r) \cdot r$ (c) $\mathfrak{F}[g_{zz}(r) \cdot r]$, peaks are fitted with the equation $\frac{1}{\sqrt{2\pi}} \frac{-\kappa_{\mathfrak{R}}}{k^2 + \kappa_{\mathfrak{I}}^2}$ to extract screening lengths ($\lambda = 1/\kappa$).

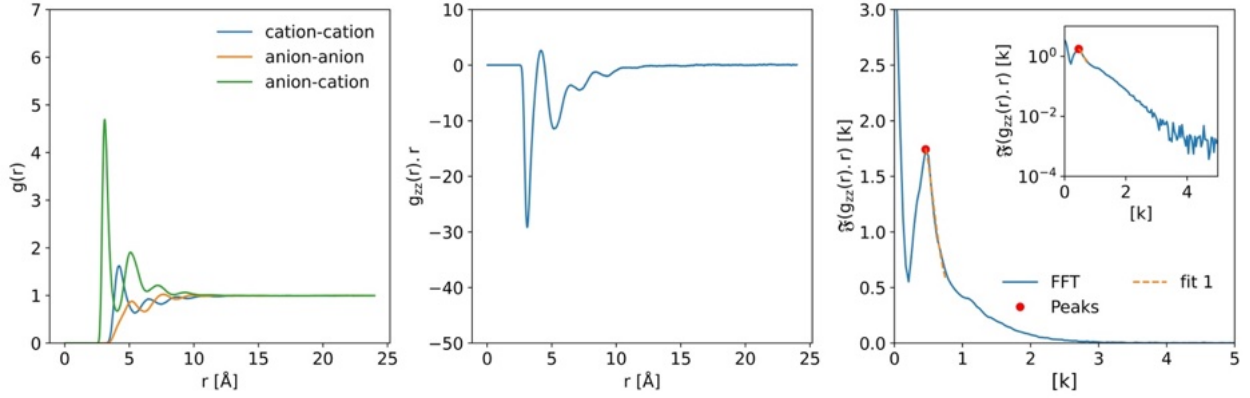


Figure S87. Derivation of λ_S using discrete Fourier Analysis for KCl 1.22 M. (a) $g_{++}(r)$, $g_{--}(r)$ and $g_{+-}(r)$ (b) $g_{zz}(r) \cdot r$ (c) $\mathfrak{F}[g_{zz}(r) \cdot r]$, peaks are fitted with the equation $\frac{1}{\sqrt{2\pi}} \frac{-\kappa_{\mathfrak{F}}}{k^2 + \kappa_{\mathfrak{F}}^2}$ to extract screening lengths ($\lambda = 1/\kappa$).

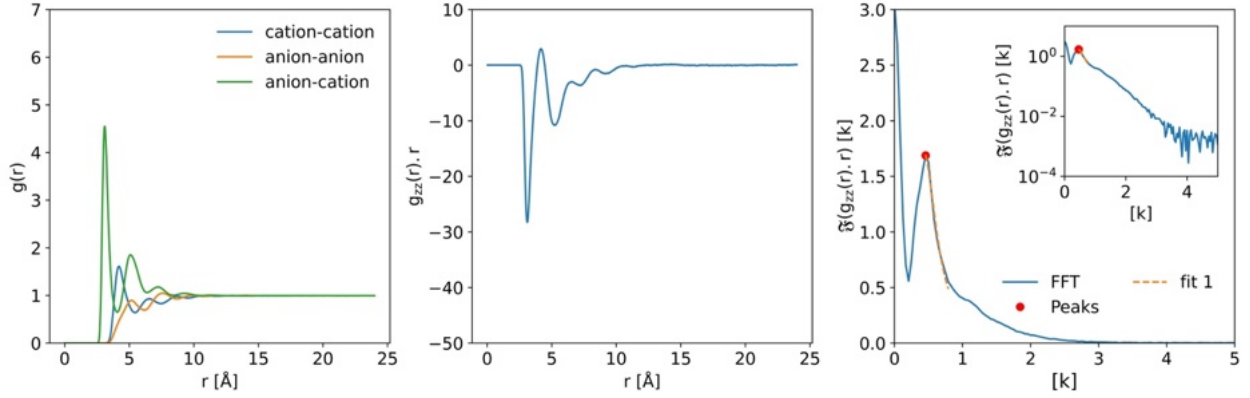


Figure S88. Derivation of λ_S using discrete Fourier Analysis for KCl 1.45 M. (a) $g_{++}(r)$, $g_{--}(r)$ and $g_{+-}(r)$ (b) $g_{zz}(r) \cdot r$ (c) $\mathfrak{F}[g_{zz}(r) \cdot r]$, peaks are fitted with the equation $\frac{1}{\sqrt{2\pi}} \frac{-\kappa_{\mathfrak{F}}}{k^2 + \kappa_{\mathfrak{F}}^2}$ to extract screening lengths ($\lambda = 1/\kappa$).

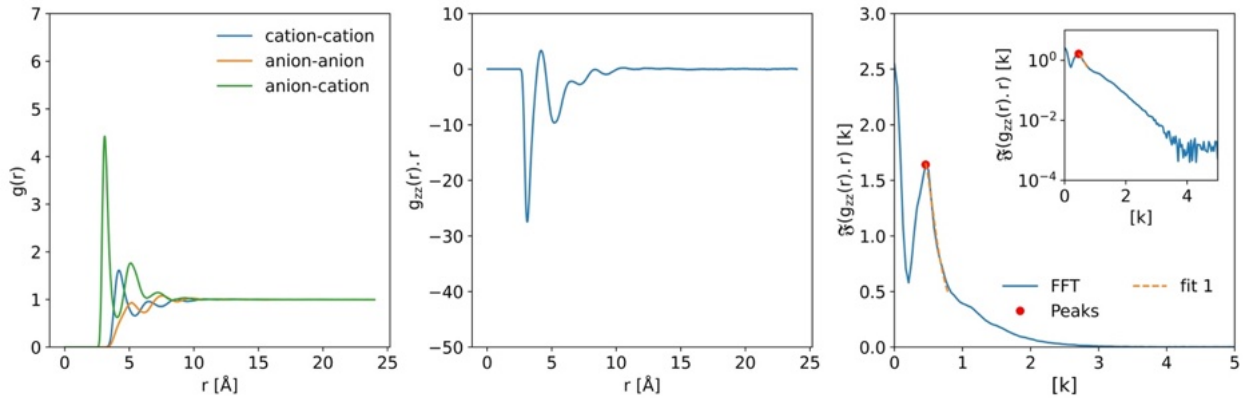


Figure S89. Derivation of λ_S using discrete Fourier Analysis for KCl 1.90 M. (a) $g_{++}(r)$, $g_{--}(r)$ and $g_{+-}(r)$ (b) $g_{zz}(r) \cdot r$ (c) $\mathfrak{F}[g_{zz}(r) \cdot r]$, peaks are fitted with the equation $\frac{1}{\sqrt{2\pi}} \frac{-\kappa_{\mathfrak{F}}}{k^2 + \kappa_{\mathfrak{F}}^2}$ to extract screening lengths ($\lambda = 1/\kappa$).

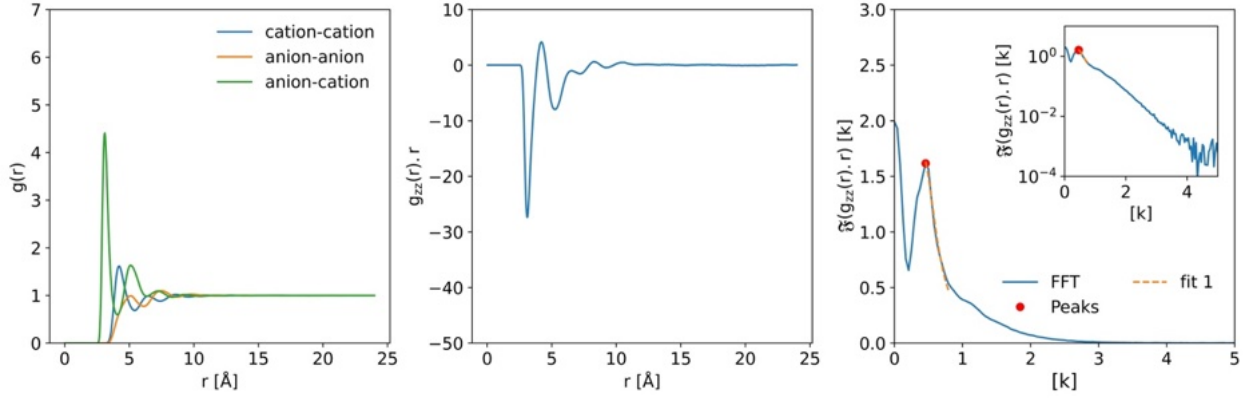


Figure S90. Derivation of λ_S using discrete Fourier Analysis for KCl 2.78 M. (a) $g_{++}(r)$, $g_{--}(r)$ and $g_{\pm}(r)$ (b) $g_{zz}(r) \cdot r$ (c) $\mathfrak{F}[g_{zz}(r) \cdot r]$, peaks are fitted with the equation $\frac{1}{\sqrt{2\pi}} \frac{e^{-\kappa_{\mathfrak{F}} r}}{k^2 + \kappa_{\mathfrak{F}}^2}$ to extract screening lengths ($\lambda = 1/\kappa$).

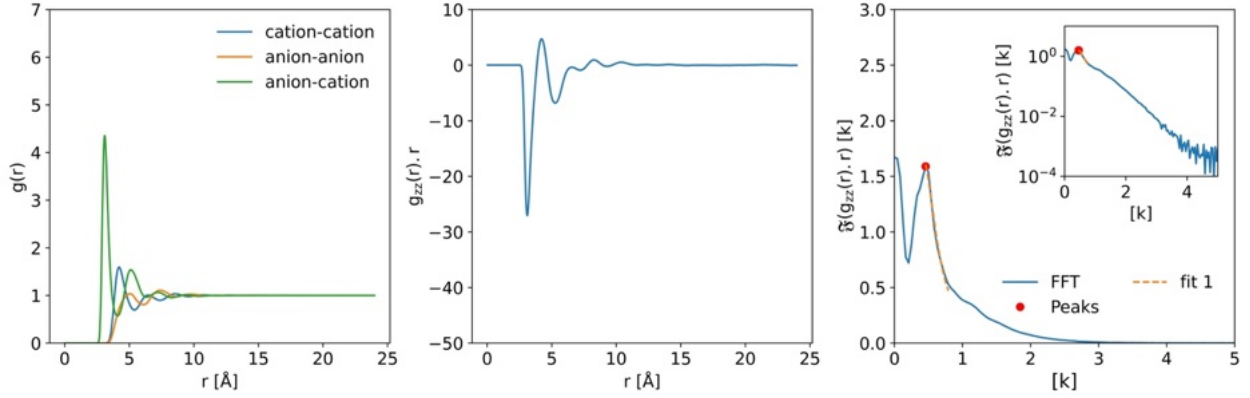


Figure S91. Derivation of λ_S using discrete Fourier Analysis for KCl 3.60 M. (a) $g_{++}(r)$, $g_{--}(r)$ and $g_{\pm}(r)$ (b) $g_{zz}(r) \cdot r$ (c) $\mathfrak{F}[g_{zz}(r) \cdot r]$, peaks are fitted with the equation $\frac{1}{\sqrt{2\pi}} \frac{e^{-\kappa_{\mathfrak{F}} r}}{k^2 + \kappa_{\mathfrak{F}}^2}$ to extract screening lengths ($\lambda = 1/\kappa$).

Cesium Chloride

Table S11. Concentration and derived λ_S values (\AA) using discrete Fourier analysis for CsCl. See accompanying Figures S92-S102.

Conc (m)	Conc (M)	Mode Frequency (\AA^{-1})			
		0.08	0.13	0.17	0.46
0.1	0.11				5.69 ± 0.26
0.5	0.50				4.77 ± 0.16
0.75	0.73				4.52 ± 0.14
1	0.96				4.36 ± 0.12
1.25	1.20				4.11 ± 0.18
1.5	1.42				4.18 ± 0.16
2	1.86				4.08 ± 0.16
3	2.68				4.07 ± 0.17
4	3.44	4.74 ± 0.06			4.11 ± 0.19
5	4.15		4.58 ± 0.14		4.20 ± 0.21
10	6.96			4.85 ± 0.00	4.76 ± 0.31

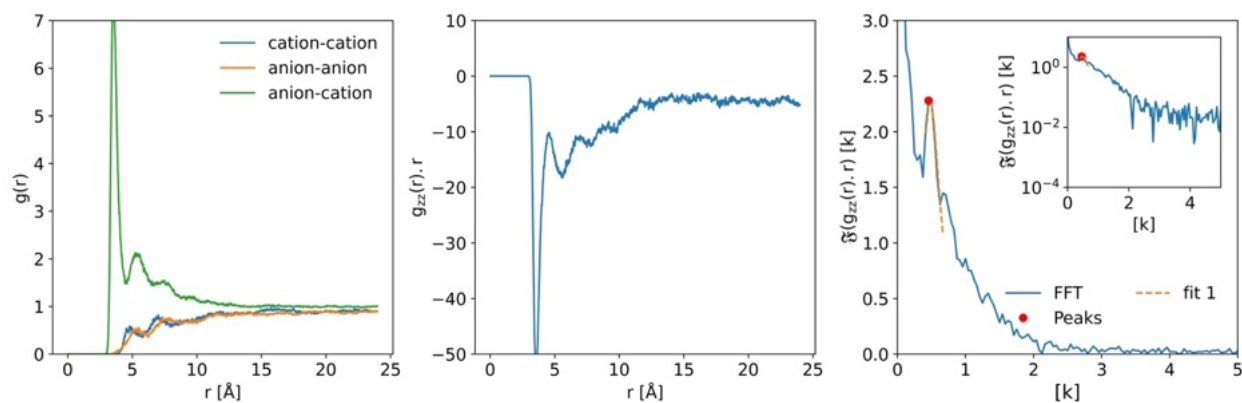


Figure S92. Derivation of λ_S using discrete Fourier Analysis for CsCl 0.11 M. (a) $g_{++}(r)$, $g_{--}(r)$ and $g_{+-}(r)$ (b) $g_{zz}(r) \cdot r$ (c) $\mathcal{F}[g_{zz}(r) \cdot r]$, peaks are fitted with the equation $\frac{1}{\sqrt{2\pi}} \frac{e^{-\kappa_{\mathcal{R}} r}}{k^2 + \kappa_{\mathcal{R}}^2}$ to extract screening lengths ($\lambda = 1/\kappa$).

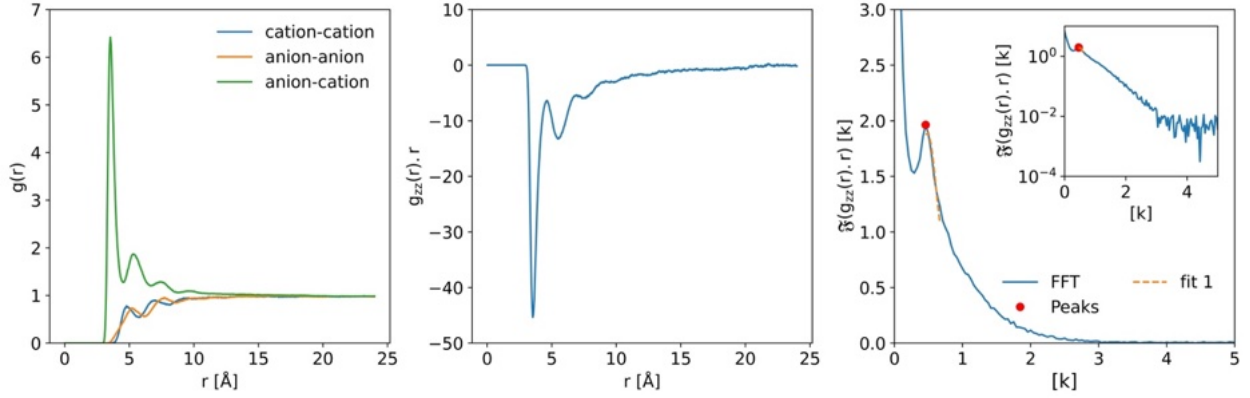


Figure S93. Derivation of λ_S using discrete Fourier Analysis for CsCl 0.50 M. (a) $g_{++}(r)$, $g_{--}(r)$ and $g_{+-}(r)$ (b) $g_{zz}(r) \cdot r$ (c) $\mathcal{F}[g_{zz}(r) \cdot r]$, peaks are fitted with the equation $\frac{1}{\sqrt{2\pi}} \frac{e^{-\kappa_{\mathcal{F}} r}}{k^2 + \kappa_{\mathcal{F}}^2}$ to extract screening lengths ($\lambda = 1/\kappa$).

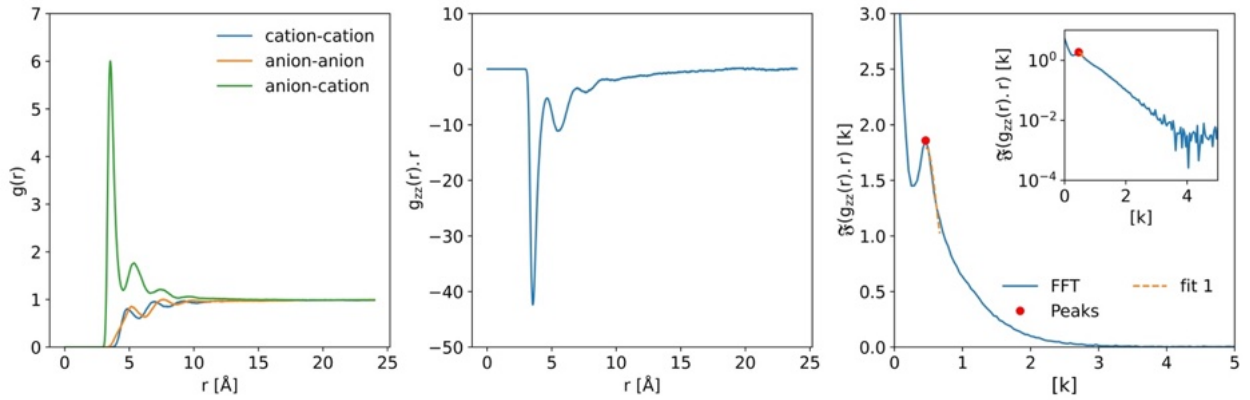


Figure S94. Derivation of λ_S using discrete Fourier Analysis for CsCl 0.73 M. (a) $g_{++}(r)$, $g_{--}(r)$ and $g_{+-}(r)$ (b) $g_{zz}(r) \cdot r$ (c) $\mathcal{F}[g_{zz}(r) \cdot r]$, peaks are fitted with the equation $\frac{1}{\sqrt{2\pi}} \frac{e^{-\kappa_{\mathcal{F}} r}}{k^2 + \kappa_{\mathcal{F}}^2}$ to extract screening lengths ($\lambda = 1/\kappa$).

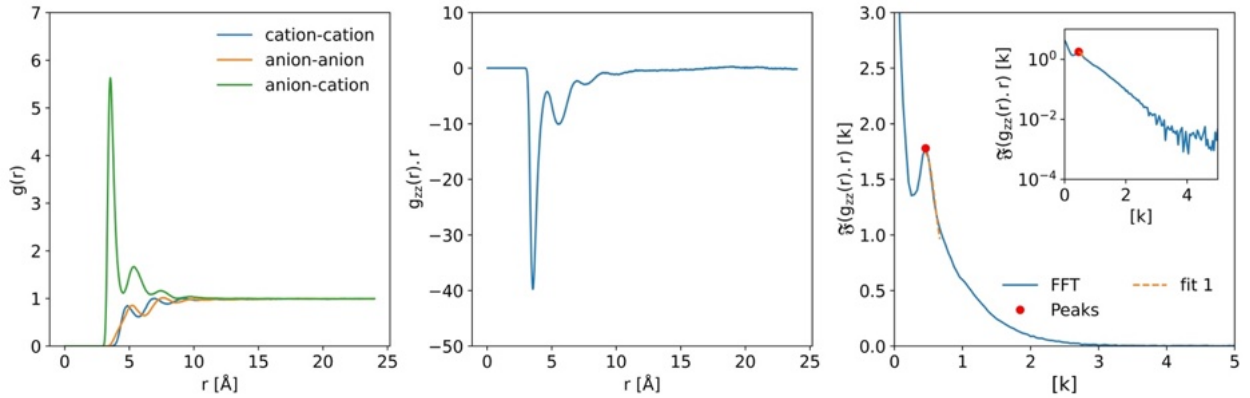


Figure S95. Derivation of λ_S using discrete Fourier Analysis for CsCl 0.96 M. (a) $g_{++}(r)$, $g_{--}(r)$ and $g_{+-}(r)$ (b) $g_{zz}(r) \cdot r$ (c) $\mathcal{F}[g_{zz}(r) \cdot r]$, peaks are fitted with the equation $\frac{1}{\sqrt{2\pi}} \frac{e^{-\kappa_{\mathcal{F}} r}}{k^2 + \kappa_{\mathcal{F}}^2}$ to extract screening lengths ($\lambda = 1/\kappa$).

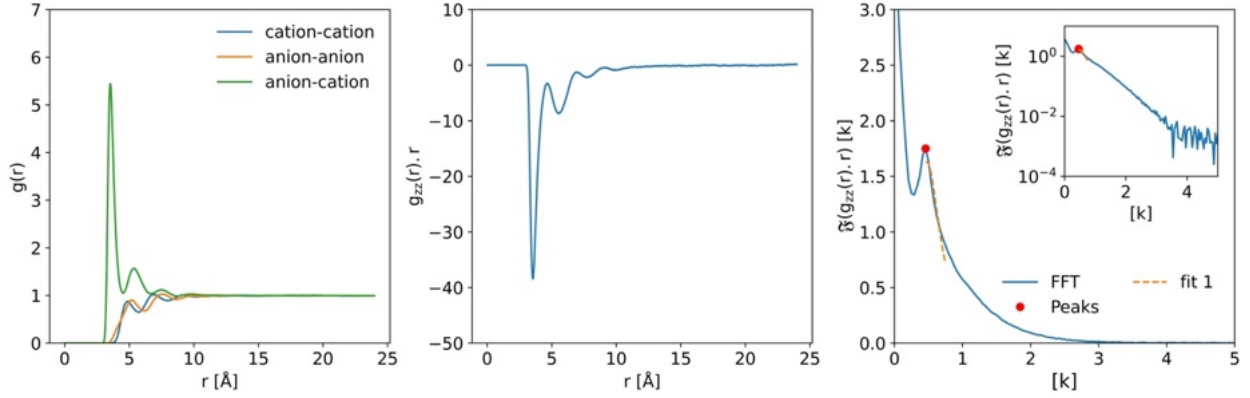


Figure S96. Derivation of λ_S using discrete Fourier Analysis for CsCl 1.20 M. (a) $g_{++}(r)$, $g_{--}(r)$ and $g_{+-}(r)$ (b) $g_{zz}(r) \cdot r$ (c) $\mathfrak{F}[g_{zz}(r) \cdot r]$, peaks are fitted with the equation $\frac{1}{\sqrt{2\pi}} \frac{-\kappa_{\mathfrak{F}}}{k^2 + \kappa_{\mathfrak{F}}^2}$ to extract screening lengths ($\lambda = 1/\kappa$).

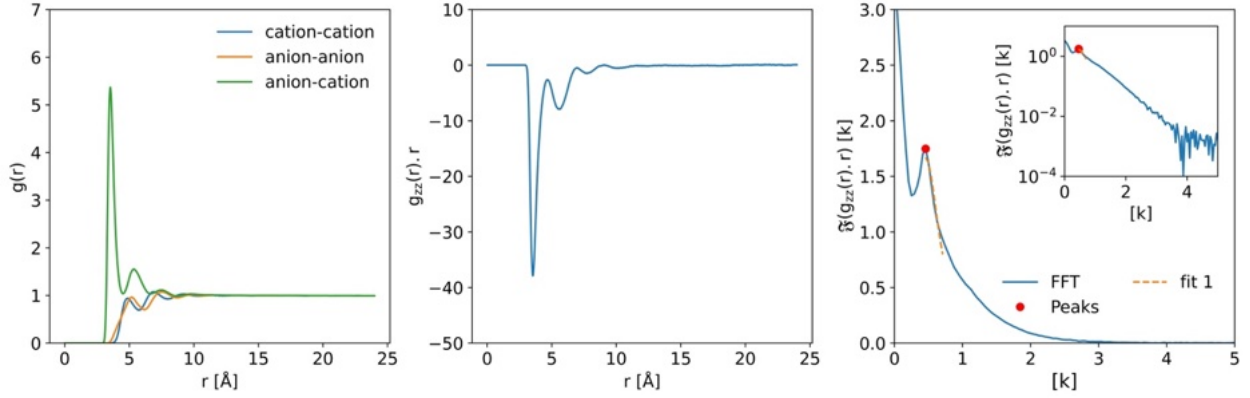


Figure S97. Derivation of λ_S using discrete Fourier Analysis for CsCl 1.42 M. (a) $g_{++}(r)$, $g_{--}(r)$ and $g_{+-}(r)$ (b) $g_{zz}(r) \cdot r$ (c) $\mathfrak{F}[g_{zz}(r) \cdot r]$, peaks are fitted with the equation $\frac{1}{\sqrt{2\pi}} \frac{-\kappa_{\mathfrak{F}}}{k^2 + \kappa_{\mathfrak{F}}^2}$ to extract screening lengths ($\lambda = 1/\kappa$).

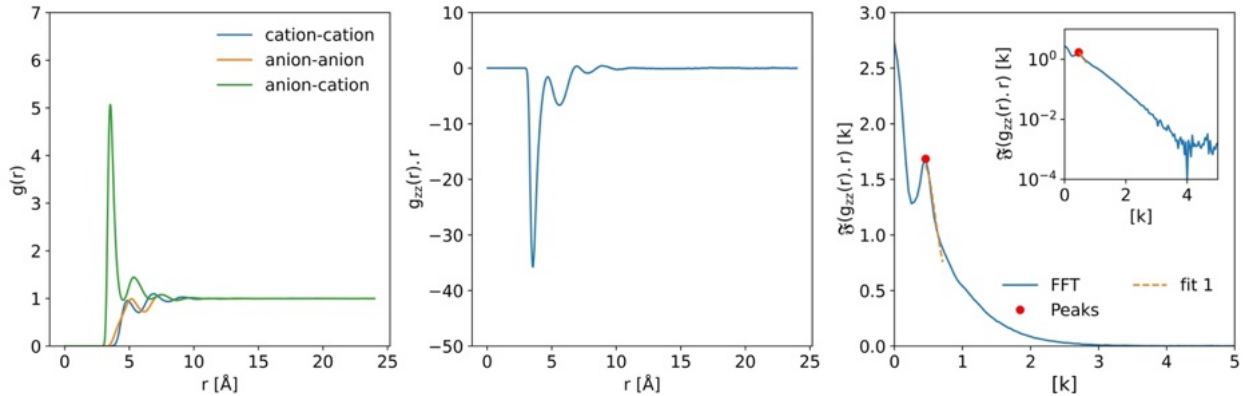


Figure S98. Derivation of λ_S using discrete Fourier Analysis for CsCl 1.86 M. (a) $g_{++}(r)$, $g_{--}(r)$ and $g_{+-}(r)$ (b) $g_{zz}(r) \cdot r$ (c) $\mathfrak{F}[g_{zz}(r) \cdot r]$, peaks are fitted with the equation $\frac{1}{\sqrt{2\pi}} \frac{-\kappa_{\mathfrak{F}}}{k^2 + \kappa_{\mathfrak{F}}^2}$ to extract screening lengths ($\lambda = 1/\kappa$).

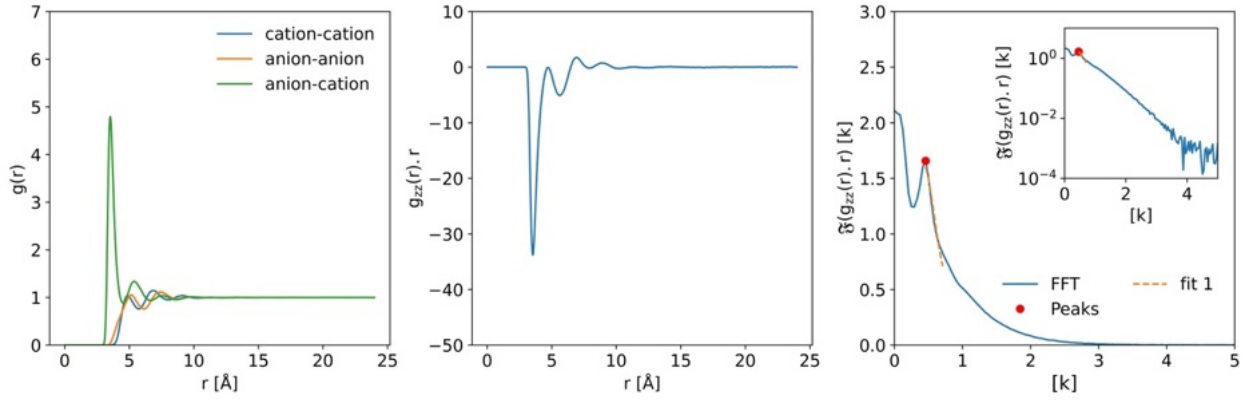


Figure S99. Derivation of λ_S using discrete Fourier Analysis for CsCl 2.68 M. (a) $g_{++}(r)$, $g_{--}(r)$ and $g_{\pm}(r)$ (b) $g_{zz}(r) \cdot r$ (c) $\mathfrak{F}[g_{zz}(r) \cdot r]$, peaks are fitted with the equation $\frac{1}{\sqrt{2\pi}} \frac{e^{-\kappa_{\mathfrak{F}} r}}{k^2 + \kappa_{\mathfrak{F}}^2}$ to extract screening lengths ($\lambda = 1/\kappa$).

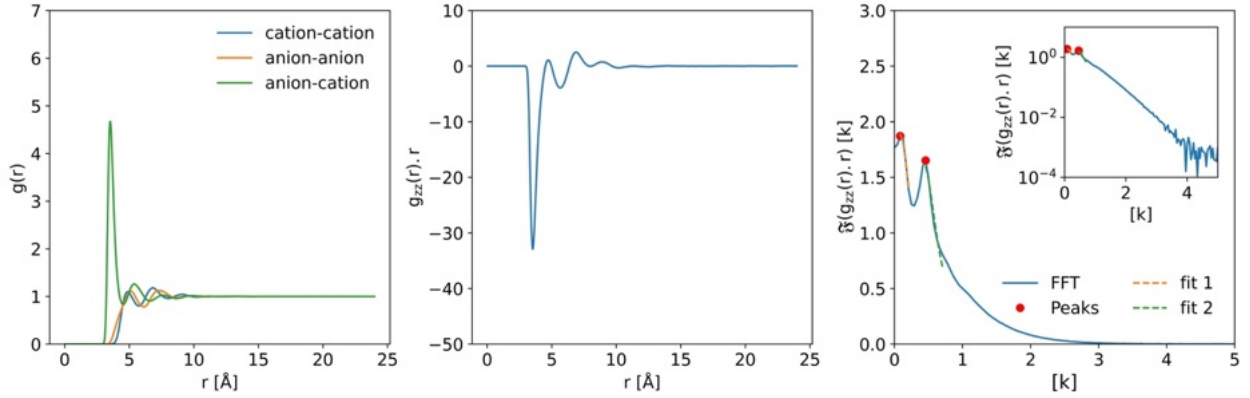


Figure S100. Derivation of λ_S using discrete Fourier Analysis for CsCl 3.44 M. (a) $g_{++}(r)$, $g_{--}(r)$ and $g_{\pm}(r)$ (b) $g_{zz}(r) \cdot r$ (c) $\mathfrak{F}[g_{zz}(r) \cdot r]$, peaks are fitted with the equation $\frac{1}{\sqrt{2\pi}} \frac{e^{-\kappa_{\mathfrak{F}} r}}{k^2 + \kappa_{\mathfrak{F}}^2}$ to extract screening lengths ($\lambda = 1/\kappa$).

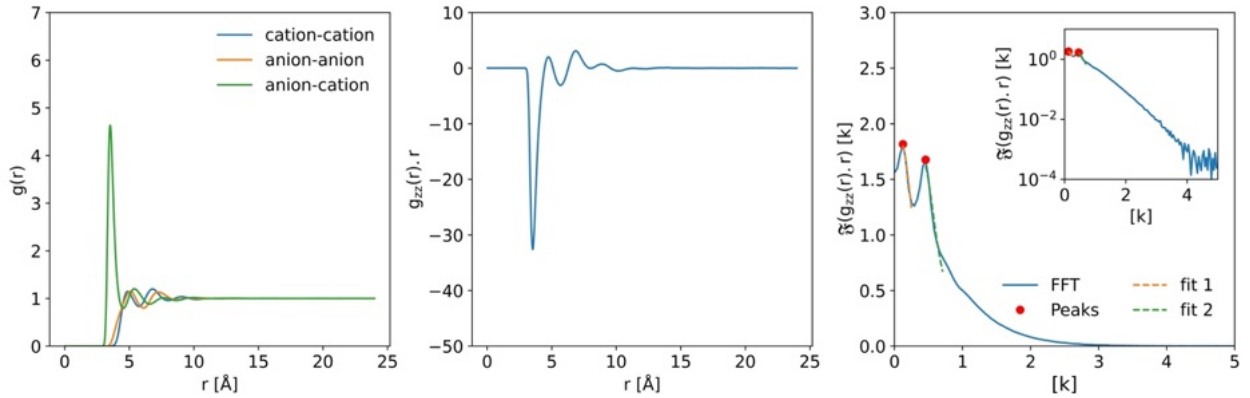


Figure S101. Derivation of λ_S using discrete Fourier Analysis for CsCl 4.16 M. (a) $g_{++}(r)$, $g_{--}(r)$ and $g_{\pm}(r)$ (b) $g_{zz}(r) \cdot r$ (c) $\mathfrak{F}[g_{zz}(r) \cdot r]$, peaks are fitted with the equation $\frac{1}{\sqrt{2\pi}} \frac{e^{-\kappa_{\mathfrak{F}} r}}{k^2 + \kappa_{\mathfrak{F}}^2}$ to extract screening lengths ($\lambda = 1/\kappa$).

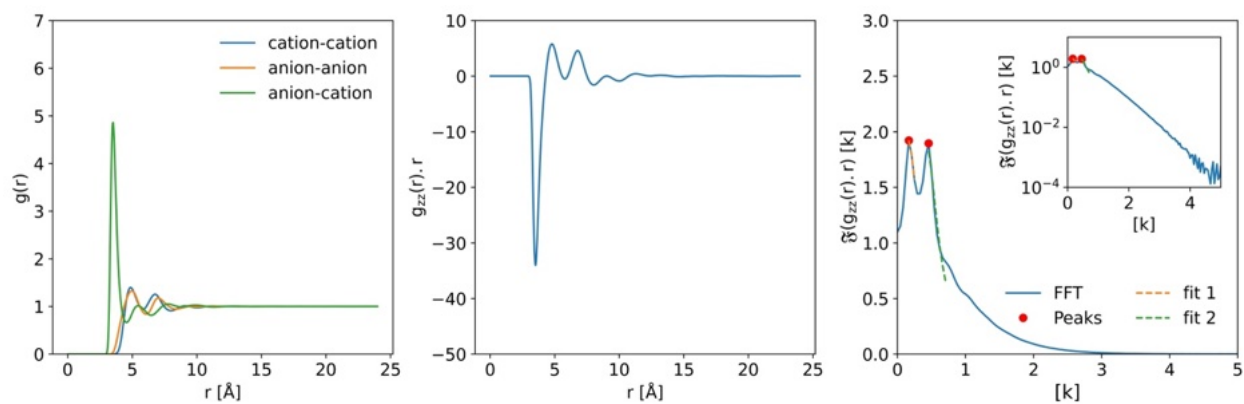


Figure S102. Derivation of λ_S using discrete Fourier Analysis for CsCl 0.96 M. (a) $g_{++}(r)$, $g_{--}(r)$ and $g_{\pm}(r)$ (b) $g_{zz}(r) \cdot r$ (c) $\mathfrak{F}[g_{zz}(r) \cdot r]$, peaks are fitted with the equation $\frac{1}{\sqrt{2\pi}} \frac{e^{-\kappa_{\mathfrak{F}} r}}{k^2 + \kappa_{\mathfrak{F}}^2}$ to extract screening lengths ($\lambda = 1/\kappa$).

Ionic Liquid: [C₂C₁im][BF₄]

Table S12. Concentration and derived λ_S values (Å) using discrete Fourier analysis for [C₂C₁im][BF₄]. See accompanying Figure S103.

Conc (M)	Mode Frequency (Å ⁻¹)			
	0.17	0.64	1.79	2.08
6.54	15.93 ± 2.33	9.19 ± 1.82	791.97 ± 561.72	710.07 ± 378.78

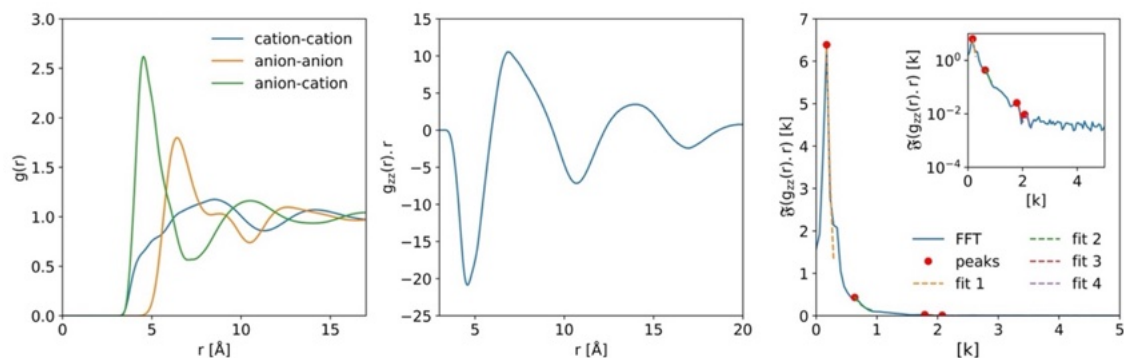


Figure S103. Derivation of λ_S using discrete Fourier Analysis for [C₂C₁im][BF₄]. (a) $g_{++}(r)$, $g_{--}(r)$ and $g_{+-}(r)$ (b) $g_{zz}(r) \cdot r$ (c) $\mathfrak{F}[g_{zz}(r) \cdot r]$, peaks are fitted with the equation $\frac{1}{\sqrt{2\pi}} \frac{-\kappa_{\mathfrak{R}}}{k^2 + \kappa_{\mathfrak{I}}^2}$ to extract screening lengths ($\lambda = 1/\kappa$).